

C.\



## LIBRARY Michigan State University

## This is to certify that the

#### dissertation entitled

## AC SIMULATION OF FIELD EFFECT TRANSISTORS WITH A HYDRODYNAMIC TRANSPORT MODEL

presented by

Yao-Tsung Tsai

has been accepted towards fulfillment of the requirements for

Ph.D. degree in Electrical Engineering.

Jimbly Sutylin Major professor

Date 5/8/90

MSU is an Affirmative Action/Equal Opportunity Institution

0-12771

PLACE IN RETURN BOX to remove this checkout from your record. TO AVOID FINES return on or before date due.

DATE DUE	DATE DUE	DATE DUE

MSU Is An Affirmative Action/Equal Opportunity Institution

# AC SIMULATION OF FIELD EFFECT TRANSISTORS WITH A HYDRODYNAMIC TRANSPORT MODEL

by

Yao-Tsung Tsai

## **A DISSERTATION**

Submitted to
Michigan State University
in partial fulfillment of the requirements
for the degree of

## **DOCTOR OF PHILOSOPHY**

Department of Electrical Engineering 1990

#### **ABSTRACT**

# AC SIMULATION OF FIELD EFFECT TRANSISTORS WITH A HYDRODYNAMIC TRANSPORT MODEL

by

### Yao-Tsung Tsai

Improvements in compound semiconductor materials and processes are producing small-geometry, high-frequency field-effect transistors (FETs) for digital, microwave and millimeter-wave applications. The design of the FETs requires accurate and efficient computer-based modeling tools which include the appropriate physical phenomenon. A computer-based simulation tool using the semiconductor hydrodynamic transport equations has been developed, evaluated and applied for studying the DC and AC behavior of III-V FETs including MESFETs and MODFETs.

The hydrodynamic transport model which solves the continuity equation, the conservation of energy equation and the Poisson equation is the basis of this simulator. The model does the DC solution by numerically solving these equations using the box-integration method for discretization and the Newton method for the discrete equation solution. The DC solution was verified by comparison to a Monte Carlo particle solution of the FET structure. The AC solution was accomplished by applying the sinusoidal small-signal analysis  $(S^3A)$  technique to the hydrodynamic transport equations. This is the first time that the hydrodynamic transport equations have been solved for the AC solution by this  $S^3A$  technique. The AC solution was compared to the AC solution found using the Monte Carlo particle simulator with a Fourier decomposition solution. FET structures of various geometries were studied with respect to their AC performance. The AC parameters simulated include y-parameters, current

gain, unilateral power gain,  $f_T$  and  $f_{\text{max}}$ . In particular, the performance of FETs in the millimeter-wave frequency range was simulated and studied.

## **ACKNOWLEDGMENTS**

I would like to thank my adviser, Professor Timothy A. Grotjohn, for his constant guidance, encouragement, valuable suggestion and inspiring discussions throughout the course of this study.

Thanks are also given to guidance committee members, Professors D. K. Reinhard, G. M. Wierzba and C. Y. Wang for taking time to serve on the examining committee.

Finally, I am also grateful to my wife Kitty for her support during this research.

## **Table of Contents**

LIST OF TABLES	viii
LIST OF FIGURES	ix
Chapter 1. INTRODUCTION	1
1.1 Semiconductor Device Modeling	1
1.2 Statement of Purpose	3
1.3 Thesis Preview	3
Chapter 2. HYDRODYNAMIC SEMICONDUCTOR EQUATIONS	7
2.1 Model History	7
2.2 Model Development	9
2.3 Relationship Between HTM and DDM	15
2.4 GaAs MESFET Simulation	19
2.5 Energy-Dependent Parameter Calculation.	23
Chapter 3. NUMERICAL SOLUTION OF THE SEMICONDUCTOR EQUATIONS	28
3.1 Finite-Difference Method	28
3.2 Finite-Element Method	30
3.3 Box-Integration Method	32
3.4 Scaling	35
3.5 Modified Scharfetter-Gummel Technique for J and S.	36
3.6 Matrix Equation Solution	42
3.6.1 Review of Matrix Equation Method.	42
3.6.2 Matrix Coefficient Allocation and Calculation.	44
3.7 Boundary Conditions	49

Chapter 4. DC SIMULATION OF MESFETS USING THE SEMICONDUCTOR HYDRODYNAMIC TRANSPORT EQUATIONS	51
4.1 Current-Voltage Characteristics Compared with Monte Carlo	51
4.2 Source and Drain Resistance Studies of Short Channel MESFET's Using Two-Dimensional Device Simulators	65
4.2.1 Source and Drain Resistance Models	66
4.2.2 Bias Dependence of Source and Drain Resistance	70
4.2.3 Source and Drain Resistance in Submicron GaAs MESFETs	74
Chapter 5. AC SIMULATION OF MESFETS USING THE SEMICONDUCTOR HYDRODYNAMIC TRANSPORT EQUATIONS	86
5.1 AC Simulation Methods	86
5.2 Sinusoidal Steady-State Analysis (S <sup>3</sup> A) using Hydrodynamic Transport Model	89
5.2.1 Model Development	89
5.2.2 Boundary Condition	94
5.2.3 Small Signal Current Calculation	94
5.2.4 Y-Parameters Calculation	96
5.3 HTM Y-Parameters Compared with Monte Carlo and Drift Diffusion Models	97
5.4 AC Performance of GaAs MESFETs	102
5.4.1 Drain Bias Dependence	105
5.4.2 Gate Bias Dependence	106
5.4.3 Gate Length Dependence	106
5.4.4 Gate-Source Spacing Dependence	106
5.4.5 Gate-Drain Spacing Dependence	106
5.4.6 Epilayer Thickness Dependence	106
5.4.7 Substrate Dependence	107
Chapter 6. HYDRODYNAMIC TRANSPORT MODEL FOR MODFET	116
6.1 Hydrodynamic Transport Equations for the MODFET	116

6.2 Simulation Results and Discussion	122
Chapter 7. CONCLUSIONS AND RECOMMENDATIONS	131
Appendix A. FINITE-ELEMENT DISCRETIZATION FOR DRIFT-DIFFUSION MODEL	133
Appendix B. DERIVATION OF THE CURRENT DENSITY AND ENERGY FLUX EXPRESSIONS USING THE MODFIED SCHARFETTER-GUMMEL TECHNIQUE	137
Appendix C. REGRID ALGORITHM	142
LIST OF REFERENCES	145

## LIST OF TABLES

Table	
3.1 Scaling factor	37
5.1 $f_{\text{max}}$ dependence on device parameters for $N_D = 2 \times 10^{17} \text{cm}^{-3}$	115

## LIST OF FIGURES

Figure	Pi	age
1.1 Di	ifferent device modeling levels	2
ve	Average drift velocity of electrons in GaAs ersus time for different fields. (b) Drift velocity	
rel	laxation time versus the electric field	4
	ne displaced Maxwellian distribution can be uniquely	
de	escribed by three quantities: $n$ , $\overline{v}$ and $T$	8
	omputer flow chart for (a) drift diffusion model,	
(b	) hydrodynamic transport model	18
2.3 G	aAs band structure	24
	esults of Monte Carlo simulation for GaAs with $T_0 = 2 \times 10^{17} cm^{-3}$ and $T_0 = 300^{\circ} K$ :	
(a	a) average electron velocity v, (b) total electron	
en	nergy $\xi$ , and (c) electron potential energy $U_p(\xi)$	
ve	ersus electric field E	26
	esults of Monte Carlo simulation for GaAs with $T_D = 2 \times 10^{17} cm^{-3}$ and $T_0 = 300^o K$ :	
(a	a) electron energy relaxation time $\tau_{\xi}(\xi)$ , (b) electron	
	nobility $\mu(\xi)$ , and (c) ratio of thermal energy to total	
en	nergy, $r(\xi)$ , versus electron total energy $\xi$	27
3.1 Fi	inite-difference mesh point notation	29
3.2 No	on-uniform finite-difference mesh	29
3.3 Fi	inite-element mesh	31
3.4 Bo	ox-integration method based on (a) point basis, (b) rectangular	
el	ement basis, and (c) triangular element basis	33
3.5 No	otation for both J and S discretization	39
3.6 Gı	rid number assignment for a rectangular mesh	45

Figu	re :	Page
4.1	Simplified two-dimensional MESFET geometry	52
4.2	The current-voltage characteristics for both HTM and Monte Carlo	54
4.3	Grid structure used in the two-dimensional Monte Carlo simulation	55
4.4	Potential distribution (V) over the entire device for $V_{GS} = 0.0 \ V$ and $V_{DS} = 1.5 \ V$	57
4.5	Electron density distribution $(m^{-3})$ over the entire device for $V_{GS}=0.0V$ and $V_{DS}=1.5V$	58
4.6	Electron energy distribution (eV) over the entire device for $V_{GS}=0.0V$ and $V_{DS}=1.5V$	59
4.7	Potential distribution at y=0.1 $\mu m$ for $V_{GS}=0.0V$ and $V_{DS}=1.5V$	61
4.8	Electron density distribution at y=0.1 $\mu m$ for $V_{GS}=0.0V$ and $V_{DS}=1.5V$	62
4.9	Electron energy distribution at y=0.1 $\mu m$ for $V_{GS}=0.0V$ and $V_{DS}=1.5V$	63
4.10	Current voltage characteristics for both HTM and DDM	64
4.11	MESFET structure showing the lateral gate depletion regions $\Delta L_{GS}$ and $\Delta L_{GD}$	68
4.12	Source (solid-line) and drain (dashed line) resistance versus gate voltage for a silicon MESFET using the power dissipation definition	72
4.13	Source resistance versus drain voltage with a gate voltage of 0.3 volts	73
4.14	Change in the lateral depletion width $\Delta L_{GD}$ versus drain voltage	75
4.15	Drain resistance between cross section A (shown in Figure 4.11) and the drain contact versus drain voltage	76

Figu	re I	Page
4.16	Drain resistance versus drain voltage for a silicon MESFET	77
4.17	Power dissipation (dashed line) and electron heating (solid line) in the drain resistance region $R_{D1}$ versus drain voltage for a $L_G=0.4~\mu m$ GaAs MESFET	81
4.18	Electron temperature versus position between the source and the drain as calculated using the energy transport simulator	82
4.19	Equivalent drain resistance versus drain voltage for a $L_G = 0.4 \ \mu m$ GaAs MESFET	83
4.20	Total electron energy above the Γ valley minimum (solid line) and the electron kinetic energy (dashed line) versus position between the source and drain at a depth	
	of 0.08 μm	85
5.1	Fourier decomposition method	87
5.2	Charge partitioning method for (a) a two terminal device, and (b) a three terminal device	90
5.3	Notation for small-signal current density calculation	95
5.4	The three-terminal y-parameter equivalent circuit	95
5.5	A comparison of y-parameters versus frequency for both the HTM method and the Monte Carlo method	98
5.6	A comparison of y-parameters versus frequency for both the HTM method and the DDM method	99
5.7	The three gains $A_I$ , $A_V$ and $G_U$ versus frequency from the HTM	100
5.8	The three gains $A_I$ , $A_V$ and $G_U$ versus frequency from the DDM	101
5.9	(a) Circuit model of a MESFET. (b) The extrapolation of the low-frequency gain overestimates the unity power gain frequency, $f_{max}$	104

Figu	re I	Page
5.10	(a) $G_U$ versus frequency for various $V_{DS}$ .	
	(b) $f_{\text{max}}$ versus $V_{DS}$	108
5.11	(a) $G_U$ versus frequency for various $V_{GS}$ .	
	(b) $f_{\text{max}}$ versus $V_{GS}$	109
5.12	(a) $G_U$ versus frequency for various $L_G$ .	
	(b) $f_{\max}$ versus $L_G$	110
5.13	(a) $G_U$ versus frequency for various $L_{GS}$ .	
	(b) $f_{\text{max}}$ versus $L_{GS}$	111
5.14	(a) $G_U$ versus frequency for various $L_{GD}$ .	
	(b) $f_{\rm max}^{\prime}$ versus $L_{GD}$	112
5.15	(a) $G_{II}$ versus frequency for various epilayer thickness $a$ .	
	(b) $f_{\text{max}}$ versus $a$	113
5 16	(a) $G_U$ versus frequency with or without substrate.	
J.10	(b) $N_D$ versus depth	114
	Basic device topology of the MODFET	
6.2	Energy band diagram for a MODFET	117
6.3	Equilibrium ohmic contact boundary condition model	121
6.4	The current-voltage characteristics of the MODFET for	
	$V_{GS}$ = 0.0V and $V_{GS}$ =0.2V	123
6.5	The conduction band distribution (eV) over the entire	
	device for $V_{GS} = 0.0 V$ and $V_{DS} = 1.0 V$	124
66	Electron density distribution ( $m^{-3}$ ) over the entire	
0.0	device for $V_{GS} = 0.0 V$ and $V_{DS} = 1.0 V$	125
		120
6.7	Electron energy distribution (eV) over the GaAs layer for	107
	$V_{GS} = 0.0 V$ and $V_{DS} = 1.0 V$	12/
6.8	Longitudinal electron current density distribution $(A/m^2)$	
	over the entire device for $V_{GS} = 0.0 V$ and $V_{DS} = 1.0 V$	128
6.9	The y-parameters versus frequency for the MODFET	
	using HTM	129

Figure	Page
$6.10~G_U~{ m and}~A_I~{ m versus}$ frequency for the MODFET using HTM	130
Appendix	
Figure	Page
C.1 Regrid algorithm for rectangular mesh	143

#### CHAPTER 1

#### INTRODUCTION

## 1.1 Semiconductor Device Modeling

Modeling for semiconductor devices means to produce a representation or simulation of a device, or to make a description or analogy which helps to visualize the device characteristics that can not be directly observed. Modeling is often done by solving the appropriate mathematical equations that describe the device operation. The semiconductor equations consist of a set of partial differential equations which must be solved subject to a pre-defined set of boundary condition over a specified domain. There are two approaches to describe the device behavior: (1) closed-form analytical solution, and (2) numerical solution. In many circumstances, it is possible to simplify the device model to be a closed-form analytical expression. The solution can be directly computed using this analytical expression with minimal computer time, hence, the analytical solution is suited for circuit-level simulation. However, they are severely limited in their range of application and accuracy because of the multidimensional and non-ideal nature of most modern devices. The numerical approach requires considerably more computer time than the analytical method, but usually produces more accurate results and provides greater flexibility. Figure 1.1 shows the different device modeling levels.

In order to obtain higher speed and higher integration performance, the size of semiconductor devices has been drastically reduced to submicrometer dimensions due to progress in fabrication technology. Numerical simulation techniques are required for submicrometer channel length devices in order to design and improve the devices for various applications. The numerical models used to model semiconductor devices may be classified into two types depending on the solution techniques. The two

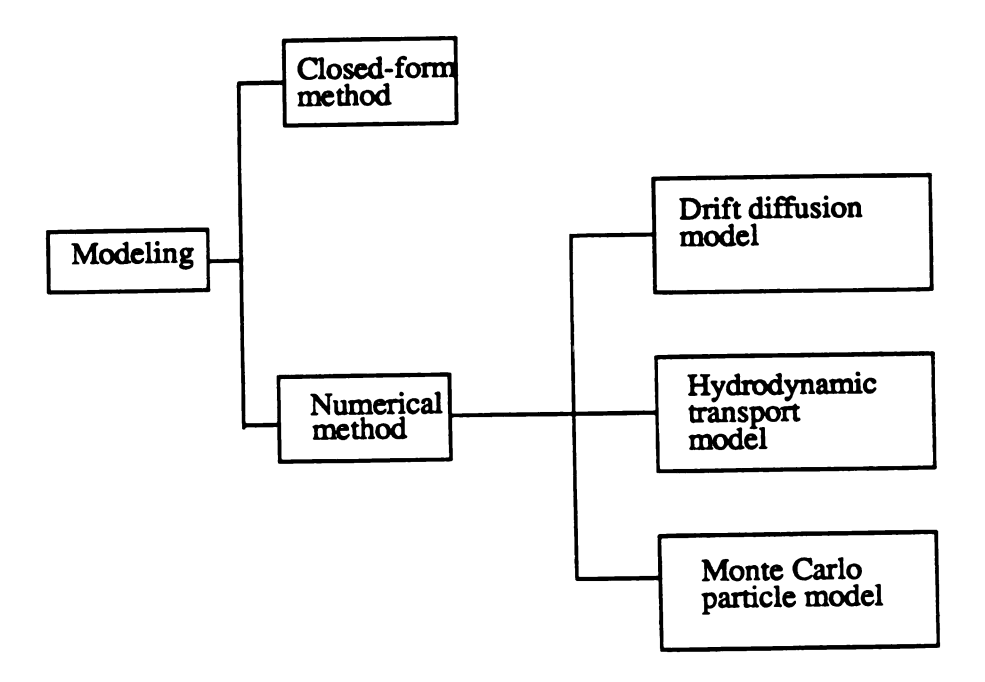
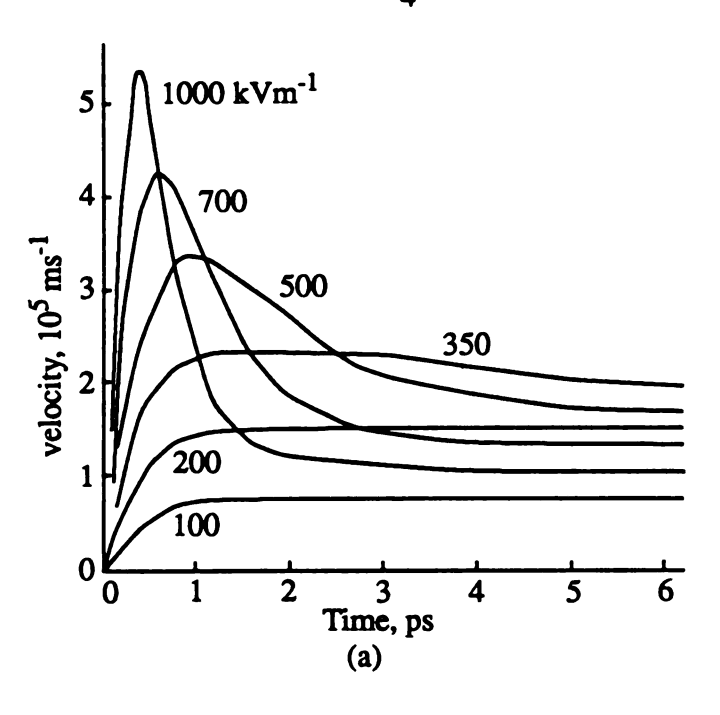


Figure 1.1. Different device modeling levels.

technique are a continuum approach treating the macroscopic quantities of carrier transport directly and the particle approach treating the macroscopic quantities as averages of many microscopic events. The continuum approach has a variety of methods including the drift diffusion model which has received the most use in the past. The drift-diffusion model (DDM) or classical model is based on solving the continuity equation and Poisson equation. This makes two central assumptions: (1) there is a steady-state thermal equilibrium between mobile carriers and the crystal lattice, and (2) there is a stationary relationship between the electric field and the carrier velocity (local field dependent mobility). In FET's with submicrometer channels, the electrons are not transported under the carrier-lattice equilibrium conditions, and nonstationary effects such as velocity overshoot become significant. The non-stationary effects can be understood with the aid of Figure 1.2 [1]. When a constant electric field is applied in a homogeneous uniformly-doped material, it takes some time for electrons to reach steady state. Figure 1.2(a) shows that velocity overshoot occurs before steady state has been reached. The velocity overshoot can improve the device performance for submicrometer devices. DDM makes the stationary assumption which is equivalent to using the velocity values at the times greater than 5ps in Figure 1.2(a), and neglects the velocity overshoot effect. Figure 1.2(b) calculates the delay time for electrons to reach within 95% of their steady state value. Therefore, the drift-diffusion model does not accurately predict importment phenomena related to nonstationary effects which occur in today's small-geometry semiconductor devices.

For accurate modeling of nonstationary effects, two major approaches have been developed. The first is the Monte Carlo particle simulation [1-4] which gives accurate solutions based on detailed transport and band structure parameters but at a large expense in computation time. This large computation time is unattractive for device optimization and the extraction of circuit simulation model parameters. The second is the hydrodynamic transport simulation [5-11] which solves the conservation equations



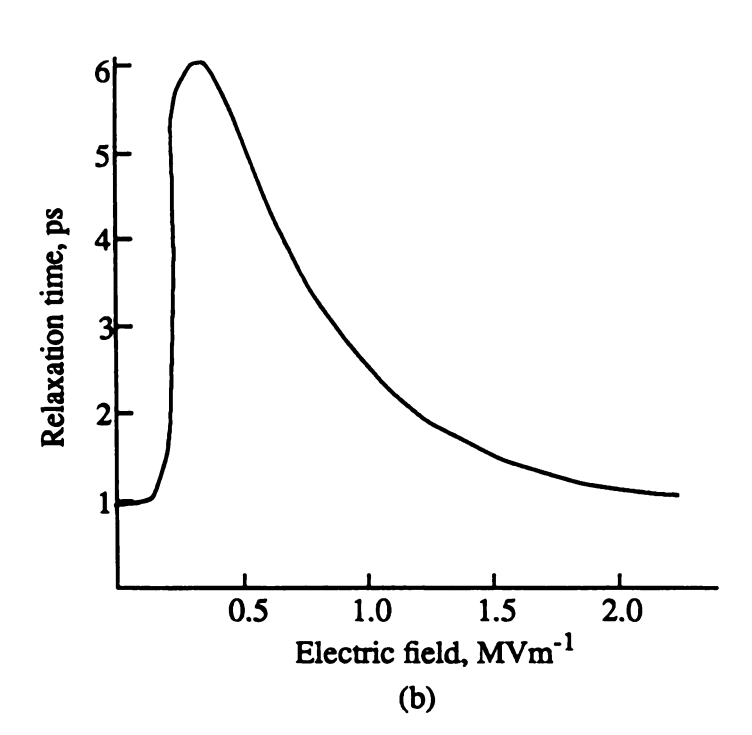


Figure 1.2. (a) Average drift velocity of electrons in GaAs versus time for different fields. (b) Drift velocity relaxation time versus the electric field. This relaxation has been defined in the text.[1]

for particles, momentum, and energy. This method greatly reduces the amount of CPU time compared with the Monte Carlo simulation method.

### 1.2 Statement of Purpose

Due to nonstationary effects, the DC, AC, and transient performance of field effect transistors must be carefully evaluated. The primary goal of this study is to develop a two-dimensional device simulator using the hydrodynamic transport model (HTM) for III-V FETs. The simulator should include the following features:

- a) solution of the three conservation equations (particle conservation, momentum conservation, and energy conservation) coupled with Poisson's equation,
- b) DC and AC simulation capabilities,
- c) transport parameters calculated from Monte Carlo simulations,
- d) regrid capabilities based on potential, electron concentration and electron energy, and
- e) heterojunction capabilities for the simulation of heterostructure FETs.

The simulator will be used to model the high-frequency (1-100's GHz) behavior of III-V FETs (MESFETs and MODFETs), and to compared to the results obtained from the Monte Carlo method or to the results available in the literature. The results of this study will not only provide information on device performance, but will also contribute to the basic understanding of device modeling using hydrodynamic transport model.

## 1.3 Thesis Preview

The thesis is divided into seven chapters. Chapter 2 develops the hydrodynamic transport model (HTM), reviews previous works and presents the model for this research. Chapter 3 describes the numerical technique for this model. In particular, the discretizations for current density and energy flux are described in detail. The DC

simulation solution of the MESFET is discussed and verified using a Monte Carlo particle simulation in Chapter 4. The sinusoidal small-signal analysis  $(S^3A)$  technique applied to the HTM is described and verified in Chapter 5. The AC performance dependence on device parameters is also studied. The HTM model is extented to the DC and AC simulations of the MODFET in Chapter 6. Conclusions are given in the last chapter.

#### **CHAPTER 2**

## HYDRODYNAMIC SEMICONDUCTOR EQUATIONS

This chapter starts with a review of the literature on the hydrodynamic transport model followed by the development of the model. The relationship between the hydrodynamic transport model (HTM) and the drift-diffusion model (DDM) will be discussed. Also, the HTM used in previous work and in this study will be included in this chapter.

## 2.1 Model History.

One of the earliest solutions of the Boltzmann transport equation (BTE) for the hot-electron problem, which was to influence subsequent developments in the field, was given by Stratton[12]. Stratton expanded the nonequilibrium distribution function in spherical harmonics, assuming the first two terms to be important. Applications to device simulation using Stratton-based transport model may be found to date in Ou and Tang [13], Cook[14], and Widiger et al. [15].

A further development that was more general in approach was given by Blotekjaer[16]. Blotekjaer solved the transport equations for electrons in a two-valley semiconductor. Instead of expanding the distribution function into harmonics as Stratton, Blotekjaer derived the model by taking the first three moments of the BTE to give the macroscopic quantities electron concentration  $n_i$ , drift velocity  $\overline{v_i}$ , and electron temperature  $T_i$ , where i indicates the valley (see Figure 2.1). The basic assumption of this theory is that the distribution of electrons within each valley can be described adequately by three quantities, namely, electron density  $n_L$ , drift velocity  $\overline{v_L}$ , and temperature  $T_L$  in the lower valley, and  $n_U$ ,  $\overline{v_U}$ , and  $T_U$  in the upper valley. It follows that all quantities which depend on the distribution function are uniquely determined by the parameters  $n_L$ ,  $\overline{v_L}$ ,  $T_L$ ,  $n_U$ ,  $\overline{v_U}$ , and  $T_U$ . This assumption is satisfied by displaced

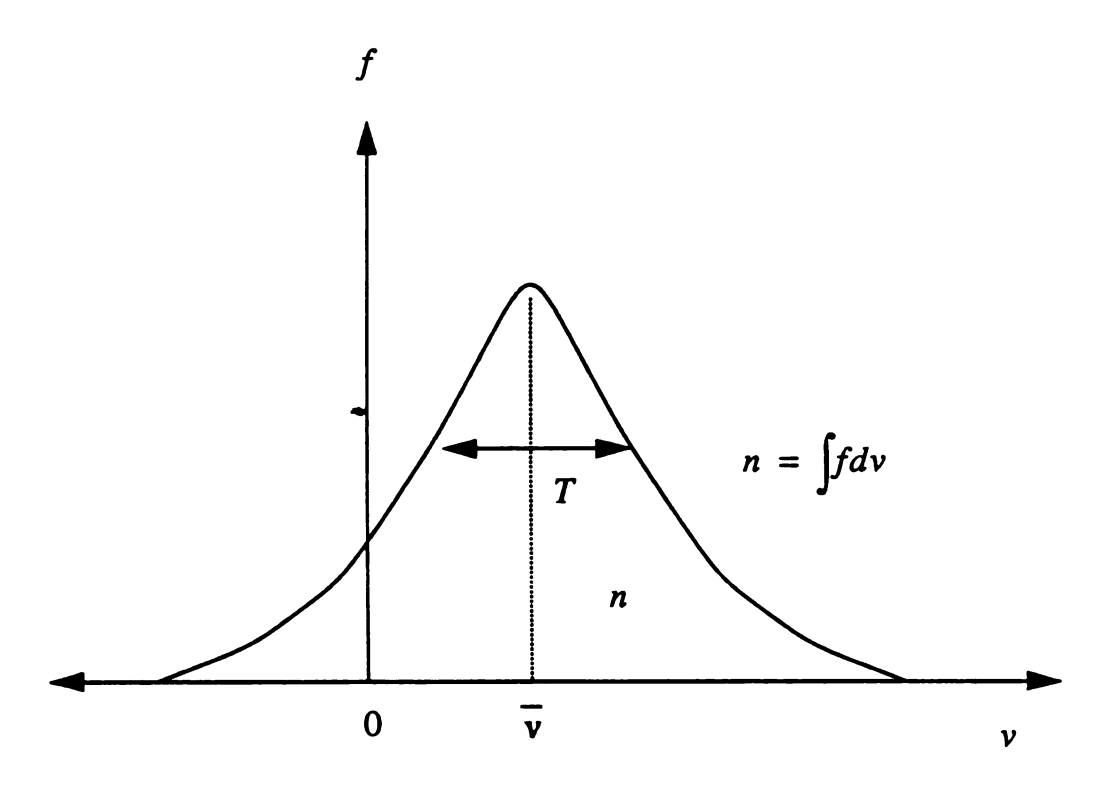


Figure 2.1. The displaced Maxwellian distribution can be uniquely described by three quantities: n,  $\bar{v}$  and T. n is electron density and describes the area under the distribution curve.  $\bar{v}$  is the mean velocity and describes how far the distribution function is displaced from its equilibrium value  $\bar{v}_0 = 0$ , and T is electron temperature and describes how wide the particle velocity spreads away from its mean velocity  $\bar{v}_0$ .

Maxwellian distributions which can be expressed as[17]

$$f_i(v_i) = n_i \left[ \frac{m^*}{2\pi k_B T} \right]^{3/2} \exp\left[ -\frac{m^* (v_i - \overline{v_i})^2}{2k_B T} \right].$$
 (2.1)

Equation (2.1) is described by three quantities:  $n_i$ ,  $\overline{v_i}$ , and  $T_i$ . However, the analysis is not restricted to any particular distribution function. Applications to device simulation using the Blotekjaer-based transport model may be found to date in Cook and Frey [6], and Snowden and Loret [7].

## 2.2 Model Development

This section will develop the first three moment equations based on the Boltzmann transport equation (BTE) for a single, parabolic energy band.

Charged particles in semiconductors can be characterized in terms of their position in space  $\mathbf{r}$  and velocity  $\mathbf{v}$  at time  $\mathbf{t}$ . The density of particles  $n(\mathbf{r},t)$  may be described by means of a distribution function  $f(\mathbf{r},\mathbf{v},t)$ , which is itself a function of phase and velocity space as well as time. The density of particles is given as

$$n(\mathbf{r},t) = \int f(\mathbf{r},\mathbf{v},t)d\mathbf{v}. \qquad (2.2)$$

The BTE can be written as [17]

$$\frac{\partial f}{\partial t} + \mathbf{v} \cdot \frac{\partial f}{\partial \mathbf{r}} + \frac{F}{m^*} \cdot \frac{\partial f}{\partial \mathbf{v}} = (\frac{\partial f}{\partial t})_c \tag{2.3}$$

where f is a distribution function  $f(\mathbf{r}, \mathbf{v}, t)$ , F represents external forces,  $m^*$  is particle effective mass. The right hand side includes the randomly-timed scattering events that the particles experience. Since (2.3) does not have a closed form solution for the devices being considered, one approach to solving the BTE consists of simulating the motion of one or more carriers at a microscopic level with Monte Carlo methods [1-4]. However, this category of simulations is computationally intensive, and therefore, with a few exceptions only, not suitable for engineering application.

An alternative approach is to solve the moment equations, which are obtained from (2.3) through multiplying by various functions of velocity,  $\Phi(\mathbf{v})$ , and integrating over velocity space. Essentially,  $\Phi(\mathbf{v})$  takes the values 1,  $\mathbf{v}(\text{ or } v_i)$ ,  $\mathbf{v}(\text{ or } v_i v_j)$ , ..., thus giving rise to the zero-order, first-order, second-order, ..., moment equations, respectively. The procedure is straightforward, though tedious for higher orders. It replaces an equation for the distribution function,  $f(\mathbf{r}, \mathbf{v}, t)$ , by equations which are function of  $\mathbf{r}$  and t only.

The average over velocity space of an arbitrary function  $\phi(\mathbf{r}, \mathbf{v}, t)$  is defined by

$$\langle \phi \rangle = \frac{1}{n(\mathbf{r},t)} \int \phi(\mathbf{r},\mathbf{v},t) f(\mathbf{r},\mathbf{v},t) d\mathbf{v}$$
 (2.4)

where  $n(\mathbf{r},t)$  is defined in (2.2). Hence, multiplying (2.3) by  $\Phi(\mathbf{v})$  and integrating over velocity space, the general moment equation may be written

$$\frac{\partial (n < \Phi >)}{\partial t} + \frac{\partial}{\partial \mathbf{r}} \cdot (n < \mathbf{v} \Phi >) - \frac{ne}{m^*} \mathbf{E} \cdot \langle \frac{\partial \Phi}{\partial \mathbf{v}} \rangle$$

$$= \left[ \frac{\partial}{\partial t} (n < \Phi >) \right]_c \tag{2.5}$$

where F is replaced by e E. e is the particle charge and E is the electric field.

Thus the BTE for the distribution function f is replaced by a set of equations containing averaged quantities. Each moment equation introduces the next higher-order velocity moment due to the second term in (2.5). The moment equations are then an infinite set of equations unless some additional assumptions are used to break the chain of equations and restrict the variables to a manageable number. These additional assumptions will be considered below.

The zero-order moment equation is obtained from (2.5) by putting  $\Phi = 1$ 

$$\frac{\partial n}{\partial t} + \nabla \cdot (n \, \overline{\mathbf{v}}) = \left[ \frac{\partial n}{\partial t} \right]_{c} \tag{2.6}$$

where

$$\overline{\mathbf{v}} = \langle \mathbf{v} \rangle = \frac{1}{n} \int \mathbf{v} f d\mathbf{v} . \tag{2.7}$$

The zero-order moment equation (2.6) is the carrier continuity equation. According to (2.6) the increase of particle density plus the divergence of particles equals the increase in density due to collisions.

The first-order moment equation, putting  $\Phi = m^* v_i$ , gives for the *i*th component of the equation

$$\frac{\partial (m^* n \overline{v_i})}{\partial t} + \nabla \cdot (m^* n \langle v v_i \rangle) - n e E_i = \left[ \frac{\partial}{\partial t} (m^* n \overline{v_i}) \right]_c . \tag{2.8}$$

The general second-order moment equation uses  $\Phi = (m^*/2)v_iv_j$ . For the development of the energy conservation equation it is adequate to take the cases i = j and sum over i = 1,2,3. Then,  $\Phi = \frac{1}{2}m^*v^2$ , and this gives

$$\frac{\partial}{\partial t}(n < \frac{1}{2}m^*v^2 >) + \nabla \cdot (n < \frac{1}{2}m^*v^2 v >) - ne \, \mathbf{E} \cdot \overline{\mathbf{v}}$$

$$= \left[ \frac{\partial}{\partial t}(n < \frac{1}{2}m^*v^2 >) \right]_c \tag{2.9}$$

where  $\langle v_i v_j \rangle$  and  $\langle v^2 v_i \rangle$  may be written

$$\langle v_i v_j \rangle = \langle (v_i - \overline{v_i} + \overline{v_i})(v_j - \overline{v_j} + \overline{v_j}) \rangle = \frac{p_{ij}}{m^* n} + \overline{v_i} \overline{v_j}$$
 (2.10)

$$\langle v^2 v_j \rangle = \sum_{i=1}^{3} \langle v_i v_i v_j \rangle = \sum_{i=1}^{3} \left[ \frac{q_{iij}}{m^* n} + \frac{p_{ii}}{m^* n} \overline{v_j} + \frac{2p_{ij}}{m^* n} \overline{v_i} + \overline{v_i} \overline{v_i} \overline{v_j} \right]$$
(2.11)

with  $p_{ij}$ , the pressure tensors, being given by

$$p_{ij} = m^* n < (v_i - \overline{v_i})(v_j - \overline{v_j}) > = m^* \int (v_i - \overline{v_i})(v_j - \overline{v_j}) f dv = p_{ji}$$
 (2.12)

and  $q_{ijk}$ , the heat tensors, being given by

$$q_{ijk} = m^{\bullet} n \langle (v_i - \overline{v_i})(v_j - \overline{v_j})(v_k - \overline{v_k}) \rangle. \tag{2.13}$$

Substituting (2.10) and (2.11) into the first-order moment equation (2.8) and into the second-order moment equation (2.9) gives

$$\frac{\partial}{\partial t}(m^* n \overline{v_i}) + \sum_{j=1}^{3} \frac{\partial}{\partial r_j}(p_{ij} + m^* n \overline{v_i} \overline{v_j}) - neE_i = \left[\frac{\partial}{\partial t}(m^* n \overline{v_i})\right]_c$$
(2.14)

and

$$\frac{\partial}{\partial t} \left[ \frac{1}{2} p_{ii} + \frac{1}{2} m^* n \overline{v_i}^2 \right] + \sum_{j=1}^3 \frac{\partial}{\partial r_j} \left[ \frac{1}{2} q_{iij} + \frac{1}{2} p_{ii} \overline{v_j} + p_{ij} \overline{v_i} + m^* n \left( \frac{1}{2} \overline{v_i}^2 \overline{v_j} \right) \right] - ne E_i \overline{v_i} = \left[ \frac{\partial}{\partial t} \left( n < \frac{1}{2} m^* v_i^2 > \right) \right]_c \tag{2.15}$$

for the momentum and energy conservation equation, respectively.

From elementary gas kinetic theory, we define

$$nk_B T_{ij} = m^* \int (v_i - \overline{v_i})(v_j - \overline{v_i}) f dv$$
 (2.16)

where  $k_B$  is Boltzmann's constant and  $T_{ij}$  is related to the pressure tensor as

$$p_{ij} = nk_B T_{ij} . (2.17)$$

Finally, the components of the heat flux vector are defined as

$$Q_i = \frac{1}{2} m^* \int (v - \overline{v})^2 (v_i - \overline{v_i}) f dv = \sum_{j=1}^3 \frac{1}{2} q_{ijj}$$
 (2.18)

by (2.13).

Using (2.17), (2.14) reduces to

$$\frac{\partial m^* n \overline{v_i}}{\partial t} + \sum_{j=1}^{3} \left[ \frac{\partial n k_B T_{ij}}{\partial r_j} + \frac{\partial}{\partial r_j} v_i (m^* n \overline{v_j}) \right] - e n E_i$$

$$= \left[ \frac{\partial}{\partial t} (m^* n \overline{v_i}) \right]_c$$
(2.19)

or in vector notation

$$\frac{\partial m^* n \overline{\mathbf{v}}}{\partial t} + \nabla \cdot \overline{\mathbf{v}} (m^* n \overline{\mathbf{v}}) + \nabla \cdot n k_B T - e n \mathbf{E} = \left[ \frac{\partial}{\partial t} (m^* n \overline{\mathbf{v}}) \right]_c$$
 (2.20)

where

$$\underline{T} = \sum_{i=1}^{3} \sum_{j=1}^{3} T_{ij} \mathbf{a}_i \mathbf{a}_j .$$

T is a tensor, and  $a_i$  and  $a_j$  are unit vectors. Assuming T is scalar, i.e. T = TI, then the moment conservation equation (2.20) becomes

$$\frac{\partial m^* n \overline{\mathbf{v}}}{\partial t} + \nabla \cdot \overline{\mathbf{v}} (m^* n \overline{\mathbf{v}}) = e n \mathbf{E} - \nabla (n k_B T) + \left[ \frac{\partial}{\partial t} (m^* n \overline{\mathbf{v}}) \right]_c$$
 (2.21)

or using (2.6), (2.21) can be rewritten as

$$\frac{\partial \overline{\mathbf{v}}}{\partial t} + \overline{\mathbf{v}} \cdot \nabla \overline{\mathbf{v}} + \frac{1}{m^* n} \nabla (nk_B T) - \frac{e}{m^*} \mathbf{E} = \left[ \frac{\partial \overline{\mathbf{v}}}{\partial t} \right]_c$$
 (2.22)

where the collision term was written as

$$\left[\frac{\partial \overline{\mathbf{v}}}{\partial t}\right]_{c} = \frac{1}{m^{*}n} \left[\frac{\partial}{\partial t} (m^{*} n \overline{\mathbf{v}})\right]_{c} - \frac{\overline{\mathbf{v}}}{n} \left[\frac{\partial n}{\partial t}\right]_{c}.$$
 (2.23)

In (2.21),  $m^* n \overline{v}$  is the momentum density. The left-hand side is the rate of change plus the outflow of momentum density. The right-hand side represents the force

exerted by the electric field and by the particle pressure  $nk_BT$ , and the rate of momentum density change due to collisions.

Using (2.17), (2.18), and  $P = nk_BT = nk_BTL$ , the second-order moment equation (2.15) reduces to

$$\frac{\partial}{\partial t} \left( \frac{3}{2} n k_B T + \frac{1}{2} m^* n \overline{v}^2 \right) + \nabla \cdot \left[ \left[ \frac{3}{2} n k_B T + \frac{1}{2} m^* n \overline{v}^2 \right] \overline{v} + Q + n k_B T \overline{v} \right]$$

$$- \mathbf{J} \cdot \mathbf{E} = \left[ \frac{\partial}{\partial t} (n \langle \frac{1}{2} m^* v^2 \rangle) \right]_c$$
(2.24)

where  $J = en \overline{v}$  is the current density. Using

$$W = \frac{3}{2}nk_BT + \frac{1}{2}m^*n\bar{v}^2 = n\xi$$
 (2.25)

$$\xi = \frac{3}{2}k_BT + \frac{1}{2}m^*\bar{\nu}^2 \tag{2.26}$$

$$\mathbf{S} = (W + nk_B T)\overline{\mathbf{v}} + \mathbf{Q} \tag{2.27}$$

and

$$\left[\frac{\partial W}{\partial t}\right]_c = \left[\frac{\partial}{\partial t} (n < \frac{1}{2} m^* v^2 >)\right]_c \tag{2.28}$$

(2.24) can be written as

$$\frac{\partial W}{\partial t} + \nabla \cdot \mathbf{S} - \mathbf{J} \cdot \mathbf{E} = \left[ \frac{\partial W}{\partial t} \right]_c$$
 (2.29)

$$\frac{\partial W}{\partial t} + \nabla \cdot (\overline{\mathbf{v}}W) = e n \, \overline{\mathbf{v}} \cdot \mathbf{E} - \nabla \cdot (\overline{\mathbf{v}}nk_B T) - \nabla \cdot \mathbf{Q} + \left[ \frac{\partial W}{\partial t} \right]_c \tag{2.30}$$

where  $\xi$  is average electron energy and S is the flux of energy flow. These two equations are equivalent expressions of the energy conservation equation. (2.30) contains on the left-hand side the rate of change plus the outflow of kinetic energy density W. On the right-hand side the first term is the energy supplied by the electric field, the second term is the work performed by the particle pressure, the third term is the divergence of the heat flow Q, and last term is the rate of change of kinetic energy density due to collisions.

(2.6), (2.21), and (2.30) are the first three moment equations for the conservation of particles, momentum, and energy (see [16 equations (1), (2), (3)]). The hydrodynamic transport model solves the three moment equations with some appropriate assumptions.

#### 2.3 Relationship Between HTM and DDM

The improved accuracy of the HTM as compared to the drift-diffusion model (DDM) can be demonstrated by showing the assumptions necessary to derive the DDM from the first two moment equations. The DDM model does not consider the energy moment equation as it assumes the energy is always at its equilibrium value.

For any quantity X, the relaxation time approximation for the scattering term reads

$$\left[\frac{\partial X}{\partial t}\right]_c = -\frac{X - X_0}{\tau_X} \tag{2.31}$$

where  $X_0$  is the value X at equilibrium and  $\tau_X$  is the relaxation time for X quantity. For the momentum relaxation time approximation,  $\overline{\mathbf{v}} = 0$  at equilibrium. For the energy relaxation time approximation for scattering terms, e = -q for the case of electrons, and

$$\frac{\overline{\mathbf{v}}}{\tau_m} \gg \frac{\partial \overline{\mathbf{v}}}{\partial t} + \overline{\mathbf{v}} \cdot \nabla \overline{\mathbf{v}} \quad , \tag{2.32}$$

(2.22) reduces to

$$\frac{1}{m^* n} \nabla (nk_B T) + \frac{q}{m^*} \mathbf{E} = -\frac{\overline{\mathbf{v}}}{\tau_m(\xi)} .$$

Rearranging terms gives

$$\overline{\mathbf{v}} = -\left[\mu_n(\xi)\mathbf{E} + \frac{k_B \mu_n(\xi)}{q} \nabla T + \frac{k_B T \mu_n(\xi)}{qn} \nabla n\right]$$
(2.33)

where  $\mu_n(\xi) = \frac{q \tau_m(\xi)}{m^*}$  is the electron mobility. Applying the two central approximations of DDM to (2.33), i.e., (1) carrier temperature - lattice temperature equilibrium  $(T = T_0)$ , where  $T_0$  is room temperature or lattice temperature, and (2) stationary relation between electric field E and electron energy  $\xi$ , (2.33) can be reduced to

$$\overline{\mathbf{v}}_n = -\left[\mu_n(E)\mathbf{E} + D_n(E)\frac{1}{n}\nabla n\right]$$
 (2.34)

where  $D_n(E) = \mu_n(E) \frac{k_B T}{q}$ .  $D_n$  is the electron diffusion coefficient. In (2.34),  $\mu_n(\xi)$  and  $D_n(\xi)$  have been replaced by  $\mu_n(E)$  and  $D_n(E)$  respectively due to the stationary assumption.

Using (2.33), the current density expression for HTM becomes

$$\mathbf{J}_{n} = e n \, \overline{\mathbf{v}}_{n} = q \left[ n \, \mu_{n}(\xi) \mathbf{E} + \frac{n k_{B} \, \mu_{n}(\xi)}{q} \, \nabla T + \frac{k_{B} T \, \mu_{n}(\xi)}{q} \, \nabla n \right]. \tag{2.35}$$

Using the velocity equation (2.34) the current density expression becomes

$$\mathbf{J}_n = en \nabla_n = q(n \mu_n(E) \mathbf{E} + D_n(E) \nabla n)$$
 (2.36)

which is the well known current density expression for DDM.

Comparison of (2.35) and (2.36) shows the fundamental difference between these two models. The DDM neglects the current due to temperature gradient which may be comparable in size with the other terms in equation (2.35). Also, DDM assumes locally field dependent mobility which may result in large errors for submicrometer device. The errors occur because of the time it takes for the electrons to reach stationary status, and if the time is compatible with the transient time of the electron travelling through the channel, then the non-stationary effect should be taken into account.

Besides the BTE or the moment equations, Poisson's equation is solved to obtain the potential distribution. The Poisson equation for unipolar (electron) semiconductors is

$$\nabla^2 \psi = -\frac{q}{\epsilon} (N_D - n) \tag{2.37}$$

where  $\psi$  is electrostatic potential,  $\varepsilon$  is the dielectric permittivity of the material,  $N_D$  is the doping, and n is electron concentration. The electric field  $\mathbf{E}$  is obtained directly from the potential using the relationship

$$\mathbf{E} = -\nabla \mathbf{\psi} \quad . \tag{2.38}$$

Therefore, the difference between solving DDM and HTM can be logically described in Figure 2.2. The comparison between HTM and DDM for the velocity component due to electric field may result in three cases:

- (1)  $v = \mu(\xi)E < \mu(E)E$ , non-stationary and undershoot.
- (2)  $v = \mu(\xi)E = \mu(E)E$ , stationary.
- (3)  $v = \mu(\xi)E < \mu(E)E$ , non-stationary and overshoot.

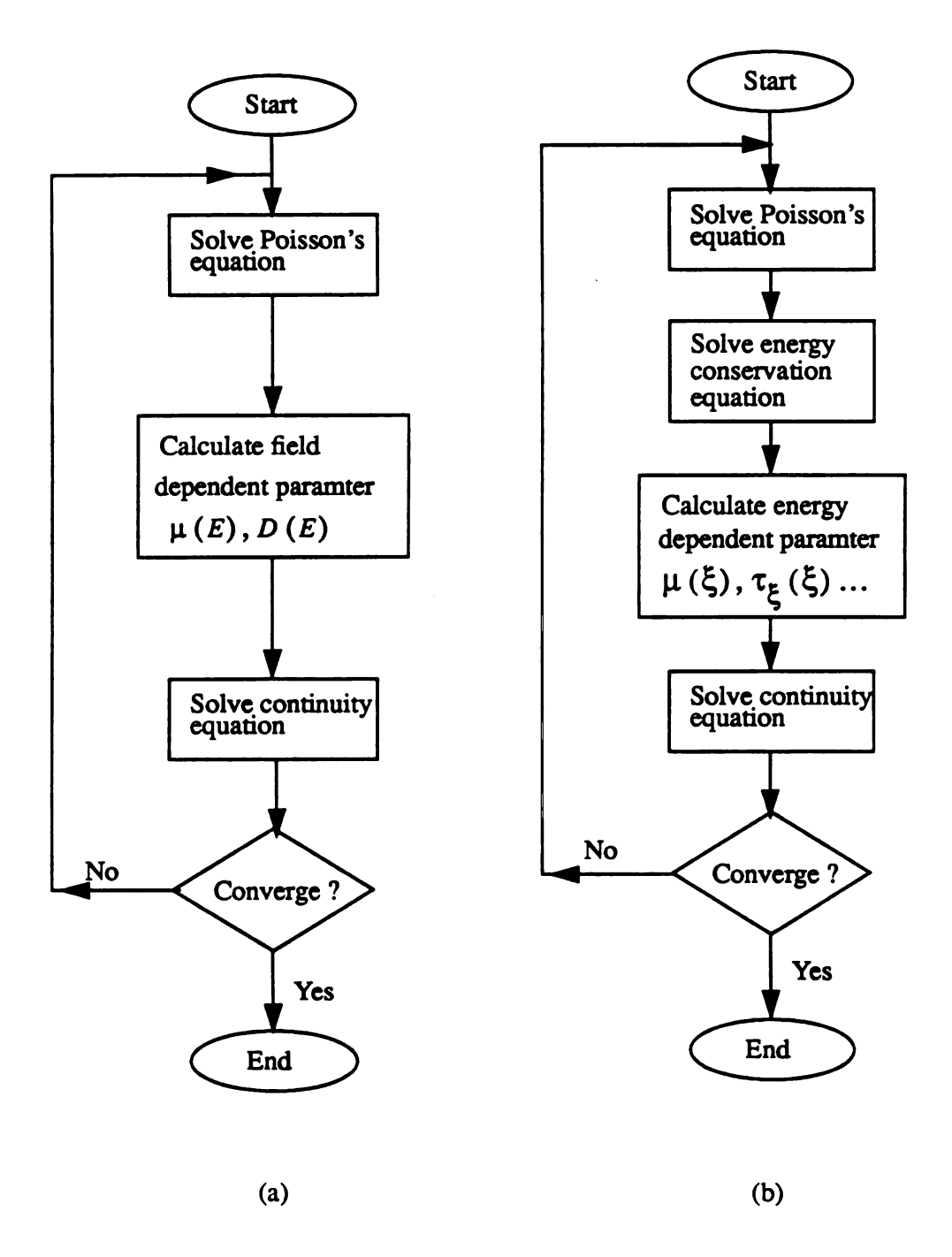


Figure 2.2. Computer flow chart for (a) drift diffusion model, (b) hydrodynamic transport model.

If the electric field varys slowly in space and time as in the case of long channel devices operating at low frequencies, then the non-stationary effect is not important. If the electric field varys rapidly in space and time, then the non-stationary effect is important and the electron energy has to be determined using the energy conservation equation.

## 2.4 GaAs MESFET Simulation

The three moment conservation equations based on solving the Boltzmann's transport equation have been developed in Section 2.2 for the single valley. In the case of multivalley semiconductors, these equations must be written in each valley. However, the generation of transport equations for electrons in multivalleys leads to a highly complex non-linear model. The problem is too complicated to be of any practical use and is simplified considerably by deriving a single equivalent electron gas, whose parameters are described by weighted averages of the electron population in each valley as obtained from steady-state Monte Carlo simulations. Even though GaAs is a three valley material, some researchers have used a two valley model [18,19]. Using a two-valley model, the single electron gas model uses the following quantities [20]:

$$n = n_{L} + n_{U}$$

$$v = (1 - F_{U}(\xi))v_{L} + F_{U}(\xi)v_{U}$$

$$m^{*} = (1 - F_{U}(\xi))m_{L}^{*} + F_{U}(\xi)m_{U}^{*}$$

$$\xi = (1 - F_{U}(\xi))\xi_{L} + F_{U}(\xi)(\Delta \xi_{UL} + \xi_{U})$$
(2.39)

where L denotes the lower conduction band valley, U denotes the equivalent upper valleys,  $F_U(\xi) = n_U/(n_L + n_U)$  is upper valley fraction, and  $\Delta \xi_{UL}$  is the energy separation between minima of the lower valley and upper valleys. The energy reference for  $\xi_L$  and  $\xi_U$  are the respective valleys. The conservation equations of the single electron gas model with the relaxation times approximation are [20,21]

$$\frac{\partial n}{\partial t} + \nabla \cdot (n \, \mathbf{v}) = 0 \tag{2.40}$$

$$\frac{\partial \mathbf{v}}{\partial t} + \mathbf{v} \cdot \nabla \mathbf{v} + \frac{q \mathbf{E}}{m^*(\xi)} + \frac{1}{m^*(\xi)n} \nabla (nk_B T(\xi)) = -\frac{\mathbf{v}(\xi)}{\tau_m(\xi)}$$
(2.41)

$$\frac{\partial(n\,\xi)}{\partial t} + \nabla \cdot n\,\mathbf{v}(\xi + k_B\,T(\xi)) + \nabla \cdot \mathbf{Q} = -qn\,\mathbf{v}\cdot\mathbf{E} - n\frac{\xi - \frac{3}{2}k_B\,T_0}{\tau_{\xi}(\xi)} \tag{2.42}$$

with

$$\xi = \frac{1}{2}m^{*}(\xi)v^{2} + \frac{3}{2}k_{B}T(\xi) + F_{U}(\xi)\Delta\xi_{UL} . \qquad (2.43)$$

The model equations (2.40)-(2.43) still need further simplification in practical use for compound semiconductors. There is a diversity in these models caused by making different assumptions as reviewed below.

Feng and Hintz [8] neglected heat flow Q and employed a relationship between  $\xi$  and T given by

$$\xi = \frac{1}{2}m^*v^2 + \frac{3}{2}k_BT \ . \tag{2.26}$$

The  $F_U(\xi)\Delta\xi_{UL}$ , though comparable in magnitude with  $\xi$  when electrons become hot, has also been neglected. This approximation is often made by authors working on the modeling of compound semiconductor devices [7,8].

The next simplification made by several authors [6,9-11] is to neglect the time derivative term  $(\frac{d\mathbf{v}}{dt})$  and the convective term  $\mathbf{v}\cdot\nabla\mathbf{v}$  in the momentum conservation equation. This gives

$$\mathbf{v} = -\left[\mu(\xi)\mathbf{E} + \frac{k_B \mu(\xi)}{q} \nabla T + \frac{k_B T \mu(\xi)}{qn} \nabla n\right]. \tag{2.33}$$

The bar over v has been dropped for simplicity. Hereafter, the bar is always dropped out.

Curtice and Yun [9] developed a carrier temperature model which used

$$\mathbf{v} = -\left[\mu(T)\mathbf{E} + \frac{1}{n}(\nabla \frac{k_B T}{q}\mu(T)n)\right]. \tag{2.44}$$

They showed the simulation results using (2.44) are similar to those generated using the simpler form

$$\mathbf{v} = -\left[\mu(T)\mathbf{E} + \frac{1}{n}(\frac{k_B T}{q}\mu(T)\nabla n)\right]. \tag{2.45}$$

This is based on the assumption that the diffusion current in (2.44) is generally a sufficiently small part of the total conduction current.

A further simplification of the momentum and energy conservation equations (2.41) and (2.42) frequently used in semiconductor device models is to assume that spatial variations are small. This reduces these equations to [5]

$$\frac{d(m^*(\xi)\mathbf{v})}{dt} = -q \mathbf{E} \frac{m^*(\xi)\mathbf{v}}{\tau_{-}(\xi)}$$
 (2.46)

and

$$\frac{d\xi}{dt} = -q \,\mathbf{v} \cdot \mathbf{E} - \frac{\xi - \xi_0}{\tau_{\xi}(\xi)} \ . \tag{2.47}$$

These equations neglect any diffusion contribution due to  $\nabla n$  or  $\nabla T$  in the momentum conservation equation, and they neglect any spatial variations in the energy conservation equation. Hence, this model is not suited to modeling Schottky barrier devices.

The models which use  $F_U(\xi)\Delta\xi_{UL}$  in (2.43) can be found in Cook and Frey [6], and Curtice and Yun [9]. Cook and Frey use the thermal energy according to the equation

$$\frac{3}{2}k_BT = \xi - F_U(\xi)\cdot\Delta\xi_{UL} \tag{2.48}$$

where  $\xi$  is the total energy and  $\Delta \xi_{UL}$  is the energy separation between the lower and

upper valley. This relation can be used to modify the momentum conservation equation (2.41) to obtain a model for multi-valley semiconductors, the new velocity is given by

$$\mathbf{v} = -\frac{\tau_m}{m^*} \left\{ q \mathbf{E} + \frac{2}{3} \left[ 1 - \Delta \xi_{UL} \frac{\partial F_U(\xi)}{\partial \xi} \right] \nabla \xi + \frac{2}{3n} \left[ \xi - F_U(\xi) \Delta \xi_{UL} \right] \nabla n \right\}. \tag{2.49}$$

In this research, (2.48) has been replaced by

$$\frac{3}{2}kT = \xi - U_p \tag{2.50}$$

where  $U_p$  is the average potential energy due to the fraction of particles in the L and X valleys, so (2.49) will be replaced by

$$\mathbf{v} = -\frac{\tau_m}{m^*} \left\{ q \mathbf{E} + \frac{2}{3} \left[ 1 - \frac{\partial U_p(\xi)}{\partial \xi} \right] \nabla \xi + \frac{2}{3n} \left[ \xi - U_p(\xi) \right] \nabla n \right\}. \tag{2.51}$$

If we define the ratio of thermal kinetic energy to total energy r by

$$r(\xi) = \frac{\frac{3}{2}k_BT}{\xi} = \frac{\xi - U_p(\xi)}{\xi}$$
, (2.52)

then (2.51) can be rewritten as

$$\mathbf{v} = -\frac{\tau_m}{m^*} \left\{ q \mathbf{E} + \frac{2}{3} \nabla (r(\xi)\xi) + \frac{2}{3n} r(\xi)\xi \nabla n \right\}. \tag{2.53}$$

(2.53) provides an alternative for numerical implementation by switching  $U_p(\xi)$  to  $r(\xi)$ .

The heat flux term in the energy conservation equation is expressed by assuming [16]

$$\mathbf{Q} = -\kappa \nabla T \tag{2.54}$$

with the Wiedeman-Franz relation used for thermal conductivity  $\kappa[12,22]$ 

$$\frac{\kappa(\xi)}{qn\mu(\xi)} = \left(\frac{k_B}{q}\right)^2 \Delta(\xi)T . \qquad (2.55)$$

 $\Delta(\xi)$  is a dimensionless number of order unity given by [12]

$$\Delta(\xi) = \frac{\left[\frac{\langle \tau \xi^3 \rangle}{\langle \tau \xi \rangle} - \left(\frac{\langle \tau \xi^2 \rangle}{\langle \tau \xi \rangle}\right)^2\right]}{(k_B T)^2}$$
(2.56)

where  $\tau(\xi)$  is the energy-dependent relaxation time of a particular type of collision [12]. Many authors have neglected the heat flux term while other authors have kept this term, in this work the heat flux is retained in order to study its effect.

## 2.5 Energy-Dependent Parameter Calculation.

The energy transport model used here requires the stationary average values of electron velocity  $v_{ss}$ , average total energy  $\xi$ , and average potential energy  $U_p$  as functions of the electric field. A steady state three-valley Monte Carlo simulation for homogeneous doping was performed to get their values. The simulator uses a three valley model for the conduction band of GaAs. Only the electron transport is considered in the simulator, hole transport is not included. The three valley model includes the  $\Gamma$ , L and X valleys as shown in Figure 2.3. Each individual band is treated as a non-parabolic band with an energy-crystal momentum relationship given by

$$E(1+\alpha E) = \frac{\hbar^2 k^2}{2m^*}$$
 (2.57)

where E is the energy,  $\alpha$  is the non-parabolic factor, k is the crystal momentum and  $m^*$  is the effective mass. The values of  $\alpha$  and  $m^*$  are different for each of the three valleys.

The simulator uses the particle simulation techniques so that each of scattering mechanisms can be included individually to more accurately represent the physics of the electron transport process. The scattering scattering mechanisms included are

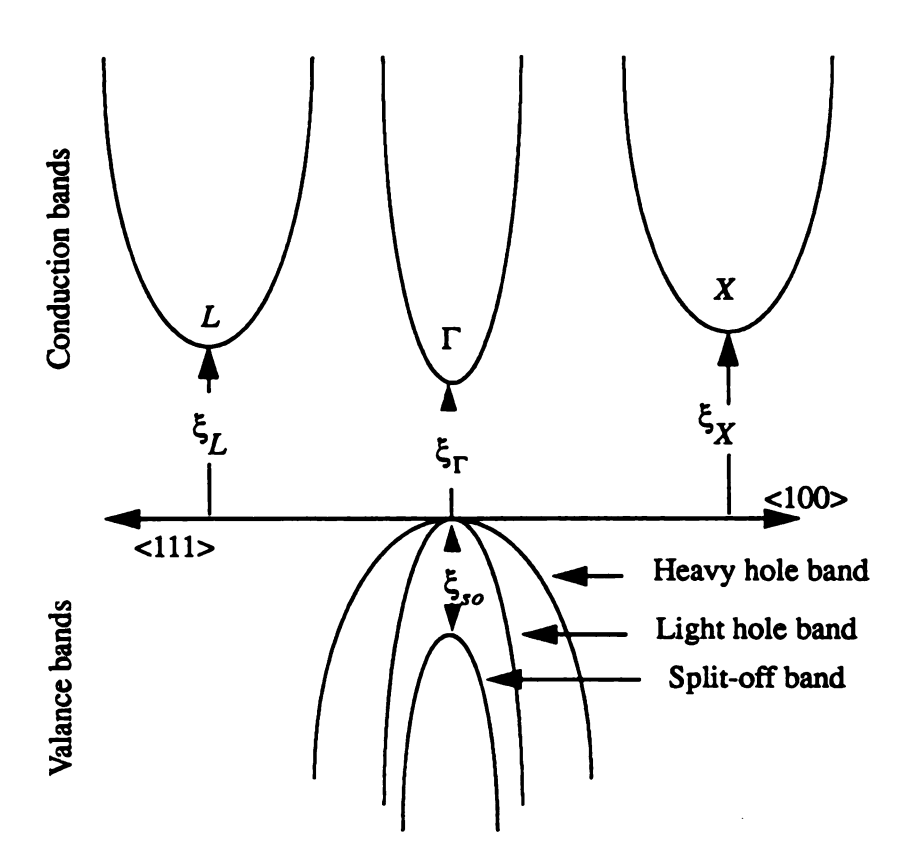


Figure 2.3. GaAs band structure.  $\xi_{\Gamma}$ ,  $\xi_{L}$  and  $\xi_{X}$  represent energies of the extremum of the  $\Gamma$ , L, X and split-off bands, respectively.

acoustic phonon scattering, optical phonon scattering, intervalley scattering, and ionized impurity scattering. Each of the phonon scattering processes may occur by phonon absorption and phonon emission. The particular electron scattering process which occurs is determined by a statistical process using random numbers. The average scattering rate (# collisions/unit time) is calculated and used to determine the probability of each scattering process. The probabilities are then used in combination with a random number generator to determine which scattering mechanism occurs[2].

The stationary results,  $v_{ss}$  versus E,  $\xi$  versus E, and  $U_p$  versus E, for a doping of  $N_D = 2 \times 10^{17} \ cm^{-3}$ , and a lattice temperature of  $T_0 = 300^o \ K$  are depicted in Figure 2.4.

The steady-state relationship of equations (2.41) and (2.42) for homogeneous case can be written as [8]

$$\tau_m(\xi) = \frac{m^*(\xi)v_{ss}(\xi)}{qE(\xi)}$$
 (2.58)

and

$$\tau_{\xi}(\xi) = \frac{\xi - \xi_0}{qE(\xi)v_{xx}(\xi)} . \tag{2.59}$$

Note that  $v_{ss}(\xi)$  and  $m^*(\xi)$  can be calculated since  $\xi(E)$  is known.

Equation (2.58) can be rearranged to treat  $\frac{\tau_m(\xi)q}{m^*(\xi)}$  as a variable  $\mu(\xi)$  giving [6]

$$\mu(\xi) = \frac{\nu_{ss}(\xi)}{E(\xi)} \ . \tag{2.60}$$

The mobility  $\mu(\xi)$ , the energy relaxation time  $\tau_{\xi}(\xi)$ , and the ratio of thermal kinetic energy to total energy  $r(\xi)$  as function of energy are depicted in Figure 2.5.

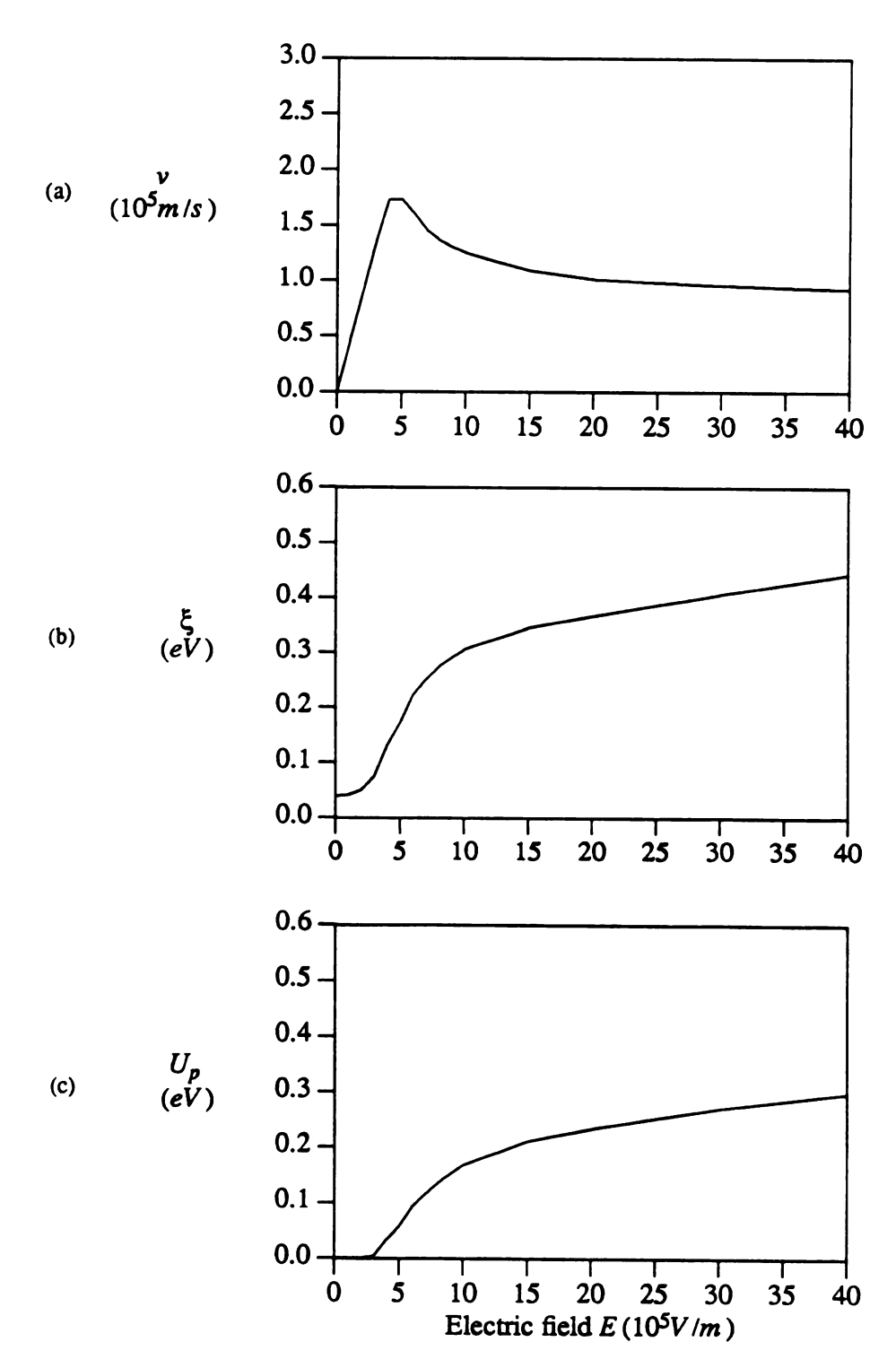


Figure 2.4. Results of Monte Carlo simulation for GaAs with  $N_D = 2 \times 10^{17} cm^{-3}$  and  $T_0 = 300^{\circ} K$ : (a) average electron velocity  $\nu$ , (b) total electron energy  $\xi$ , and (c) electron potential energy  $U_p(\xi)$  versus electric field E.

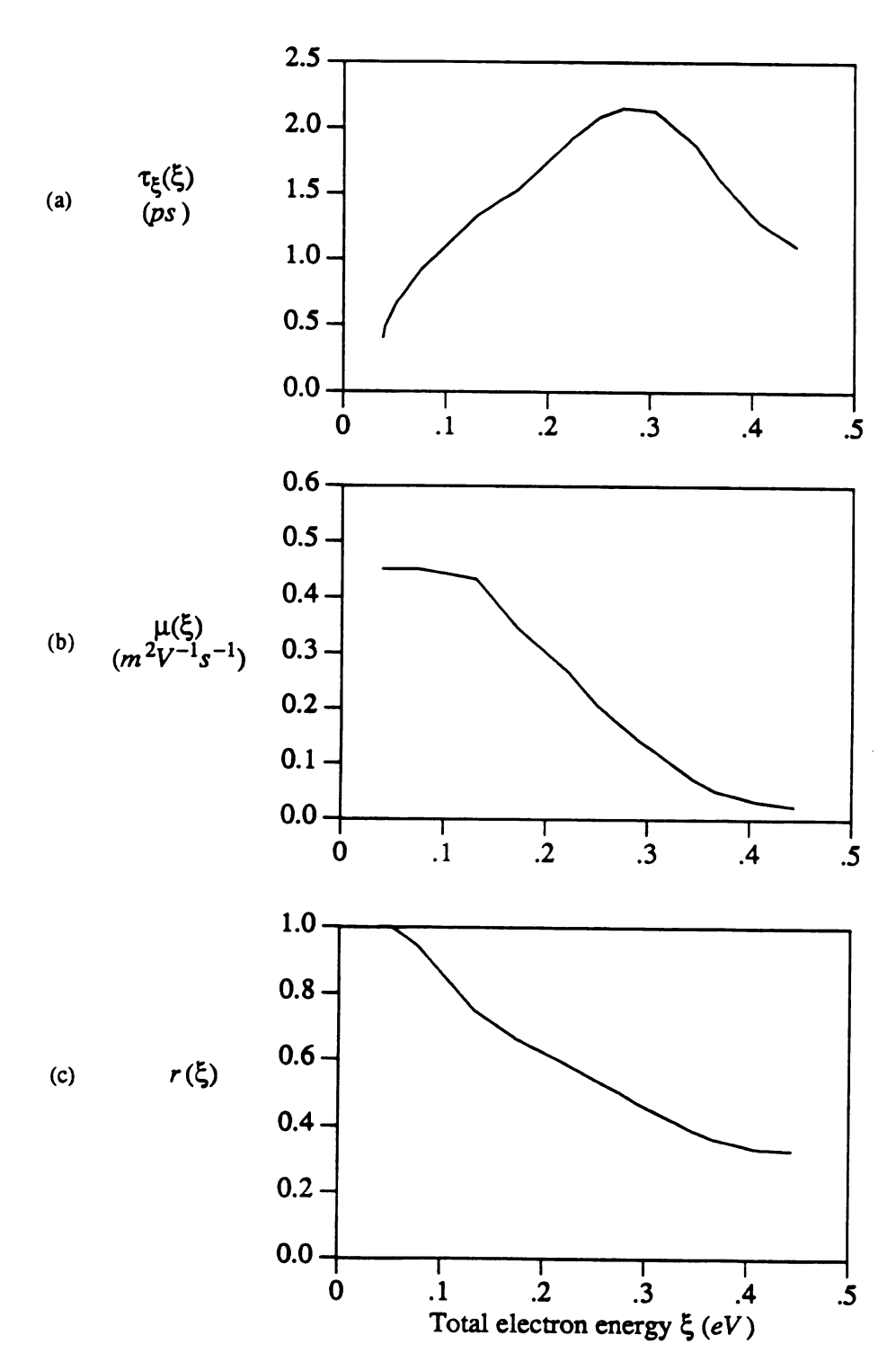


Figure 2.5. Results of Monte Carlo simulation for GaAs with  $N_D = 2 \times 10^{17} cm^{-3}$  and  $T_0 = 300^{\circ} K$ : (a) electron energy relaxation time  $\tau_{\xi}(\xi)$ , (b) electron mobility  $\mu(\xi)$ , and (c) ratio of thermal energy to total energy,  $r(\xi)$ , versus electron total energy  $\xi$ .

# **CHAPTER 3**

# NUMERICAL SOLUTION OF THE SEMICONDUCTOR EQUATIONS

In general it is not possible to obtain closed-form expressions which describe satisfactorily the operation of modern semiconductor devices. Therefore, numerical techniques are used to solve the full set of semiconductor equations over a specified domain.

The most common numerical techniques used to solve the set of partial differential equations which constitute the semiconductor equation are finite-difference, finite-element, and box-integration techniques.

### 3.1 Finite-Difference Method

The continuous derivatives of the semiconductor equations are replaced by discretized finite-difference approximation derived from truncated Taylor series. The Poisson equation in two-dimensions is usually discretized using a 'five-point' difference approximation which gives (see Figure 3.1)

$$\frac{\frac{\psi_{i+1,j} - \psi_{i,j}}{a_i} - \frac{\psi_{i,j} - \psi_{i-1,j}}{a_{i-1}}}{\frac{a_i + a_{i-1}}{2}} + \frac{\frac{\psi_{i,j+1} - \psi_{i,j}}{b_j} - \frac{\psi_{i,j} - \psi_{i,j-1}}{b_{j-1}}}{\frac{b_j + b_{j-1}}{2}}$$

$$= -\frac{q}{\varepsilon} \left( N_{Di,j} - n_{i,j} \right)$$
(3.1)

where  $N_D$ , n, and  $\varepsilon$  are defined in (2.37).

The finite-difference discretization of the current continuity equation is more crucial due to the electron concentration exponentially depending on the potential. For the DDM, the Scharfetter and Gummel scheme [23] provides the electron current density as

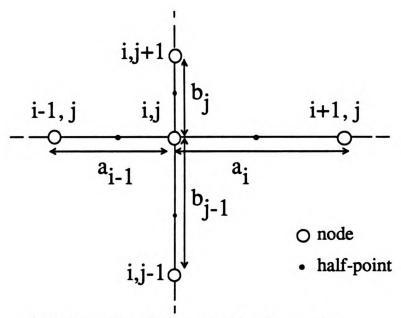


Figure 3.1. Finite-difference mesh point notation

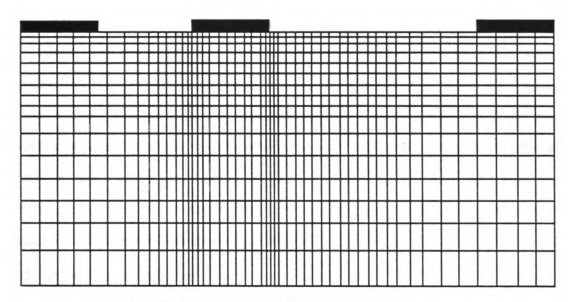


Figure 3.2. Non-uniform finite-difference mesh

$$J_{n,i+\frac{1}{2}} = -\frac{qD_n}{a_i} \left\{ n_{i+1}B \left[ \frac{q}{k_B T} (\psi_{i+1} - \psi_i) \right] - n_i B \left[ \frac{q}{k_B T} (\psi_i - \psi_{i+1}) \right] \right\}$$
(3.2)

where  $a_i$  is the mesh spacing between x = i and x = i+1, and B(x) is the Bernoulli function

$$B(x) = \frac{x}{e^x - 1}. ag{3.3}$$

Equation (3.2) allows the electron density to follow an exponential variation between mesh points. The DC electron continuity equation reads

$$\nabla \cdot \mathbf{J} = qU \tag{3.4a}$$

$$\frac{J_{x,i+\frac{1}{2}} - J_{x,i-\frac{1}{2}}}{\frac{a_i + a_{i-1}}{2}} + \frac{J_{y,j+\frac{1}{2}} - J_{y,j-\frac{1}{2}}}{\frac{b_j + b_{j-1}}{2}} = qU$$
(3.4b)

where U is the net recombination rate. The subscript n for J has been neglected for unipolar devices without any ambiguity. It is straightforward to construct the discretized continuity equation (3.4b) using the discretized current density equation (3.2).

Finite-difference techniques applied to semiconductor modeling are well established and there is considerable information available on the stability and convergence properties of these schemes. A major disadvantage of the finite difference technique when compared with the finite-element method, is that the requirement for a finer mesh in one specific area of the device necessitates the presence of a finer mesh in other parts of the device (see Figure 3.2). This leads to a surplus of nodes in regions which could have a relatively course mesh.

#### 3.2 Finite-Element Method

The finite-element method is fundamentally quite different from the finitedifference method. The domain requiring analysis is sub-divided using piecewise approximations to produce a mesh with m nodes at intersections of the mesh as shown

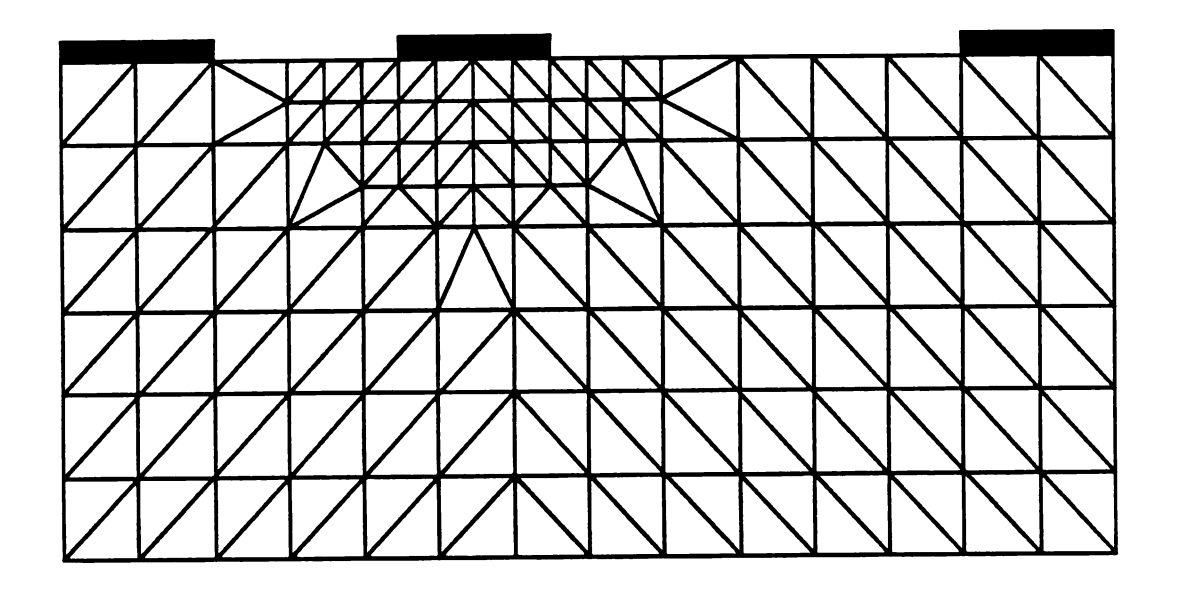


Figure 3.3. Finite-element mesh.

in Figure 3.3. The basis of the finite-element method is to approximate the solution in each element. This method was not generally applied to semiconductor device modeling until the early 1970's when Barnes and Lomax [24] reported one of the first two-dimensional finite-element simulations which was used to model a short gate-length GaAs metal-semiconductor field-effect transistor (MESFET). A finite-element discretization for the drift-diffusion model is discussed in Appendix A.

An important advantage of the finite-element method over the finite-difference schemes is that there is no additional complication introduced by using elements of different size. Finite-element methods provide a flexible means of investigating semiconductor devices with non-planar geometries and regions of highly nonlinear field and carrier distributions. The principal disadvantages of the finite-element method compared with the finite-difference approach are that initially more effort is required to implement the technique and that the stability and convergence criteria are not as well understood for the semiconductor equations. Additionally it is difficult to develop special finite-element schemes which are competitive with the exponentially fitted finite-difference method.

### 3.3 Box-integration method

Box-integration methods [25,26] link exponentially fitted carrier concentrations to the finite-element method which divides the simulated domain into elements. This is the technique used in this investigation and it is described in this section.

The general semiconductor equation can be expressed as

$$\nabla \cdot F(u, \dot{u}) = c(u, \dot{u}) \tag{3.5}$$

where F represents any physical flow quantity like electric flux density D, current density J, or energy flux S, and u represents the unknown state variables which are being solved, e.g.  $(\psi, n, \xi)$ . The divergence theorem states for a generalized function F that the volume integral transforms into the surface integral given by the relationship,

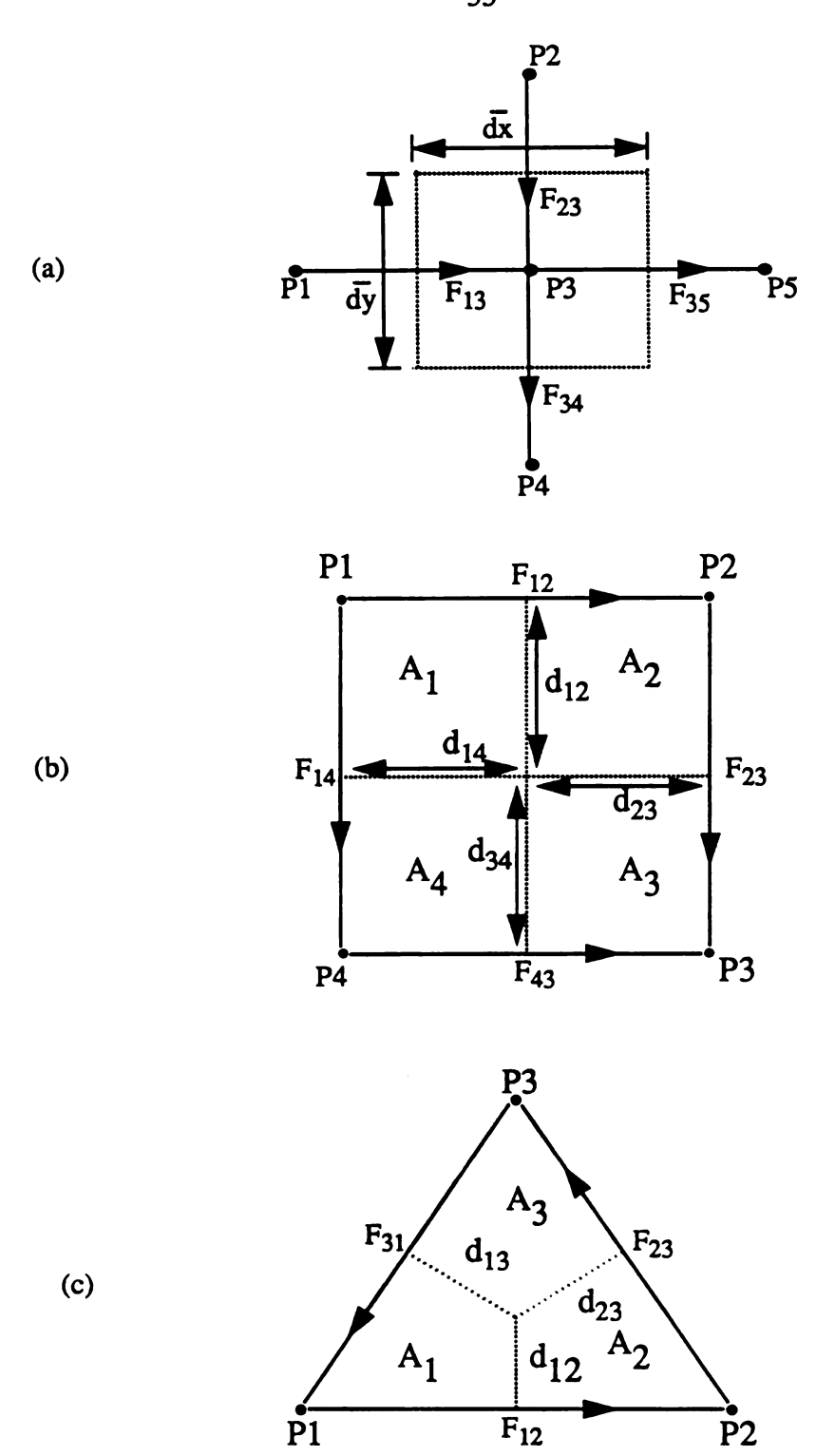


Figure 3.4 Box-integration method based on (a) point basis, (b) rectangular element basis, and (c) triangular element basis.

$$\int_{\text{vol}} \nabla \cdot F dv = \int_{\text{surf}} F \cdot \vec{a} dA \tag{3.6}$$

where  $\vec{a}$  is the outgoing unit vector normal to surface dA. Applying (3.6) to (3.5) gives

$$\int_{\text{surf}} F \cdot \vec{a} dA = \int_{\text{vol}} c dv . \tag{3.7}$$

In the case of two dimensions, (3.7) becomes

$$\int_{I} F \cdot \vec{a} dl = \int_{A} c dx dy . \tag{3.8}$$

The numerical application can be understood with the following examples.

Example 1: By adopting nomenclature shown in Figure 3.4(a) and by treating (3.8) on a point basis, the discretized form for (3.8) is

$$(F_{35} - F_{13})\overline{dy} + (F_{34} - F_{23})\overline{dx} = c_3(\overline{dx}\,\overline{dy}). \tag{3.9}$$

Example 2: By treating (3.8) on a rectangular element basis as shown in Figure 3.4(b), the discretized form for (3.8) is

$$F_{12}d_{12} + F_{14}d_{14} = c_1A_1$$
 for point P1,  
 $F_{23}d_{23} - F_{12}d_{12} = c_2A_2$  for point P2,  
 $-F_{23}d_{23} - F_{43}d_{34} = c_3A_3$  for point P3,  
 $F_{43}d_{34} - F_{14}d_{14} = c_4A_4$  for point P4. (3.10)

Example 3: By treating (3.8) on a triangular element basis as shown in Figure 3.4(c), the discretized form for (3.8) is

$$F_{12}d_{12} - F_{31}d_{13} = c_1A_1$$
 for point P1,  
 $F_{23}d_{23} - F_{12}d_{12} = c_2A_2$  for point P2,  
 $F_{31}d_{31} - F_{23}d_{23} = c_3A_3$  for point P3. (3.11)

Usually the F's are either electric flux density D, current density J, or the energy flux S. The next task to use this method for computer simulation is discretizing F efficiently and stably. First, it is simple for D,

$$D_{ij} = \varepsilon E_{ij} = \varepsilon \frac{\Psi_i - \Psi_j}{h_{ii}}$$
 (3.11b)

where  $h_{ij}$  is the spacing between nodes i and j. For the DDM, the Scharfetter-Gummel (S-G) technique is applied for J according to equation (3.2). For the case of HTM, the modified S-G technique for both J and S will be discussed in Section 3.5.

This hybrid method, which can be understood as a finite-difference method on a triangular element or rectangular element, has been proven to work satisfactorily for many applications [27,28]. The box-integration method allows exponentially fitted carrier concentrations similar to the finite-difference method. The finite-box method is a good choice to discretize semiconductor equation for devices with non-planar geometries and regions of highly nonlinear field and carrier distributions. It has been implemented in the FIELDAY [27] and PISCES [28] programs.

# 3.4 Scaling

Since the unknown variables ( $\psi, n, \xi$ ) in the basic equations (2.40)-(2.43) are of greatly different orders of magnitude, it is appropriate to scale the unknown variables and parameters to O(1) for numerical considerations. Some scaling factors for DDM are discussed in Selberherr[26]. In this research, the scaling factors used are

summaried in Table 3.1.

The Poisson equation (2.37) and the moment equations (2.40)-(2.43) are transformed into the following equations for numerical simulation in scaled form. The scaled equations are

$$\nabla \cdot (\lambda^2 \nabla \psi) = -(N_D - n) \tag{3.12}$$

$$\frac{\partial n}{\partial t} - \nabla \cdot \mathbf{J} = 0 \tag{3.13}$$

and

$$\frac{\partial(n\,\xi)}{\partial t} + \nabla \cdot \mathbf{S} = \mathbf{J} \cdot \mathbf{E} - n \frac{\xi - \xi_0}{\tau_{\xi}(\xi)} \tag{3.14}$$

with

$$\mathbf{J} = \mu(\xi)(n\mathbf{E} + \nabla(nT)) = -n\mathbf{v} \tag{3.15}$$

$$S = n v(\xi + T) - \Delta T n \mu(\xi) \nabla T$$
 (3.16)

$$\xi = \frac{3}{2}T + U_p(\xi) \tag{3.17}$$

and

$$\lambda^2 = \frac{\varepsilon}{(x_0^2 q C_0/\psi_0)} \tag{3.18}$$

where the assumption (2.32) is used, and (3.17) neglects  $(1/2)m^*v^2$  [6,9]. Notice that there is no  $k_B$  or q parameters shown in (3.12)-(3.17), and that the magnitudes of all the scaled unknown variables are closed to O(1). The discretization for J, S, and  $J \cdot E$  will be the topic of the next section.

# 3.5 Modified Scharfetter-Gummel technique for J and S

The current density J and energy flux S are expressed in (3.15) and (3.16) respectively. This section will discuss the discretization of (i) J, (ii) S, and (iii)  $J \cdot E$ 

Table 3.1 Scaling factors.

quantity	symbol	value
x,y (position)	<i>x</i> <sub>0</sub>	max(x,y)
ψ (voltage)	$\Psi_0$	$\frac{k_BT_0}{q}$
n,N <sub>D</sub> (doping)	$C_0$	$\max(N_D(x,y))$
μ(ξ) (mobility)	$\mu_0$	$max(\mu(\xi))$
$t$ , $\tau_m$ , $\tau_\xi$ (time)	$t_0$	$\frac{{x_0}^2}{\mu_0\psi_0}$
T (temperature)	$T_{0}$	$T_0 = 300^o K$
ξ (energy)	ξo	$k_B T_0 = q \Psi_0$
J (current density)	$J_0$	$\frac{q\mu_0C_0\psi_0}{x_0}$
S,Q (energy flux)	$S_0$	$J_0 \psi_0 = (\frac{q  \mu_0 C_0 \psi_0}{x_0}) \psi_0$
v (velocity)	ν <sub>0</sub>	$\frac{x_0}{t_0}$

for the box-integration technique. Note these discretization techniques can apply to both rectangular and triangular meshes.

# (i) Current density J discretization:

Following the work in Tang[22], J between points i and i+1 in Figure 3.5 can be expressed as

$$J = \mu \left[ nE + \nabla (nT) \right]$$

$$= \mu (nE + n\nabla T + T\nabla n)$$

$$= \mu \left[ n(E + \nabla T) + T\nabla n \right]$$

$$= \mu T \left[ (E + \nabla T) \frac{1}{T} n + \nabla n \right]. \tag{3.19}$$

Rearranging terms gives

$$\frac{J}{\mu T} = (E + \nabla T) \frac{1}{T} n + \nabla n$$

$$= \nabla T (\alpha + 1) \frac{1}{T} n + \nabla n$$
(3.20)

where

$$\alpha = \frac{E}{\frac{dT}{dx}} \ . \tag{3.21}$$

If  $E = -\frac{d\psi}{dx}$ ,  $\frac{dT}{dx}$ , and J are all assumed to be constant in the interval [i, i+1], (3.20) can be integrated to yield [see Appendix B]

$$J_{m} = \mu_{m} \left(\frac{dT}{dx}\right) \frac{1}{\ln \frac{T_{i}}{T_{i+1}}} \left[ n_{i} B \left(-x_{b}\right) - n_{i+1} B \left(x_{b}\right) \right]$$
(3.22)

where

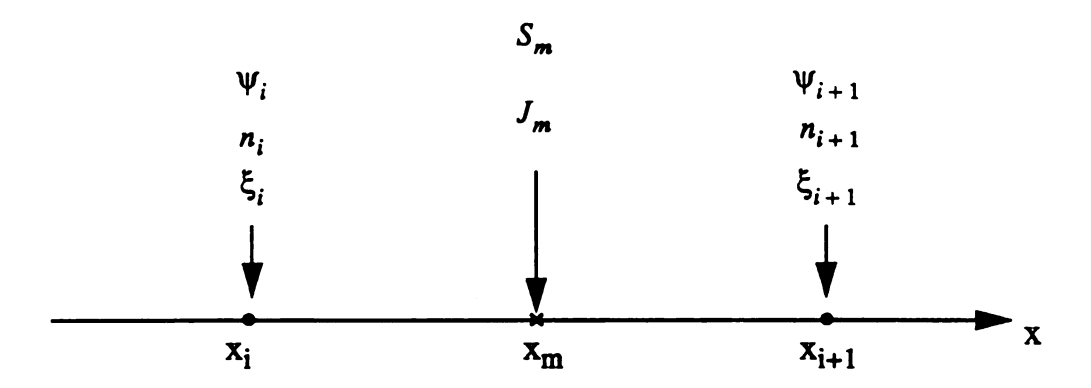


Figure 3.5. Notation for both J and S discretization. The two neighboring mesh points are  $x_i$  and  $x_{i+1}$  where  $\psi$ , n and  $\xi$  are evaluated.  $x_m$ , the midpoint between  $x_i$  and  $x_{i+1}$ , represents the location where E, J and S are evaluated.

$$x_b = (\alpha + 1)\ln\frac{T_i}{T_{i+1}} \tag{3.23}$$

The mesh point m is midway between points i and i+1.  $B(-x_b)$  and  $B(x_b)$  are Bernoulli functions defined in equation (3.3).

# (ii) Energy flux S discretization:

S can be discretized in a similar manner as J. Defining

$$\xi = \frac{3}{2}T_{\xi},\tag{3.24}$$

the percentage of thermal energy relative to total energy is given as

$$r(\xi) = \frac{\frac{3}{2}T}{\frac{3}{2}T_{\xi}} = \frac{\xi - U_{p}(\xi)}{\xi} = \frac{T}{T_{\xi}}.$$
 (3.25)

 $r(\xi)$  is an energy-dependent parameter which can be calculated from three-valley Monte Carlo simulation as described in Figure 2.5. Substituting (3.24) and (3.25) into (3.16) gives

$$S = -J(1.5T_{\xi} + T) - \Delta T n \mu \nabla T$$

$$= -\mu (nE + \nabla (nT))(\frac{1.5}{r}T + T) - \Delta T n \mu \nabla T$$

$$= -\mu (\frac{1.5}{r} + 1)T(nE + \nabla (nT)) - \Delta T n \mu \nabla T$$

$$= -\mu \delta \left[ T(nE + \nabla (nT)) + \Delta \delta^{-1} T n \nabla T \right]$$

$$= -\mu \delta \left[ T n(E + \Delta \delta^{-1} \nabla T) + T \nabla (nT) \right]$$

$$= -\mu \delta T \left[ \frac{1}{T} (T n)(E + \Delta \delta^{-1} \nabla T) + \nabla (nT) \right]$$
(3.26)

where

$$\delta = \frac{1.5}{r} + 1 \ . \tag{3.27}$$

Rearranging terms gives

$$\frac{S}{-\mu\delta T} = (E + \Delta\delta^{-1}\nabla T)\frac{1}{T}(Tn) + \nabla(nT)$$

$$= \nabla T(\alpha + \Delta\delta^{-1})\frac{1}{T}(Tn) + \nabla(nT). \qquad (3.28)$$

Again, if we make the approximation that E,  $\nabla T$ , S,  $\delta$ , and  $\Delta \delta^{-1}$  all change little in the interval [i, i+1], (4.31) can be integrated to yield [see Appendix B]

$$S_{m} = -\mu_{m} \delta_{m} \frac{dT}{dx} \frac{1}{\ln \frac{T_{i}}{T_{i+1}}} \left[ (nT)_{i} B (-x_{b}) - (nT)_{i+1} B (x_{b}) \right]$$
(3.29)

or

$$S_{m} = -\mu_{m} \delta_{m} \frac{d(rT_{\xi})}{dx} \frac{1}{\ln \frac{(rT_{\xi})_{i}}{(rT_{\xi})_{i+1}}} \left[ (nrT_{\xi})_{i} B(-x_{b}) - (nrT_{\xi})_{i+1} B(x_{b}) \right]$$
(3.30)

where

$$x_b = (\alpha + \Delta \delta^{-1}) \ln \frac{T_i}{T_{i+1}} . \tag{3.31}$$

#### (iii) J.E discretization:

A major discretization problem to be solved in HTM regards the inner product J·E, which represents the forcing term for carrier heating. The proposed discretization scheme for J·E is based on the simple vector relationship [29]

$$\mathbf{J} \cdot \mathbf{E} = -\nabla \cdot (\psi \mathbf{J}) + \psi \nabla \cdot \mathbf{J} . \tag{3.32}$$

By remembering that in the DC case,  $\nabla \cdot \mathbf{J} = qU$  with U being the net recombination rate, the second term on the right side of (3.32) can be neglected for unipolar devices to further simplify (3.32). However, in the AC case, the second term on right side of

(3.32) has to be retained because it is not zero in equation (3.13). Hence, both terms have to be included to allow DC and AC simulation even for unipolar devices. Applying the box-integration method to (3.32) is similar to the examples in Section 3.3. It is worth mentioning that (3.32) does not involve the problem of computing the current density **J** on the node; rather all the physical parameters appearing in (3.32) are either nodal values of scalar quantities or the current density through the sides emanating from the node.

# 3.6 Matrix Equation Solution

# 3.6.1 Review of Matrix Equation Methods

To simplify notation, the HTM equations can be expressed as

$$F(\psi, n, \xi) = \begin{bmatrix} F_{\psi}(\psi, n, \xi) \\ F_{n}(\psi, n, \xi) \\ F_{\xi}(\psi, n, \xi) \end{bmatrix} = 0$$
(3.33)

where  $F_{\psi}$  denotes the Poisson equation,  $F_n$  denotes the continuity equation and  $F_{\xi}$  denotes the energy conservation equation. Various numerical techniques may be used to solve for (3.33) equal zero. The two principal approaches to solving the HTM equations are the coupled method (Newton's method) and the decoupled method (Gummel's method) [30].

The Newton's method is used to linearize the partial differential equations. Given an initial guess, the solution of the non-linear equations is obtained by iterating the matrix equation

$$\begin{bmatrix}
\frac{\partial F_{\psi}}{\partial \psi} & \frac{\partial F_{\psi}}{\partial n} & \frac{\partial F_{\psi}}{\partial \xi} \\
\frac{\partial F_{n}}{\partial \psi} & \frac{\partial F_{n}}{\partial n} & \frac{\partial F_{n}}{\partial \xi} \\
\frac{\partial F_{\xi}}{\partial \psi} & \frac{\partial F_{\xi}}{\partial n} & \frac{\partial F_{\xi}}{\partial \xi}
\end{bmatrix}^{k} \begin{bmatrix}
\Delta \psi^{k} \\
\Delta n^{k} \\
\Delta \xi^{k}
\end{bmatrix} = -\begin{bmatrix}
F_{\psi}(\psi^{k}, n^{k}, \xi^{k}) \\
F_{n}(\psi^{k}, n^{k}, \xi^{k}) \\
F_{\xi}(\psi^{k}, n^{k}, \xi^{k})
\end{bmatrix}$$
(3.34)

where k denotes the iteration count. The correction vector for the k-th iteration is

given by

$$\Delta \psi^k = \psi^{k+1} - \psi^k \,, \tag{3.35a}$$

$$\Delta n^k = n^{k+1} - n^k \tag{3.35b}$$

and

$$\Delta \xi^k = \xi^{k+1} - \xi^k \ . \tag{3.35c}$$

All of the variables in the problem are allowed to change during each iteration, and all of the coupling between variables is taken into account. Due to this tight coupling, the Newton's algorithm has a fast convergence. The matrix size will be  $3N \times 3N$  (for 3-coupled equations), where N is the number of grid point.

In Gummel's method, the equations are decoupled such that each one can be regarded as an independent equation for each iteration cycle. The equations are solved and updated sequentially. At the k-th step, Gummel's method can be formally written as

$$\left[\frac{\partial F_{\psi}(\psi^{k}, n^{k}, \xi^{k})}{\partial \psi}\right] \cdot \Delta \psi^{k} = -F_{\psi}(\psi^{k}, n^{k}, \xi^{k})$$
(3.36a)

$$\left[\frac{\partial F_n(\boldsymbol{\psi}^{k+1}, n^k, \boldsymbol{\xi}^k)}{\partial n}\right] \cdot \Delta n^k = -F_n(\boldsymbol{\psi}^{k+1}, n^k, \boldsymbol{\xi}^k)$$
(3.36b)

$$\left[\frac{\partial F_{\xi}(\boldsymbol{\psi}^{k+1}, \boldsymbol{n}^{k+1}, \boldsymbol{\xi}^{k})}{\partial \boldsymbol{\xi}}\right] \cdot \Delta \boldsymbol{\xi}^{k} = -F_{\xi}(\boldsymbol{\psi}^{k+1}, \boldsymbol{n}^{k+1}, \boldsymbol{\xi}^{k}) . \tag{3.36c}$$

Note that the most recent variables are used in equations (3.36a)-(3.36c) by making use of equations (3.35a)-(3.35c). At each stage only one equation is being linearized and solved by Newton's method, so the matrix A has N rows  $\times N$  columns regardless of the number of coupled equations being solved, where N is the number of grid points.

Both the Gummel method and the Newton method produce a linear matrix equation of the form AX = B. This matrix equation can be solved by direct or iterative techniques. Two direct methods are Gaussian elimination or LU-decomposition. Three common iterative methods are Jacobi, Gauss-Seidel, and successive-over-relaxation (SOR) methods [25]. In general the matrix size A is large due to a large number of mesh points, hence a banded matrix LU decomposition solution technique is used to reduce the computation time needed to solve AX = B.

### 3.6.2 Matrix coefficient allocation and calculation

Equations (3.12)-(3.14) govern the device transport behavior. Integrating these equations gives

$$\int [\nabla \cdot (\lambda^2 \nabla \psi) + (N_D - n)] dx dy = F_{\psi}$$
(3.37)

$$\int \frac{\partial n}{\partial t} dx dy - \int \nabla \cdot \mathbf{J_n} dx dy = \int \frac{\partial n}{\partial t} dx dy + F_n = 0$$
 (3.38)

$$\int \frac{\partial n \, \xi}{\partial t} \, dx \, dy + \int [\nabla \cdot \mathbf{S} - (\mathbf{J_n} \cdot \mathbf{E} - n \frac{\xi - \xi_0}{\tau_{\xi}(\xi)})] \, dx \, dy$$

$$= \int \frac{\partial n \, \xi}{\partial t} \, dx \, dy + F_{\xi} = 0 \tag{3.39}$$

where  $F_{\psi}$ ,  $F_n$ ,  $F_{\xi}$  denote respectively the DC part of the integrated Poisson equation, continuity equation, and energy conservation equation. In particular,  $F_n$  and  $F_{\xi}$  are expressed as

$$F_n = -\int \nabla \cdot \mathbf{J_n} dx dy \tag{3.40}$$

$$F_{\xi} = \int [\nabla \cdot \mathbf{S} - (\mathbf{J_n} \cdot \mathbf{E} - n \frac{\xi - \xi_0}{\tau_{\xi}(\xi)})] dx dy . \qquad (3.41)$$

In this study, a rectangular mesh with variable mesh spacing was used as shown in Figure 3.1. Since the number of grid points in the x-direction is larger than that in the y-direction for the MESFET, the grid points are numbered as shown in Figure 3.6.

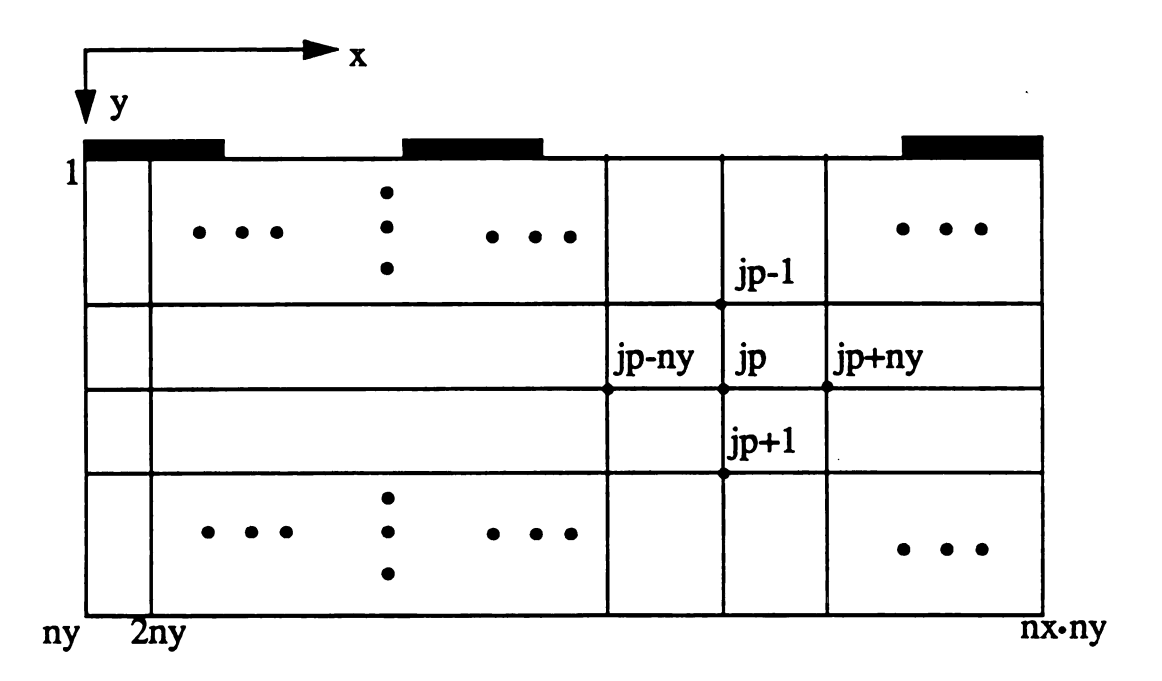


Figure 3.6. Grid number assignment for a rectangular mesh. The arrangement gives a reduced matrix of bandwidth (2ny+1) for Gummel's method and (6ny+5) for Newton's method.

The rectangular mesh can be refined using a regrid generator as described in Appendix C. Applying the box-integration method [see example 1 in Section 3.3], equations (3.37)-(3.39) can be rewritten as follow.

$$\begin{split} & \left[ (\lambda^2 \nabla \psi)_{jp,jp+ny} - (\lambda^2 \nabla \psi)_{jp-ny,jp} \right] \overline{dy} \\ & + \left[ (\lambda^2 \nabla \psi)_{jp,jp+1} - (\lambda^2 \nabla \psi)_{jp-1,jp} \right] \overline{dx} + (N_D - n)_{jp} \overline{dx} \overline{dy} = 0 \end{split}$$
(3.42)

$$\left[\frac{\partial n}{\partial t}\right]_{jp} \overline{dx} \overline{dy} - \left[ (J_{jp,jp+ny} - J_{jp-ny,jp}) \overline{dy} + (J_{jp,jp+1} - J_{jp-1,jp}) \overline{dx} \right] = 0 \quad (3.43)$$

$$\left[\frac{\partial n \xi}{\partial t}\right]_{jp} \overline{dx} \, \overline{dy} + \left[ (S_{jp,jp+ny} - S_{jp-ny,jp}) \overline{dy} + (S_{jp,jp+1} - S_{jp-1,jp}) \overline{dx} \right] - \left[ \mathbf{J_n \cdot E} - n \frac{\xi - \xi_0}{\tau_{\xi}(\xi)} \right] \overline{dx} \, \overline{dy} = 0$$
(3.44)

or they may be expressed as:

$$F_{\psi,jp}=0 (3.45)$$

$$\left(\frac{\partial n}{\partial t}\right)_{jp} d\overline{x} d\overline{y} + F_{n,jp} = 0 \tag{3.45}$$

$$\left[\frac{\partial n\xi}{\partial t}\right]_{jp} dx dy + F_{\xi,jp} = 0 \tag{3.46}$$

where  $F_{\psi,jp}$ ,  $F_{n,jp}$ ,  $F_{\xi,jp}$  denote the DC part at grid point jp in (3.42),(3.43) and (3.44), respectively. The dx and dy were defined earlier in Figure 3.4(a). The matrix equation solution of (3.42)-(3.44) is done by using either (i) Gummel's method, or (ii) Newton's method.

## (i) Gummel's method

Gummel's method solves equations (3.45)-(3.46) sequentially as shown in Figure 2.2. The matrix equation for the DC solution of the Poisson equation can be expressed

as

$$\begin{bmatrix}
\frac{\partial F_{\psi,1}}{\partial \psi_{1}} & \frac{\partial F_{\psi,1}}{\partial \psi_{2}} & \cdots & \frac{\partial F_{\psi,1}}{\partial \psi_{N}} \\
\vdots & \vdots & \ddots & \vdots \\
\frac{\partial F_{\psi,N}}{\partial \psi_{1}} & \frac{\partial F_{\psi,N}}{\partial \psi_{2}} & \cdots & \frac{\partial F_{\psi,N}}{\partial \psi_{N}}
\end{bmatrix}
\begin{bmatrix}
\Delta \psi_{1} \\
\Delta \psi_{2} \\
\vdots \\
\vdots \\
\Delta \psi_{N}
\end{bmatrix} = -
\begin{bmatrix}
F_{\psi,1} \\
F_{\psi,2} \\
\vdots \\
\vdots \\
F_{\psi,N}
\end{bmatrix}, (3.47a)$$

OT

$$A_{N\times N}X_{N\times 1} = B_{N\times 1} . ag{3.47b}$$

Similarly, the matrix equation for both continuity equation and energy equation can be easily formulated. The matrix A is a band diagonal matrix with five or less non-zero elements in each row. In equations (3.42)-(3.44) for grid point jp, the highest grid number is jp+ny, and the lowest is jp-ny, therefore the bandwidth is (2ny+1). By taking advantage of this banded property, the size of matrix A can be reduced from  $N \times N$  to  $(2ny+1)\times N$ . For example, if nx=100 and ny=20, then N=2000, and matrix A is reduced from  $2000\times2000$  to  $41\times2000$ . This means only 1/48 of the original memory space is enough, and that the computation time is reduced substantially.

One thing worth mentioning is that Gummel's method requires the addition of one more term to the main diagonal of matrix A for the Poisson equation, otherwise the iteration will not converge. This can be understood by rewritting the Poisson equation (3.12) as

$$\nabla \cdot \lambda^2 \nabla \psi^{k+1} + (N_D - n^{k+1})$$

$$= \nabla \cdot \lambda^2 \nabla \psi^{k+1} + (N_D - n^k \exp(\frac{\psi^{k+1} - \psi^k}{U_t})) = 0$$
(3.48)

where the superscript k indicates the k-th iteration and  $U_t = \frac{k_B T}{q}/\psi_0$  for the scaled Poisson equation. The added diagonal term came from the exponential dependence of

n on potential.

The coefficients in matrix A are calculated by numerical evaluation. For example,

$$A(jp,jp) = \frac{\partial F_{\psi,jp}}{\partial \psi_{jp}} = \frac{F_{\psi,jp}(\psi_{jp} + \Delta \psi_{jp}) - F_{\psi,jp}(\psi_{jp})}{\Delta \psi_{jp}}$$
(3.49)

and

$$B(jp) = -F_{\psi,jp}(\psi_{jp})$$
 (3.50)

The numerical evaluation for A causes longer computer time than analytical expression, but it provides great flexibility for changing device models. After A and B have been calculated, the matrix equation is solved by the LU-decomposition method in this study.

## (ii) Newton's method

The second approach to solving the semiconductor equations is Newton's method which solves all three equations simultaneously. This method provides the capability for the sinusoidal steady state analysis which will be presented in Chapter 5, and it allows the simulation of high current densities. However, this method requires  $3N \times 3N$  for the size of matrix A. In order to reduce the size of matrix A, the unknown variables are arranged in the following order

$$\begin{bmatrix}
\frac{\partial F_{\psi,1}}{\partial \psi_{1}} & \frac{\partial F_{\psi,1}}{\partial n_{1}} & \frac{\partial F_{\psi,1}}{\partial \xi_{1}} & \cdots & \frac{\partial F_{\psi,1}}{\partial \xi_{N}} \\
\vdots & \vdots & \ddots & \vdots & \vdots \\
\frac{\partial F_{\xi,N}}{\partial \psi_{1}} & \frac{\partial F_{\xi,N}}{\partial n_{1}} & \frac{\partial F_{\xi,N}}{\partial \xi_{1}} & \cdots & \frac{\partial F_{\xi,N}}{\partial \xi_{N}}
\end{bmatrix}
\begin{bmatrix}
\Delta \psi_{1} \\ \Delta n_{1} \\ \Delta \xi_{1} \\ \vdots \\ \Delta \psi_{N} \\ \Delta n_{N} \\ \Delta \xi_{N}
\end{bmatrix} = -\begin{bmatrix}
F_{\psi,1} \\ F_{n,1} \\ F_{\xi,1} \\ \vdots \\ F_{\psi,N} \\ F_{n,N} \\ F_{n,N} \\ F_{\xi,N}
\end{bmatrix}, (3.51a)$$

OF

$$A_{3N \times 3N} X_{3N \times 1} = B_{3N \times 1} . {(3.51b)}$$

The matrix A is also a band diagonal matrix with fifteen or less non-zero elements in each row. Instead of  $X = [\Delta \psi_1, \dots, \Delta \psi_N, \Delta n_1, \dots, \Delta n_N, \Delta \xi_1, \dots, \Delta \xi_N]^T$  which is commonly used in Newton's method [31], the rearranged X shown in (3.51a) has been used. By doing so, the matrix A is more compact in bandwidth. After a careful arrangement for matrix A to match X, the size of A can be reduced from  $3N \times 3N$  to  $(6ny+5)\times 3N$ . The reduced matrix A can save substantial memory space. For example, nx=100 and ny=20 gives N=2000, with matrix A reduced from  $6000\times 6000$  to  $125\times 6000$ . This means only 1/48 of the original memory space is used. In order to reduce the grid point number and the size of matrix A, ny should be kept as small as possible for this arrangement.

There are fifteen or less non-zero terms in matrix A for each row or each column. The non-zero terms are also evaluated numerically. The matrix equation obtained is solved by LU-decomposition as indicated for the case of Gummel's method.

# 3.7 Boundary Conditions

The above set of coupled equations are solved numerically using a boxintegration formulation on a variable spacing mesh. The solution is subject to the following boundary conditions.

(i) Neumann boundary conditions are applied to the free surfaces. The boundary conditions are

$$\frac{\partial \Psi}{\partial u_n} = 0, \quad \frac{\partial n}{\partial u_n} = 0, \quad \frac{\partial \xi}{\partial u_n} = 0$$
 (3.52)

where  $u_n$  is the normal direction. This is equivalent to

$$E_{u_n} = 0, \quad J_{u_n} = 0, \quad S_{u_n} = 0.$$
 (3.53)

(ii) Dirichlet boundary conditions are applied to the electrodes. The boundary conditions are

$$\psi = constant$$
,  $n_s = n_d = N_D$ , and  $\xi = \xi_0$  (3.54)

where  $n_s$ ,  $n_d$  and  $N_D$  are respectively carrier concentrations under the source and the drain and the doping level.

(iii) A thermionic emission-diffusion boundary condition is applied on the Schottky contact at the gate [32]. The boundary conditions are

$$\Psi = -\Phi_{bn} + V_{gs} \tag{3.55}$$

$$J = qv_r(n - N_c \exp(-\frac{q \phi_{bn}}{k_B T_0}))$$
 (3.56)

and

$$\xi = \xi_0 \ . \tag{3.57}$$

The thermionic emission-diffusion model is used to calculate the electron concentration at the Schottky contact.  $q \phi_{bn}$  is the barrier height,  $v_r$  is the effective recombination velocity, and  $N_c$  is the effective density of states in the conduction band.

#### **CHAPTER 4**

# DC SIMULATION OF MESFETS USING THE SEMICONDUCTOR HYDRODYNAMIC TRANSPORT EQUATIONS

# 4.1 Current-Voltage Characteristics Compared with Monte Carlo.

The study of small geometry GaAs MESFETs is a important application of the HTM simulator described in the previous chapters. The DC simulation of the MESFET is presented in this chapter along with the verification of the accuracy of the HTM simulator. The DC simulation of the MESFET using the HTM method has been compared to calculations using the Monte Carlo particle method. This comparison serves to verify the accuracy of the hydrodynamic transport model because the Monte Carlo method is known to include the important physics of electron transport in MESFETs. In particular, comparisons of Monte Carlo results to experimental data have shown good agreement [62]. The structure used for the simulations had  $L_{GS}$ =0.4 $\mu m$ ,  $L_{G}$  = 0.4 $\mu m$ , and  $L_{GD}$  = 0.6 $\mu m$  as shown in Figure 4.1. The device doping was a constant n-type doping of  $2.0\times10^{17}cm^{-3}$  for the active layer. The depth of the active layer was  $0.1\mu m$  and the Schottky barrier potential was  $0.75\,V$ .

The HTM model gives the current voltage characteristics shown in Figure 4.2. The HTM model used had one additional simplification to the model presented earlier in Section 3.5. This simplification was implemented to improve the convergence for higher  $V_{DS}$  values. The source of the convergence problem was the strong dependence of  $r(\xi)$  on energy for high drain voltages as shown in Figure 2.5. The difficulty occurs in the discretization of S given as

$$S_{m} = -\mu_{m} \delta_{m} \frac{d(rT_{\xi})}{dx} \frac{1}{\ln \frac{(rT_{\xi})_{i}}{(rT_{\xi})_{i+1}}} \left[ (nrT_{\xi})_{i} B(-x_{b}) - (nrT_{\xi})_{i+1} B(x_{b}) \right]$$
(3.30)

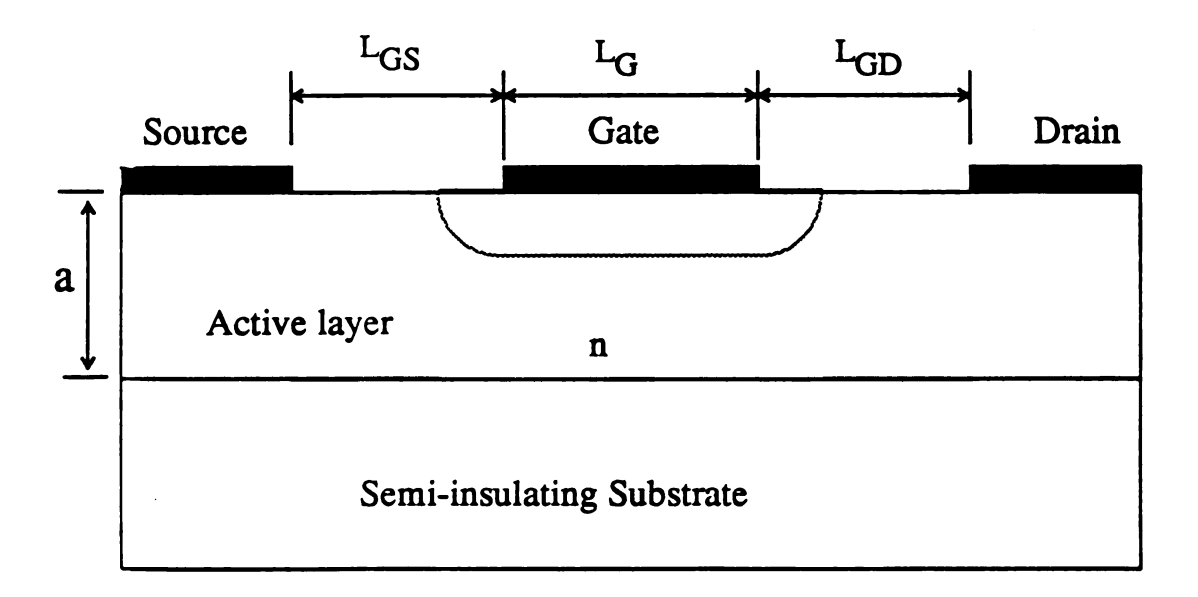


Figure 4.1 Simplifid two-dimensional MESFET geometry.

where the  $nrT_{\xi}$  terms are the unstable terms. The simplification made is that the r in the  $nrT_{\xi}$  terms is set to a constant value of  $r_s$ =0.4. This value of  $r_s$ =0.4 is an approximate value for the r shown earlier in Figure 2.5. The simplified energy flux expression becomes

$$S_{m} = r_{s} \left\{ -\mu_{m} \delta_{m} \frac{d (rT_{\xi})}{dx} \frac{1}{\ln \frac{(rT_{\xi})_{i}}{(rT_{\xi})_{i+1}}} \left[ (nT_{\xi})_{i} B (-x_{b}) - (nT_{\xi})_{i+1} B (x_{b}) \right] \right\}$$
(4.1)

The importance of the  $S_j$  term to the solution of the FET currents is in the gradient of the electron energy. The validity of the  $r_s$  approximation can be seen in Figure 4.2 where the HTM and the Monte Carlo results are compared. The other material parameters including  $r(\xi)$ ,  $\mu$  and  $t_{\xi}$  where all determined from using the one particle Monte Carlo simulator. The one modification made to the Monte Carlo data is an adjustment of the low field mobility to  $\mu_0=0.45m^2V^{-1}s^{-1}$ . This was done to match low field mobility values found in the literature [7]. The one particle Monte Carlo simulator used does not accurately simulate the low field region due to an oversimplified acoustic phonon scattering model. The acoustic phonon model used treats the acoustic phonon scattering process as an elastic process which is a valid approximation only at higher fields.

The grid structure used in the two-dimensional Monte Carlo simulator consists of small rectangles as shown in Figure 4.3. The simulator allows recess gate structures with a insulating region on each side of the gate. The simulator solves the Poisson equation using the finite difference method and it solves the Boltzmann transport equation using the Monte Carlo particle method. The boundary conditions used in the Poisson equation solution are:

# 1) Potential equals source voltage

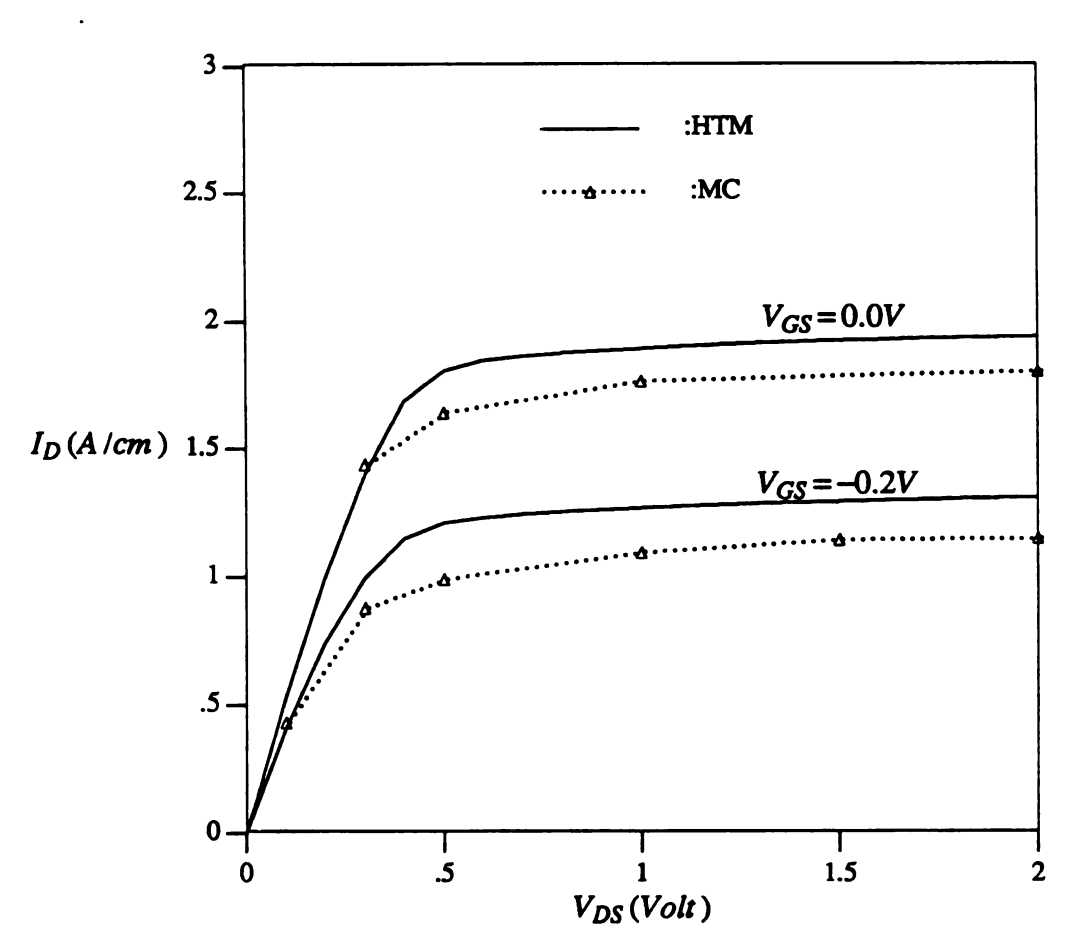


Figure 4.2. The current-voltage characteristics for both HTM and Monte Carlo.

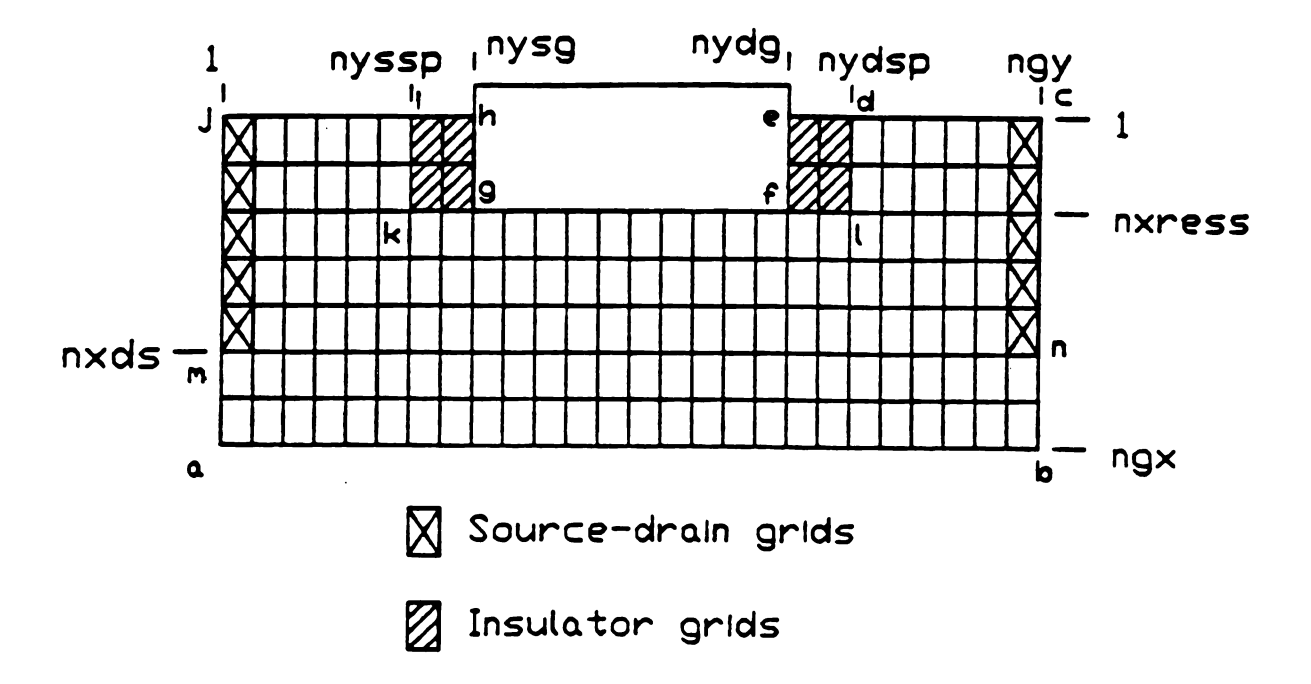


Figure 4.3. Grid structure used in the two-dimensional Monte Carlo simulation.

2) Potential equals drain voltage

n-c

3) Potential equals gate voltage

4) Normal component of electric field is zero

5) Normal component of electric flux density is constant

6) Potential equals substrate voltage

(a-b)

Note that the boundary (a-b) has two possible boundary conditions (4 or 6).

The boundary conditions for the Boltzmann transport equation solution are:

1) Reflective boundary to particles

2) Source-drain grids

At the source and drain grids, particles are added to these grid cells each time step to maintain a charge neutrality.

The computation times for the Monte Carlo particle and the HTM methods were compared. For each I-V curve with 10 points as shown in Figure 4.2, it took about 4 to 6 hours CPU time for the Monte Carlo simulation on the CONVEX C-220 computer, and it took about 5 minutes CPU time on the same computer with a grid size of 60×5 for HTM.

The typical two-dimensional distributions for the potential, the electron density, and the electron energy obtained from the HTM model are shown in Figure 4.4, Figure

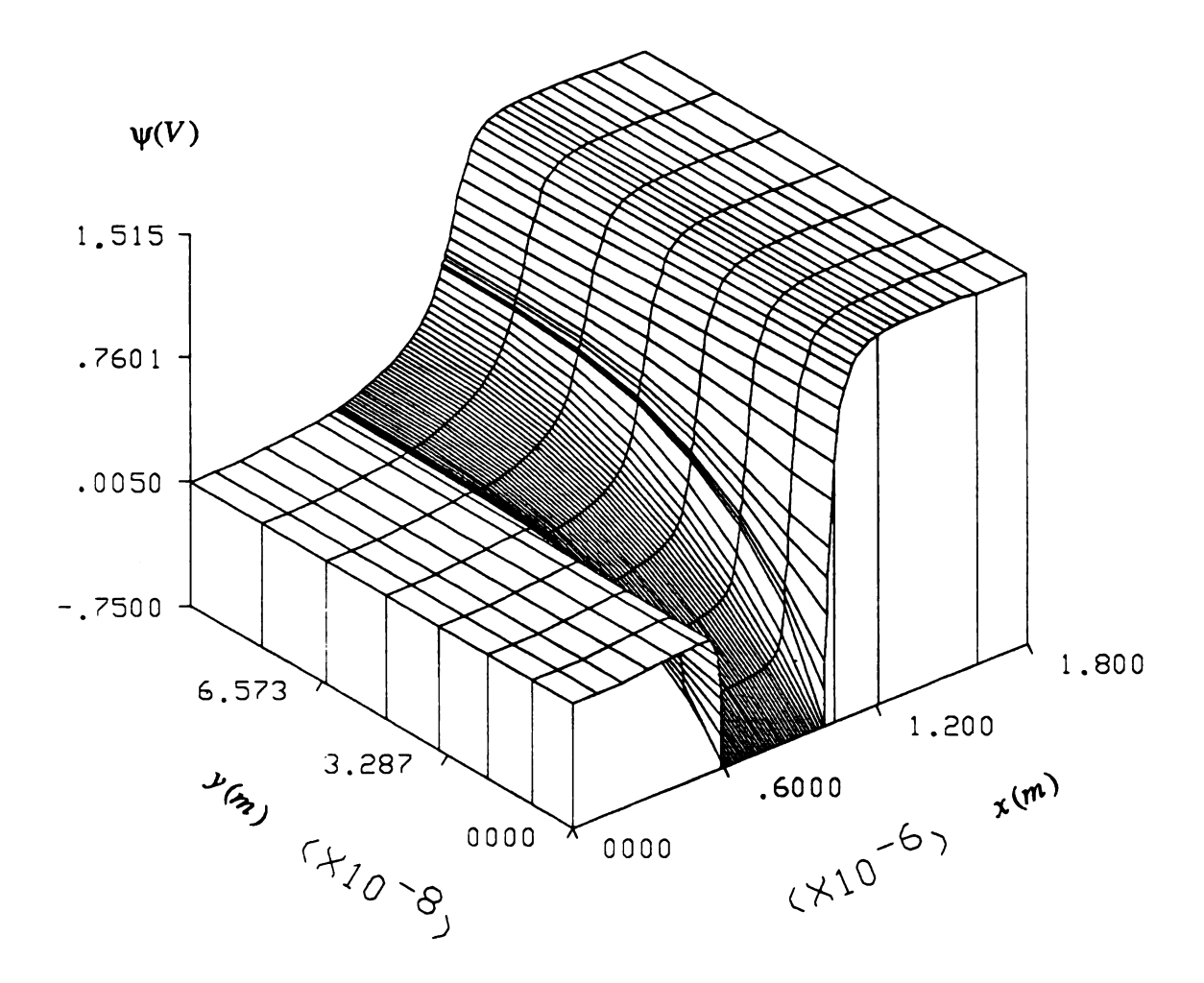


Figure 4.4. Potential distribution (V) over the entire device for  $V_{GS} = 0.0 V$  and  $V_{DS} = 1.5 V$ . The source is the front left region and the drain is the front right region. The gate extends from  $0.6 \, \mu m$  to  $1.0 \, \mu m$ .

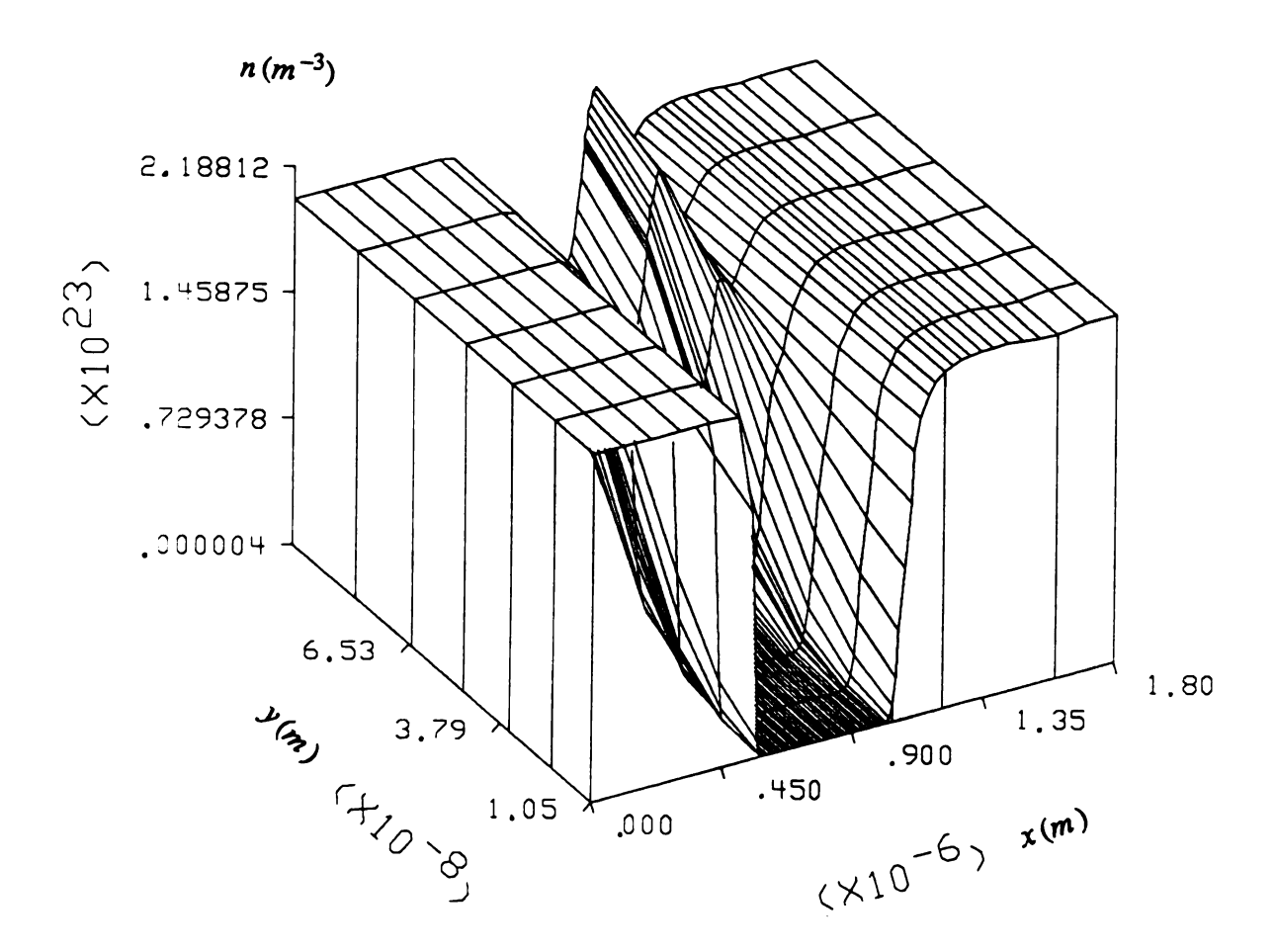


Figure 4.5. Electron density distribution  $(m^{-3})$  over the entire device for  $V_{GS} = 0.0 V$  and  $V_{DS} = 1.5 V$ . The source is the front left region and the drain is the front right region. The gate extends from  $0.6 \, \mu m$  to  $1.0 \, \mu m$ .

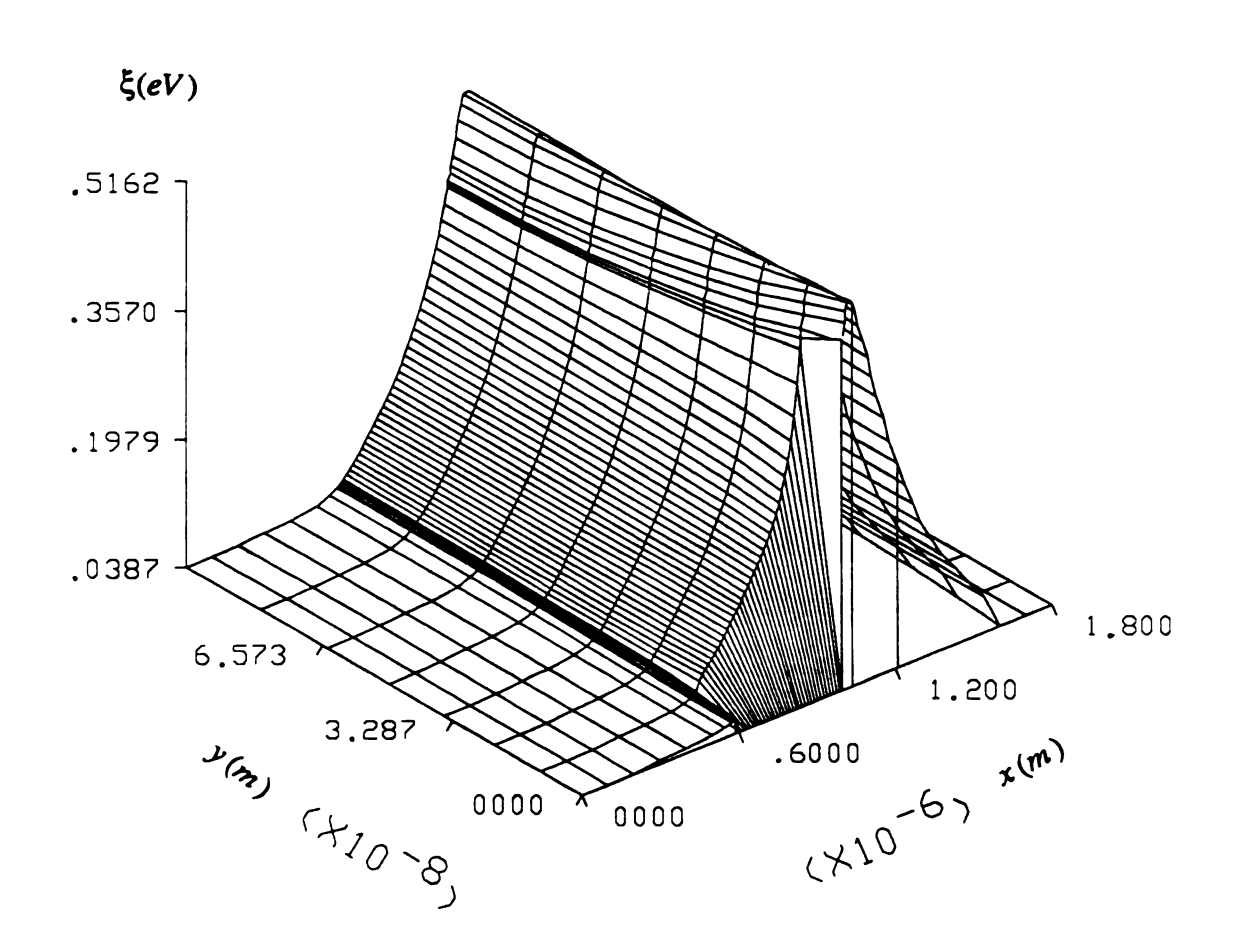


Figure 4.6. Electron energy distribution (eV) over the entire device for  $V_{GS} = 0.0 \, V$  and  $V_{DS} = 1.5 \, V$ . The source is the front left region and the drain is the front right region. The gate extends from  $0.6 \, \mu m$  to  $1.0 \, \mu m$ .

4.5 the region directly under the gate is depleted with electrons present at the bottom of the active channel. The electron concentration plot shows a dipole domain towards the drain end of the channel. This dipole domain occurs for the GaAs MESFET because of the multivalley nature of GaAs [33]. The electron energy distribution shown in Figure 4.6 has a peak energy of approximate 0.52eV.

A more detailed picture of the potential, electron density and electron energy along the lower portion of channel between the source and the drain is shown in Figure 4.7-4.9. In Figure 4.8, the dipole domain can be clearly seen. For these figures the gate extends from  $0.6 \, \mu m$  to  $1.0 \, \mu m$ .

For comparison with the field dependent mobility model, the current-voltage characteristics for DDM and HTM is shown in Figure 4.10. The DDM and HTM are compared using the same relationship for velocity versus electric field as shown earlier in Figure 2.4. Figure 4.10 shows that the HTM predicts a larger current than the DDM. The DDM calculates the mobility from the electric field resulting in a stationary relationship between velocity and electric field. The HTM calculates the mobility as a function of electron energy where the electron energy is calculated by solving the energy conservation equation. Since the electron can not gain energy instantly from the electric field, the electron energy for HTM is smaller than the energy corresponding to the local electric field model used for the DDM. Hence, the HTM has higher mobility than the DDM in the device channel. This results in the electron velocity for the HTM being higher than the stationary values used in the DDM. This higher velocity is called a non-stationary effect and it leads to higher current [6,7].

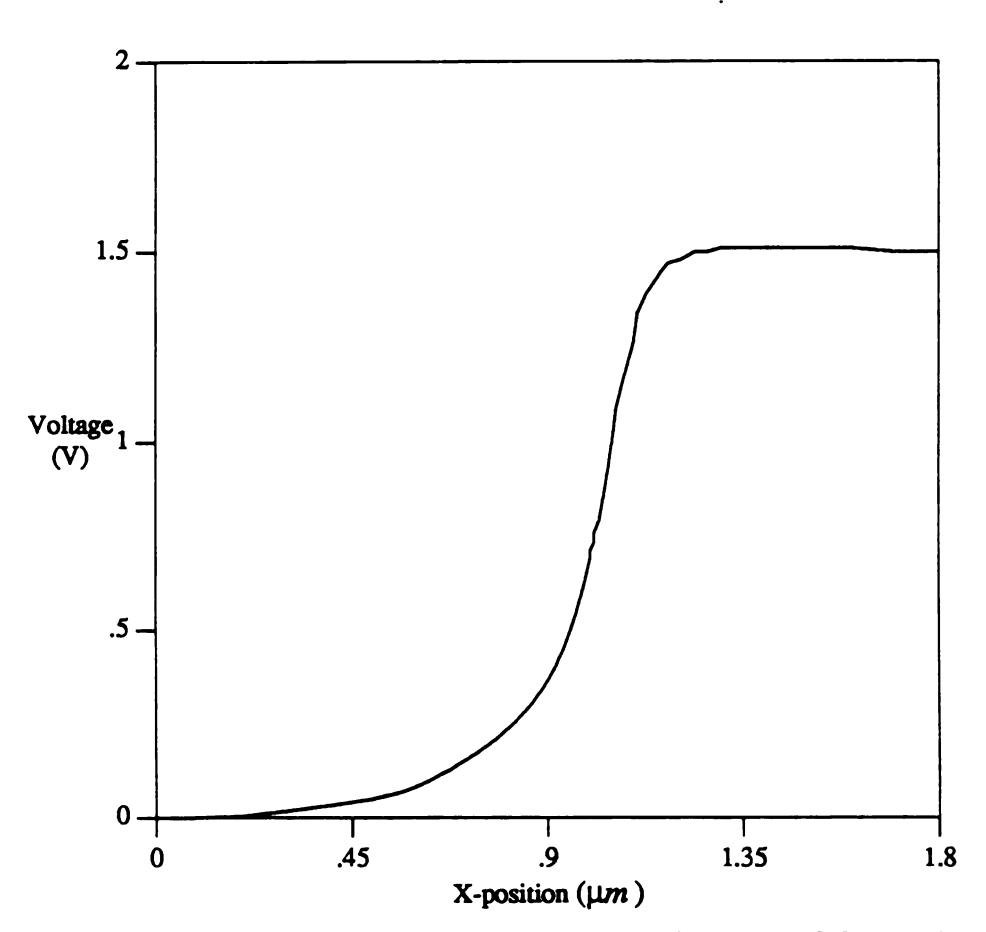


Figure 4.7. Potential distribution at y=0.1  $\mu m$  for  $V_{GS}=0.0\,V$  and  $V_{DS}=1.5\,V$ . The gate extends from 0.6  $\mu m$  to 1.0  $\mu m$ .

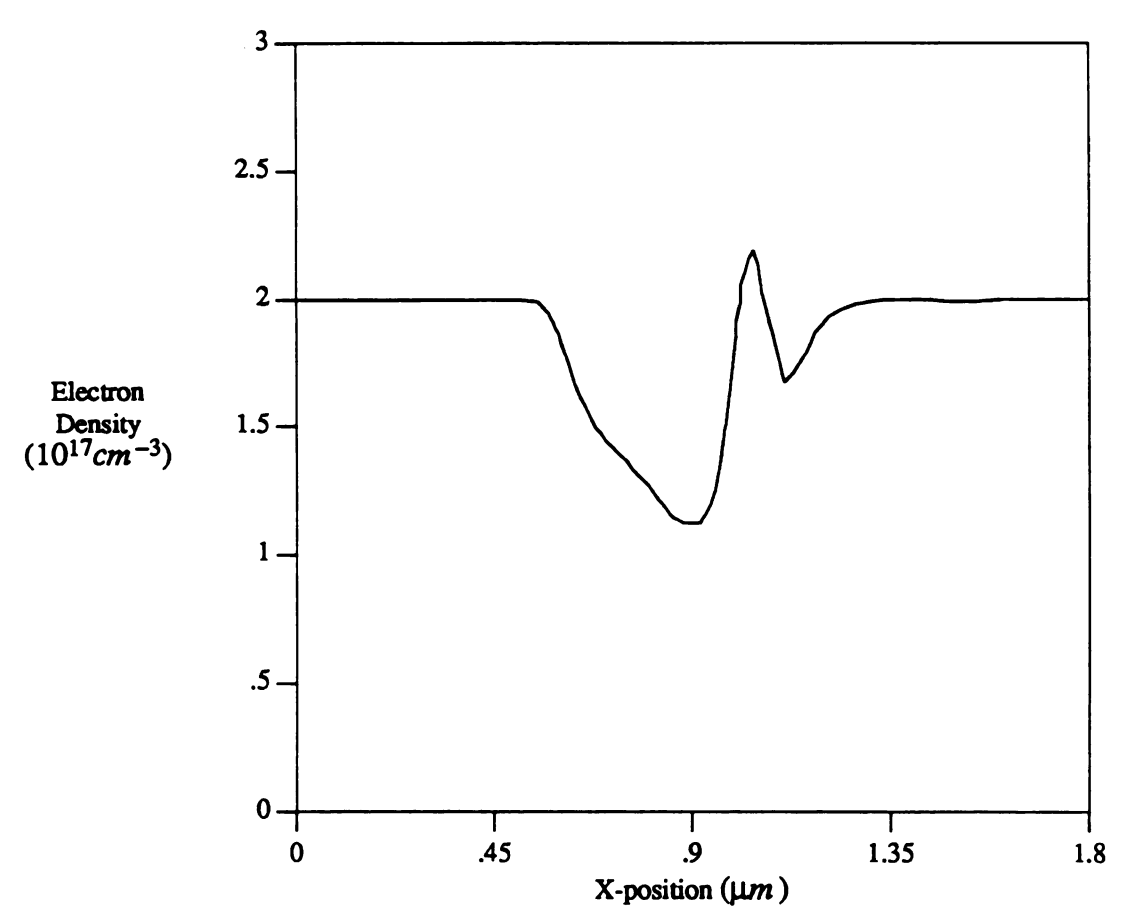


Figure 4.8. Electron density distribution at y=0.1  $\mu m$  for  $V_{GS}=0.0\,V$  and  $V_{DS}=1.5\,V$ . The gate extends from 0.6  $\mu m$  to 1.0  $\mu m$ .

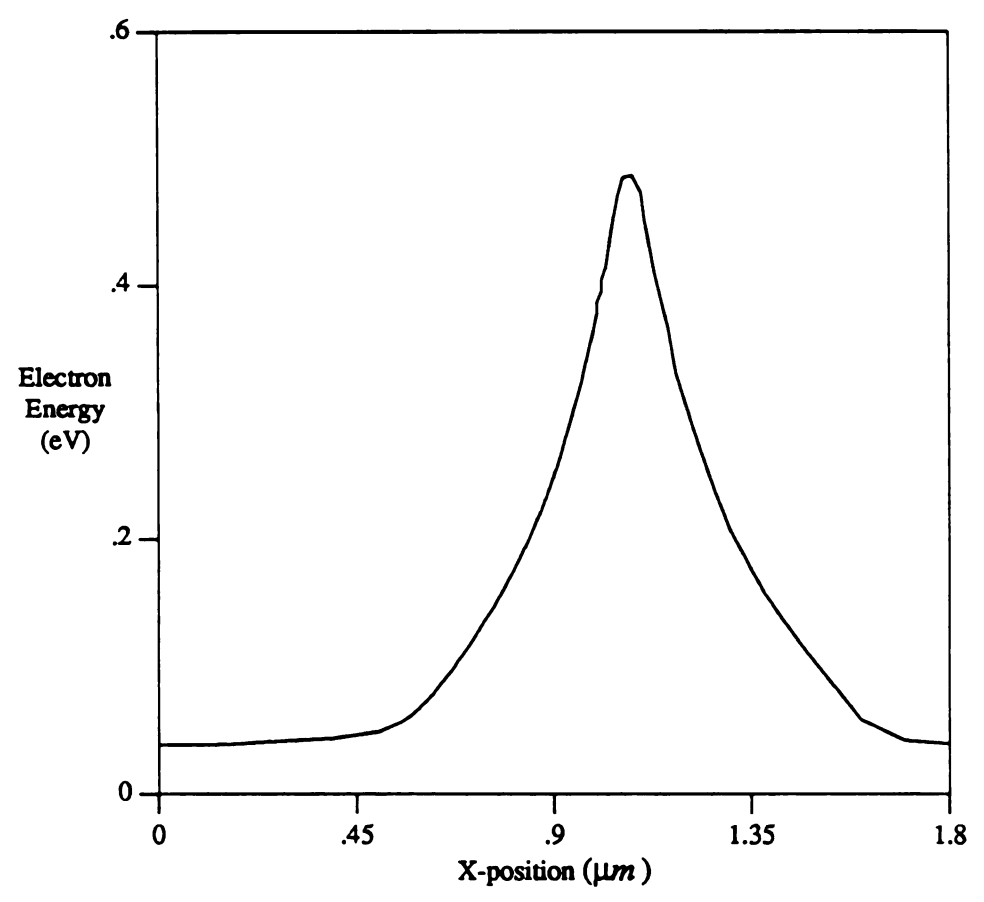


Figure 4.9. Electron energy distribution at y=0.1  $\mu m$  for  $V_{GS}=0.0\,V$  and  $V_{DS}=1.5\,V$ . The gate extends from 0.6  $\mu m$  to 1.0  $\mu m$ .

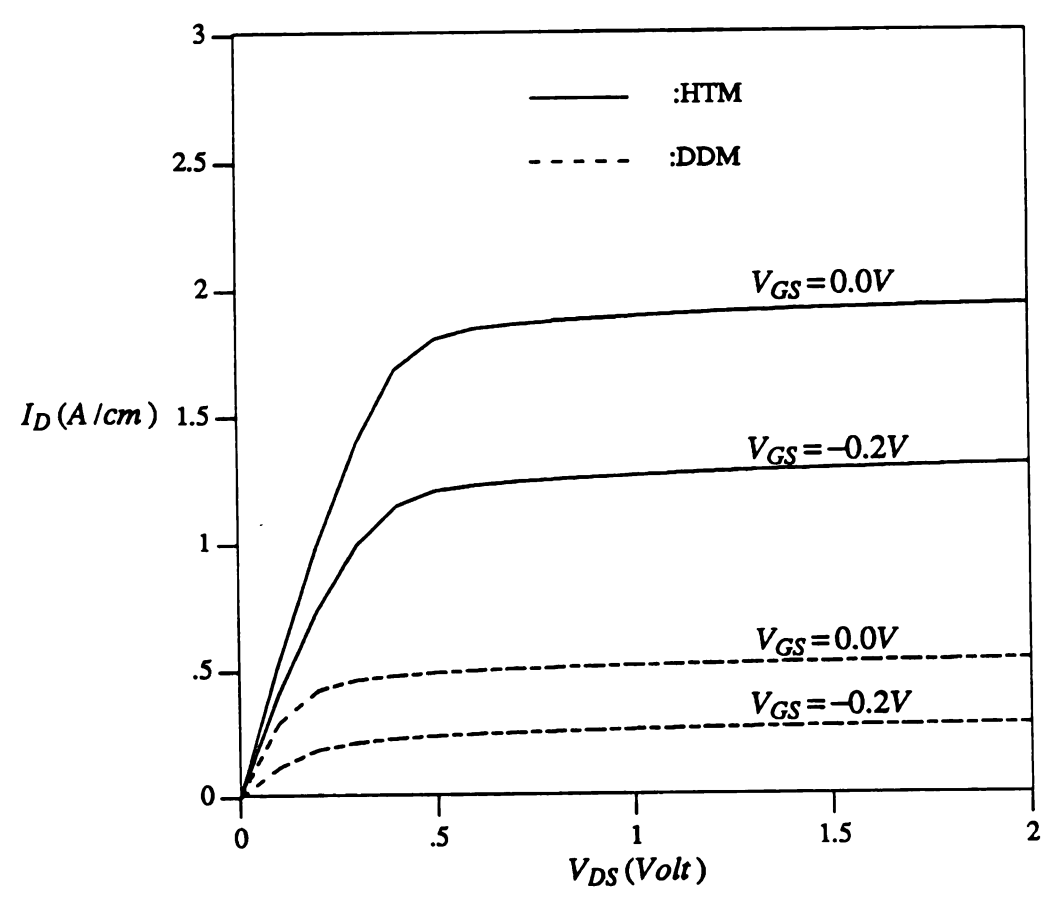


Figure 4.10. Current voltage characteristics for both HTM and DDM.

## 4.2 Source and Drain Resistance Studies of Short Channel MESFET's using Two-Dimensional Device Simulators<sup>1</sup>

One of the phenomena which is predicted by the HTM is that the electrons are at high energies as they enter the drain region shown in Figure 4.9. The high electron energy strongly influences the behavior of the parasitic drain resistance region which exists between the gate and the drain contact. A study was conducted to model the parasitic resistance regions using two dimensional device simulators.

The parasitic MESFET source and drain resistances strongly influence the MESFET's performance as the channel length of the MESFET is reduced. The increased influence of the resistances,  $R_S$  and  $R_D$ , is due to the source-to-gate length,  $L_{GS}$ , and the drain-to-gate length,  $L_{GD}$ , not decreasing proportionally as the gate length is decreased. Previous source and drain resistance studies[34-40] have modeled the source resistance and drain resistance as constants which are independent of the applied bias. One exception to using a bias independent model is the gate voltage dependent model developed by Byun and coworkers[41]. These previous models are used for circuit simulator models with resistance values extracted from measured current-voltage characteristics. The use of a bias independent source and drain resistance model neglects three effects which become important in short-channel MES-FETs. The first effect is the increase of the electric field along the current flow path in the parasitic resistor regions as the channel length decreases. The electric field can become large enough to yield field-dependent mobility effects. The second effect is the increased impact of the lateral gate depletion region as the device geometries are reduced. The third effect is the energy relaxation of the carriers as they leave the channel region and move into the drain resistance region. These three effects cause

<sup>&</sup>lt;sup>1</sup> This section contains a paper published in *IEEE Trans. on Electron Devices*, vol. ED-37, pp. 775-780, 1990.

changes in the parasitic resistance of the transistor as a function of the transistor operating bias.

This section will examine the source and drain resistance in short channel silicon and GaAs MESFETs using two-dimensional simulator tools including a drift-diffusion simulator, an energy transport simulator and a Monte Carlo particle simulator. This approach allows a careful study of the transistor's internal potential, electric field, electron concentration and currents which yields an improved understanding of the source and drain resistance for both design improvement of the transistor and for development of models for circuit simulation. The models used for circuit simulation typically describe the transistor as a parasitic source resistance, a parasitic drain resistance and an intrinsic MESFET model. Section 4.2.1 describes the use of a device simulator to study source and drain resistance and compares the resistor values extracted using other source and drain resistance definitions. Section 4.2.2 discusses the bias dependence of the source and drain resistance values in a silicon MESFET. Section 4.2.3 presents simulations for a submicron GaAs MESFET using an energy transport simulator and a Monte Carlo particle simulator.

#### 4.2.1 Source and Drain Resistance Models

The source and drain resistance models are divided into three types according to the definition of the resistance. The first definition is a constant value definition of the source and drain resistance. These models use the I-V characteristics of the transistor to extract bias independent values for  $R_S$  and  $R_D$ . The constant value definition models include the Hower and Bechtel model[34], the Fukui model[35] and the end resistance model [36-39]. The Hower model extracts the sum  $R_S + R_D$  by measuring the drain-source resistance at  $V_{DS} \rightarrow 0$  as a function of the gate voltage. The Fukui method extracts the value of  $R_S - R_D$  by measuring the current flow through the gate to either the source or the drain. This method finds  $R_S - R_D$  as

$$R_S - R_D = \frac{dV_{GS}}{dI_G} \mid_{Drain \ open} - \frac{dV_{GD}}{dI_G} \mid_{Source \ open}. \tag{4.2}$$

The end resistance method drives a current through the gate and source terminals. The voltage at the open drain acts as a probe which gives a voltage which is related to the source resistance as

$$R_S = \frac{V_D}{I_G} - \alpha R_{ch} \tag{4.3}$$

where  $R_{ch}$  is the channel resistance. Similarly, a current is flowed through the gate and drain terminals with source open circuited to give

$$R_D = \frac{V_S}{I_G} - \alpha R_{ch}. \tag{4.4}$$

The  $\alpha$  depends on the bias condition and measurement method as described in the literature [39].

The second definition[41] is the geometric definition where the resistance is defined for the region from the source to the edge of the gate for  $R_S$  and from the drain to the edge of the gate for  $R_D$  as seen in Figure 4.11. The sum of  $R_S + R_D$  is found by measuring the value of  $R_S + R_D + R_{ch}$  for transistors with various channel lengths.  $R_{ch}$  is the active channel resistance under the gate. The sum  $R_S + R_D + R_{ch}$  is then plotted versus channel length and the extrapolation of the data points to  $L_G = 0$  gives  $R_S + R_D$ . This method gives a gate bias dependent model.

The third definition, which is used for this research, is the power dissipation definition of source and drain resistance. For this definition, the resistance is extracted from a device simulator using the simulated potential, electric field, and current data. The source and drain resistance is found by equating the parasitic resistance power loss in a lumped model,  $RI_{term}^2$ , to the power loss throughout the parasitic resistance region. The equation for this parasitic equivalent resistance is given by

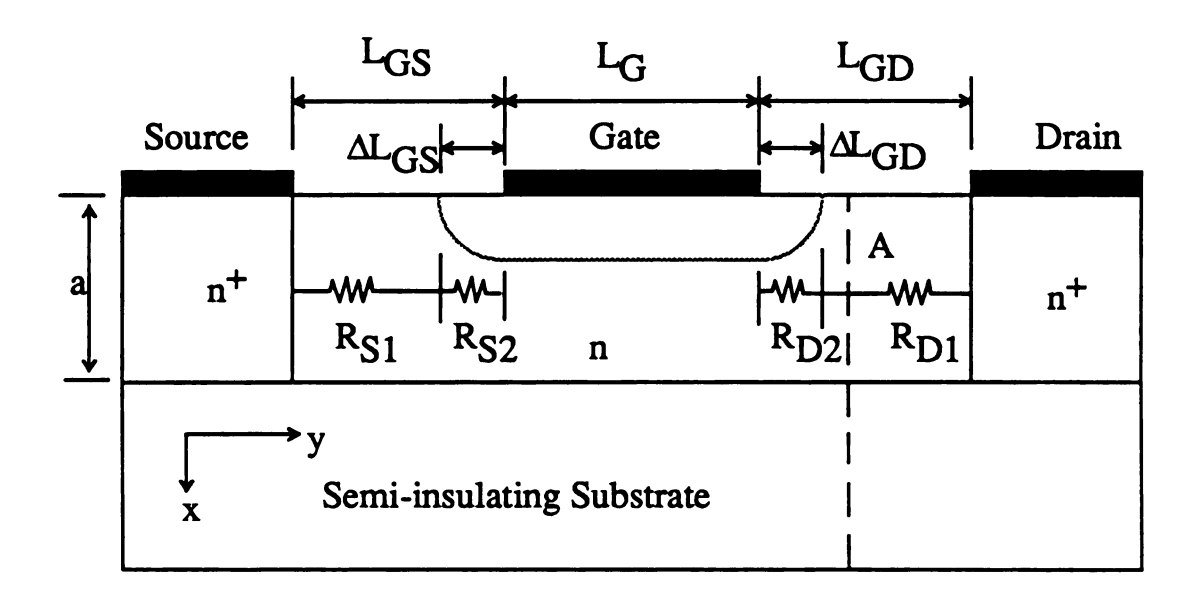


Figure 4.11. MESFET structure showing the lateral gate depletion regions  $\Delta L_{GS}$  and  $\Delta L_{GD}$ . The thickness of the active layer is a.

$$R = \frac{\int_{R} \frac{\mathbf{J} \cdot \mathbf{E} \ dr^3}{I_{term}^2}.$$
 (4.5)

J·E is the power dissipation per unit volume as described by Navon[42] and Adler[43]. By selecting various cross-sectional regions, this method allows the resistivity versus position to be determined. The value of  $R_S$  is found using the power dissipation in the region extending from the source to the edge of the gate. This source resistance is further divided as the resistance from the source to the edge of the lateral gate depletion region,  $R_{S1}$ , and the resistance from the edge of the lateral depletion region to the edge of the gate,  $R_{S2}$ . The edge of the lateral depletion region is selected as the y position in Figure 4.11 where the surface concentration starts to decrease because of the gate depletion effect. Typically, a decrease in the surface concentration to 90% of the non-depleted value is used to indicate the edge of the gate's lateral depletion region. Knowing the value of  $R_{S1}$  is important for understanding how changes in the source-to-gate spacing changes the source resistance.

The drain resistance can also be divided into two sections which extend from the edge of the gate to the edge of the lateral depletion region,  $R_{D2}$ , and from the edge of the lateral depletion region to the drain,  $R_{D1}$ . For small drain voltages with the transistor operating in the linear region both  $R_{D1}$  and  $R_{D2}$  have validity as being part of the parasitic drain resistance. However, when the transistor is operating in the saturation region, the use of  $R_{D2}$  as part of the parasitic drain resistance is not valid as the channel under the lateral depletion region is in a current saturation condition. This region  $R_{D2}$  becomes a part of the effective channel length that accounts for additional carrier transit time delay. Since the  $R_{D2}$  portion of the drain resistance is strongly dependent on the active channel behavior, the  $R_{D2}$  portion of the transistor will be considered as part of the intrinsic transistor device model. The behavior of  $R_{D1}$  will be of primary interest in this research.

These three methods give slightly different  $R_S$  and  $R_D$  values because of the different definitions for the source and drain resistance used in each case. To compare the three definitions, the structure shown in Figure 4.11 has been simulated and the three methods have been used to calculate the source and drain resistance values. The Si MESFET structure simulated has  $L_G = 1.0 \ \mu m$ ,  $L_{GS} = 0.4 \ \mu m$  and  $L_{GD} = 0.6 \ \mu m$ . The active channel doping was  $N_D = 2 \times 10^{17} \ cm^{-3}$  and the channel thickness was  $0.12 \ \mu m$ . The simulator used was the PISCES-II two-dimensional semiconductor device simulator[28] which solves the Poisson equation and the continuity equation.

The Hower and Bechtel method was applied to the simulated current-voltage data to get  $R_S+R_D=2530~\Omega-\mu m$  (resistance for a unit width of 1  $\mu m$ ). The Fukui method gave a value of  $R_D-R_S=695~\Omega-\mu m$ . Putting these two results together gives  $R_S=920~\Omega-\mu m$  and  $R_D=1610~\Omega-\mu m$ . The second method of finding the parasitic resistance is by using transistors with different channel lengths. At a gate voltage of 0.0 volts, this method yielded a value of  $R_D+R_S=3450~\Omega-\mu m$ . This value is greater than the Hower and Bechtel value because the resistance of the lateral depletion regions is included in this second method. The new method proposed in this paper gives values at  $V_{GS}=0.0$  volts and  $V_{DS}=0.01$  (linear region) of  $R_S=R_{S1}+R_{S2}=1452~\Omega-\mu m$  and  $R_D=R_{D1}+R_{D2}=2005~\Omega-\mu m$  for a sum of  $R_S+R_D=3457~\Omega-\mu m$  which agrees closely with the second method. The values of  $R_{S1}=1130~\Omega-\mu m$  and  $R_{D1}=1635~\Omega-\mu m$  gives a sum of  $R_{S1}+R_{D1}=2765~\Omega-\mu m$ . This sum of  $R_{S1}+R_{D1}$  gives a value close to that found using the Hower and Bechtel method and the Fukui method.

## 4.2.2 Bias Dependence of the Source and Drain Resistance

The values of  $R_S$  and  $R_D$  using the power dissipation definition are dependent on the gate voltage,  $V_{GS}$ , and on the drain voltage,  $V_{DS}$ . The gate voltage dependence was investigated by Byun and coworkers[41]. They demonstrated using the geometric

definition that the parasitic resistance decreases as the gate voltage of an n-channel MESFET is increased. This occurs because the width of the lateral gate depletion region decreases as the gate voltage increases. The power dissipation definition of the parasitic resistances shows a similar gate voltage dependence. Using the PISCES-II device simulator, the gate voltage dependence was calculate for the source and drain resistance at  $V_{DS} = 0.01$  volts. The results are shown in Figure 4.12 where the drain and source resistances,  $R_S$  and  $R_D$ , decrease as the gate voltage increases. Also shown in Figure 4.12 are the values of  $R_{S1}$  and  $R_{D1}$ . Both of these resistances show an increase as the gate voltage increases. The increase in the resistance occurs because the lateral gate depletion region decreases in size so that the length of the source and drain resistance regions,  $R_{S1}$  and  $R_{D1}$ , increase. For a gate voltage of -0.9 volts the lateral depletion width was 0.088  $\mu m$  and for a gate voltage of 0.3 volts the lateral depletion width was 0.052  $\mu m$ . The use of this variable length resistor model for  $R_{S1}$  and  $R_{D1}$  is appropriate when the gate's lateral depletion width is modeled in the active device portion of the MESFET model.

The drain voltage dependence of the source and drain resistance can also be determined with the device simulator extraction of the parasitic resistors. The drain voltage influences both the drain and the source resistances. Considering the source resistance first, the source resistance changes as a function of the drain bias if the electric field in the source resistance region is large enough that the carrier mobility begins to decrease. The carrier mobility decrease occurs in silicon due to carrier velocity saturation. The lateral depletion width on the source end of the gate remains unchanged with respect to the drain voltage. The source resistance values versus drain voltage for a silicon MESFET with  $L_{GS} = 0.4 \, \mu m$ ,  $L_{G} = 0.5 \, \mu m$  and  $L_{GD} = 0.6 \, \mu m$  are shown in Figure 4.13. The mobility versus electric field expression used to give the mobility in the simulation [28] was

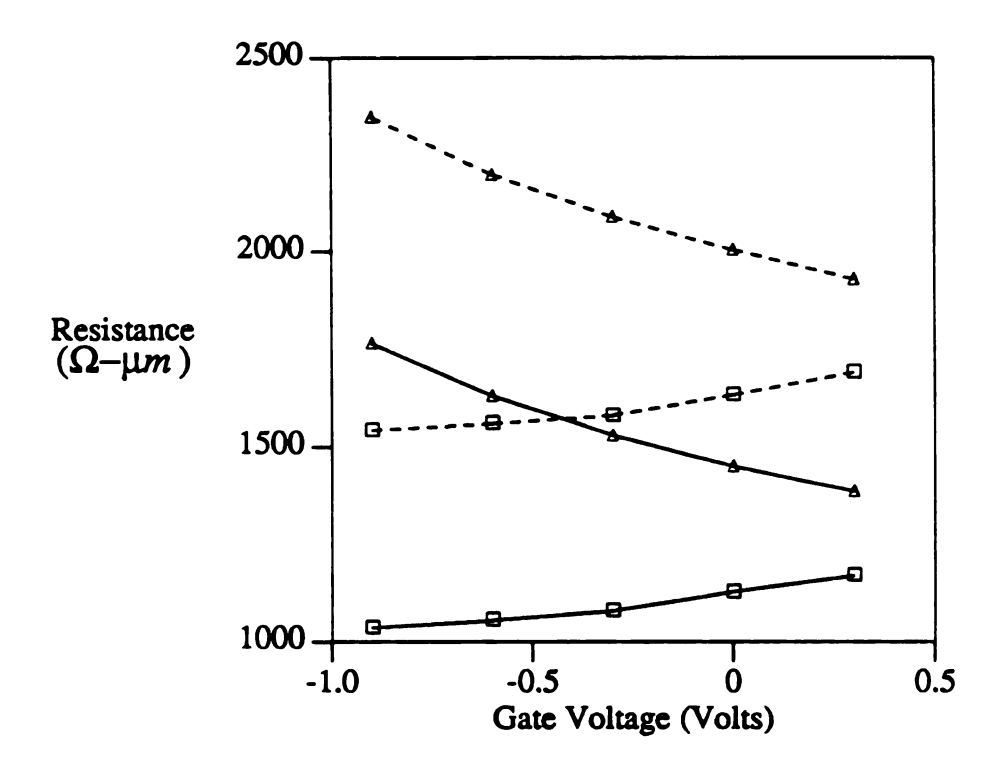


Figure 4.12. Source (solid-line) and drain (dashed line) resistance versus gate voltage for a silicon MESFET using the power dissipation definition. The triangles indicate the resistances calculated using the gate edge definition and the squares indicate the resistances calculated using the gate depletion edge definition.

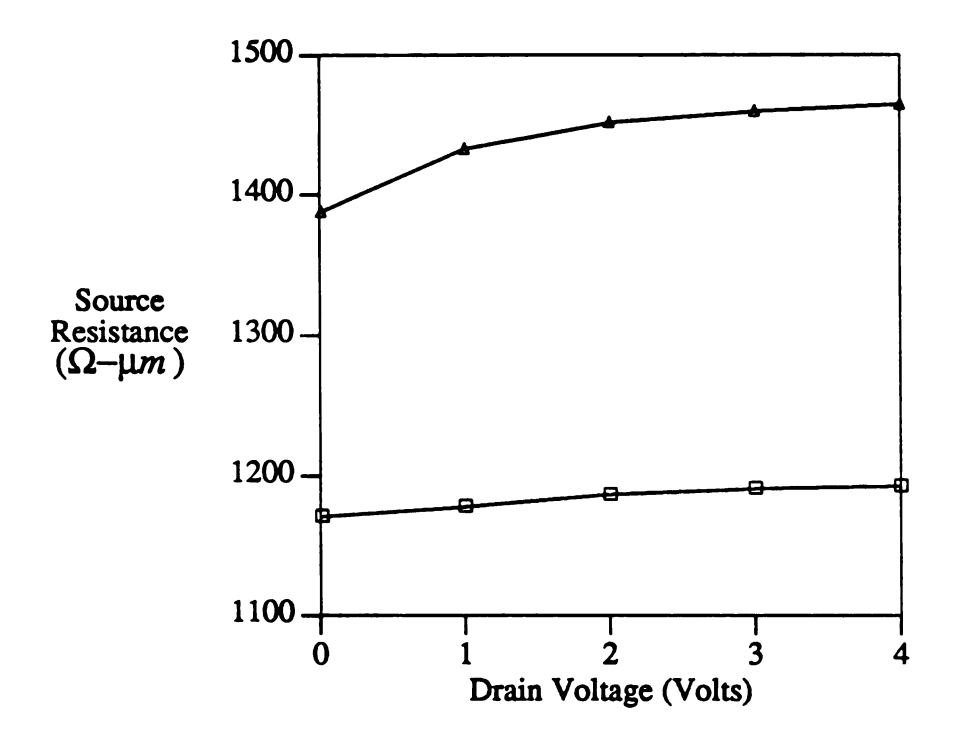


Figure 4.13. Source resistance versus drain voltage with a gate voltage of 0.3 volts. The triangles indicate the resistance calculated using the gate edge definition and the squares indicate the resistances calculated using the gate depletion edge definition. The barrier potential height for the gate was 0.7 volts.

$$\mu(E) = \left[\frac{1}{1 + (\mu_o E / v_{sat})^2}\right]^{1/2} \mu_o \tag{4.6}$$

where E is the local electric field,  $\mu_o$  is the zero field mobility and  $\nu_{sat}$  is the saturation velocity.

The drain resistance,  $R_{D1}$ , is influenced by both the change in the lateral depletion width of the gate and by the decrease in the mobility at high electric fields. The change in the lateral depletion width versus drain voltage is plotted in Figure 4.14 where the width is seen to change by 0.135  $\mu m$  for  $V_{DS}$  changing from 0.0 to 4.0 volts. The influence of the non-constant mobility as seen in Figure 4.15 is assessed by plotting the value of the resistance from cross-section A (as shown in Figure 4.11) to the drain contact using the resistance definition given in equation (4.5). This plot is constructed using cross-section A so that the lateral depletion change is absent from the resistance calculation. The effect occurring is that the drain region resistivity increases as the drain voltage increases. In opposition, the lateral gate depletion region increases in size as the drain voltage increases. The two effects are opposing each other with one increasing and one decreasing the drain resistance value  $R_{D1}$ . The inclusion of both effects is seen in Figure 4.16 where the drain resistance first decreases slightly then increases.

### 4.2.3 Source and Drain Resistance in Submicron GaAs MESFETs

The power dissipation / electron heating definition of source and drain resistance is applied to short channel GaAs MESFETs in this section. The structure used for the simulation had  $L_{GS}=0.4~\mu m$ ,  $L_{G}=0.4~\mu m$  and  $L_{GD}=0.6~\mu m$ . The device doping was a constant n-type doping of  $2.0\times10^{17}~cm^{-3}$  for the active layer. The depth of the active layer was 0.1 micrometers.

One device simulator used was a two-dimensional simulator which selfconsistently solves the Boltzmann transport equation and the Poisson equation. The

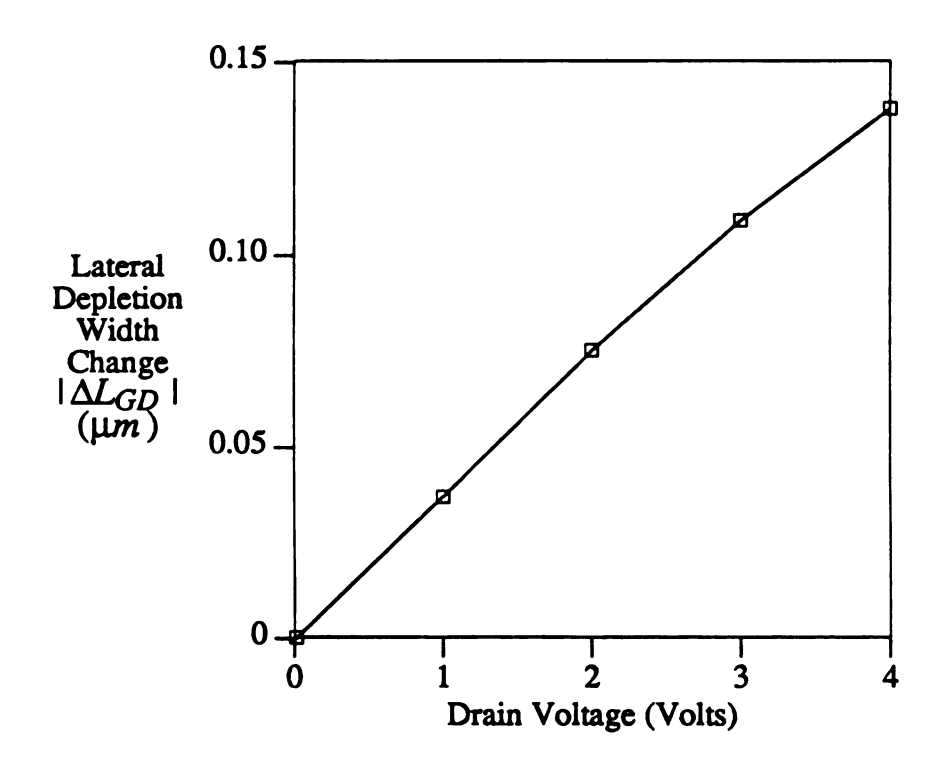


Figure 4.14. Change in the lateral depletion width  $\Delta L_{GD}$  versus drain voltage.

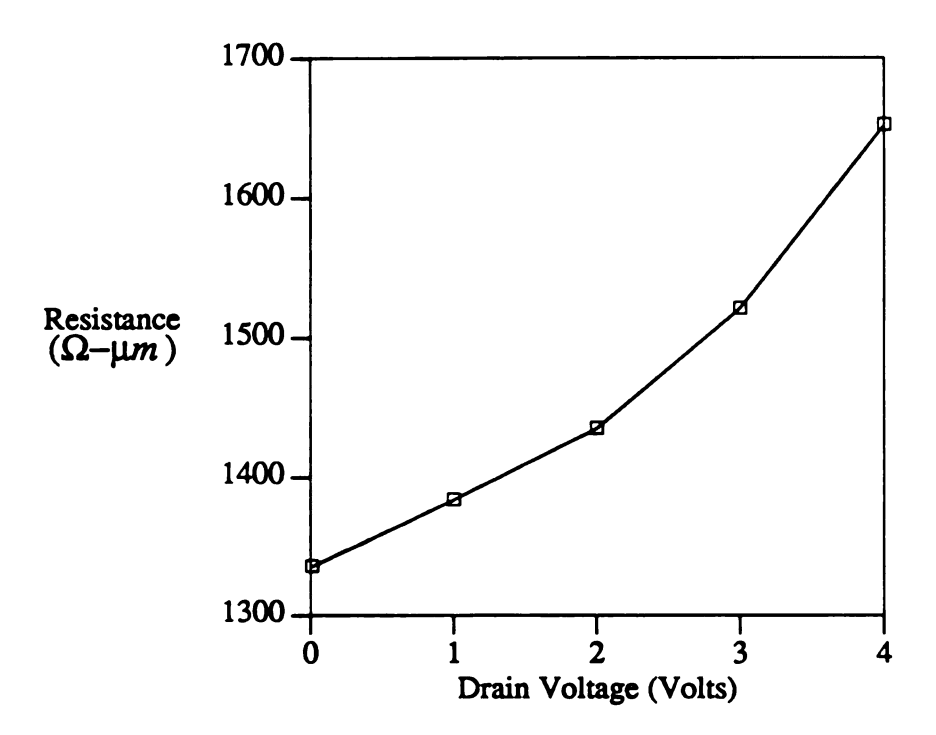


Figure 4.15. Drain resistance between cross section A (shown in Figure 4.11) and the drain contact versus drain voltage.

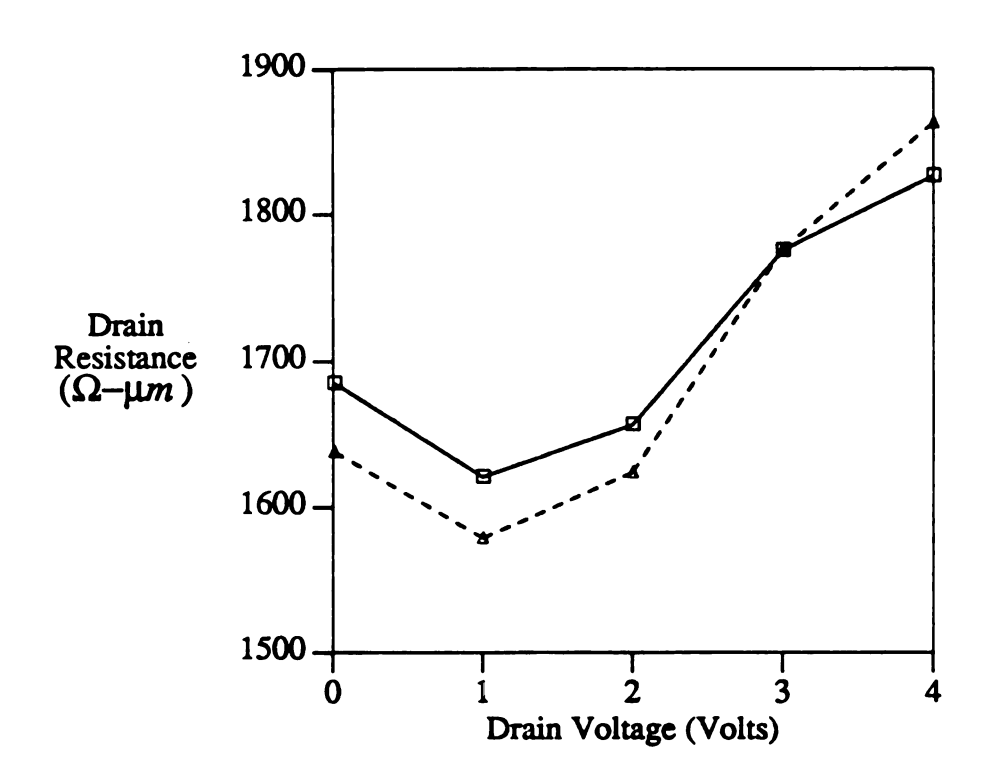


Figure 4.16. Drain resistance versus drain voltage for a silicon MESFET. The dashed line is for  $V_{GS}=0.0$  volts and the solid line is for  $V_{GS}=0.3$  volts.

Boltzmann transport equation is solved using the Monte Carlo particle method and the Poisson equation is solved using the finite difference method[4,44,61]. The simulator includes the nonparabolicity of the  $\Gamma$ , L and X valleys, ionized impurity scattering, intervalley scattering, acoustic phonon scattering and optical phonon scattering. The simulator calculates the solution of the Poisson equation every 5 femtoseconds and the Monte Carlo method moves the particles for the 5 femtoseconds of electron movement. This process is repeated with an advancing time until an accurate steady-state solution is reached. This simulator was used so that the non-stationary velocity overshoot and the multivalley transport effects of GaAs would be included in the resistance calculation.

Another simulator used was a two-dimensional energy transport simulator which solves the Poisson equation, the continuity equation and the energy transport equation [15,16]. The multi-valley nature of GaAs was treated using a single continuity equation and a single transport equation to represent all the valleys. This was done by using an energy dependent effective mass, momentum relaxation time and energy relaxation time. The energy dependence of these values were extracted from a one-particle Monte Carlo simulator [45-47].

The source and drain resistance behavior versus gate voltage for small drain voltages was found to have a behavior for the GaAs MESFET similar to the Si MESFET as discussed in Section 4.2.2. The source and drain resistance variation was due to the change in the lateral gate depletion width with respect to the gate voltage.

The drain resistance at moderate and large drain voltages requires further examination because of non-stationary effects. In the energy transport solution, the steady-state energy transport equation given by[7]

$$\mathbf{J} \cdot \mathbf{E} + \nabla \cdot \alpha [\mu W \mathbf{E} + \nabla (DW)] - \frac{W - W_o}{\tau_{\xi}(\xi)} = 0$$
 (4.7)

is used. W is the energy density,  $W_o$  is the equilibrium energy density, D is the diffusion coefficient,  $\mu$  is the electron mobility,  $\alpha$  is the energy transport coefficient,  $\tau_{\xi}$  is the energy relaxation time and  $\xi$  is the average electron energy. The first term is the energy gained by the electrons from the electric field, the second term is the transport of the energy and the third term is the dissipation of the electron energy to the lattice. The drift diffusion model used earlier for the silicon simulations assumes that the energy is dissipated in the same region as the electrons gain energy from the electric field. The MESFET operating with a moderate drain voltage has a large transport of energy from the active channel region into the drain region. The total power dissipated in the drain region can be attributed to the energy transported to the region and the energy dissipated in the region which was created by the J-E electron heating in the region. The total power dissipation is written as

$$P_{tot} = P_{et} + P_{eh} \tag{4.8}$$

where  $P_{et}$  is the power dissipation in the drain region due to energy transported from the active channel region and  $P_{eh}$  is power dissipated in the drain resistance region due to electron heating in the drain resistance region. An assumption is made that the drain contract regions are ohmic contacts with an equilibrium electron density and an equilibrium electron energy density. The design of the drain resistance region should look at minimizing the value of  $P_{eh}$ .

The calculation of the total power dissipation in this region for the energy transport simulator is done using

$$P_{tot} = \int_{R_{D1}} \frac{W - W_o}{\tau_{\xi}(\xi)} dr^3. \tag{4.9}$$

The calculation of the electron heating in this region is given by

$$P_{eh} = \int_{R_{0.1}} \mathbf{J} \cdot \mathbf{E} \ dr^3. \tag{4.10}$$

The method for calculating the total power dissipation in the resistance region using the Monte Carlo simulator is to calculate the net phonon emission in this region per unit time. The total power dissipation is given by

$$P_{tot} = \sum_{ph} \frac{E_{ph} [n_{ph}^e - n_{ph}^a]}{t}$$
 (4.11)

where  $E_{ph}$  is the phonon energy,  $n_{ph}^{e}$  is the number of phonons emitted,  $n_{ph}^{a}$  is the number of phonons absorbed and t is the simulated time. The summation is performed over the phonons of different energies produced by the various scattering mechanisms.

The drain resistance  $R_{D1}$  is best understood by considering the power dissipation and the electron heating. Figure 4.17 plots both of these quantities for drain voltages from 0.1 to 2.0 volts. The main feature to note is that because energy is transported from the channel region to the drain resistance region, the power dissipation is greater than the electron heating in the drain resistance region. The smaller value for electron heating is due to the electrons moving across the drain resistance region as the result of a gradient in the electron energy or temperature. The influence of the energy or temperature gradient is demonstrated by considering the velocity expression for electrons as given by [7]

$$\mathbf{v} = -\left[\mu(\xi)\mathbf{E} + \frac{k\mu(\xi)}{q}\nabla T + \frac{kT\mu(\xi)}{qn}\nabla n\right]$$
(2.33)

where  $\xi$  is the electron energy, T is the electron temperature,  $\mu$  is the mobility, and n is the electron concentration. The first term is the drift transport term, the second term is the temperature gradient transport term, and the last term is the diffusion transport term. Figure 4.18 demonstrates this large carrier temperature gradient between the gate and the drain. The drain resistances calculated using  $R_{D \, 1(tot)} = P_{tot}/I_D^2$  and  $R_{D \, 1(eh)} = P_{eh}/I_D^2$  are shown in Figure 4.19. The drain resistance due to electron heating shows a slight decrease initially as the drain voltage increases because of the

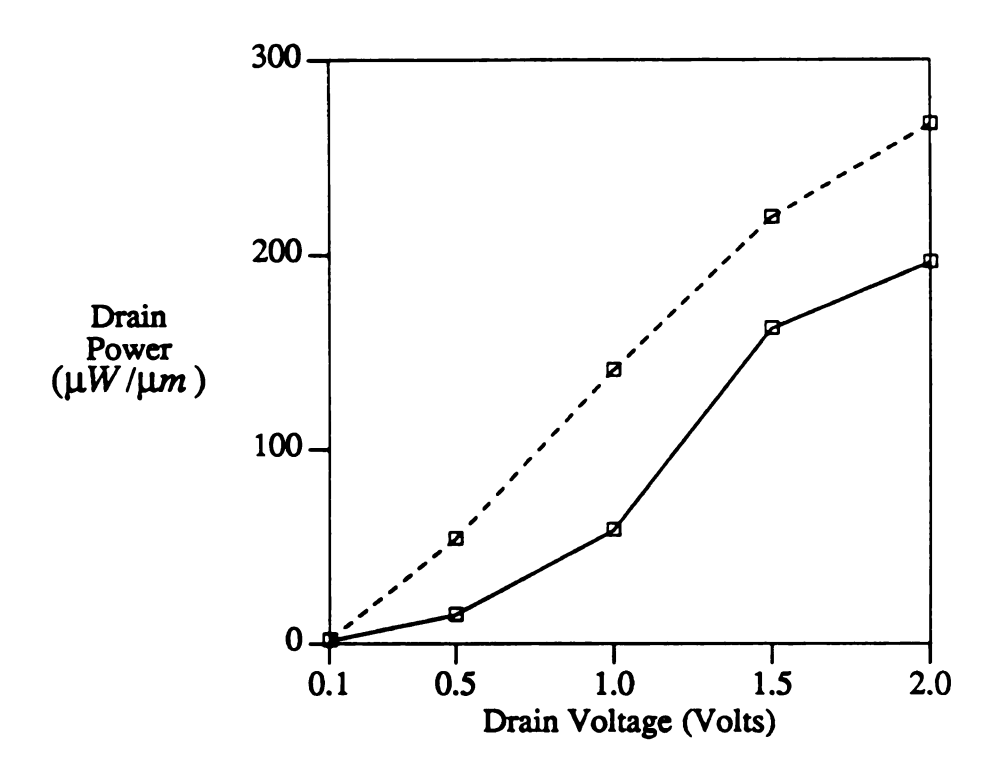


Figure 4.17. Power dissipation (dashed line) and electron heating (solid line) in the drain resistance region  $R_{D\,1}$  versus drain voltage for a  $L_G=0.4~\mu m$  GaAs MESFET.

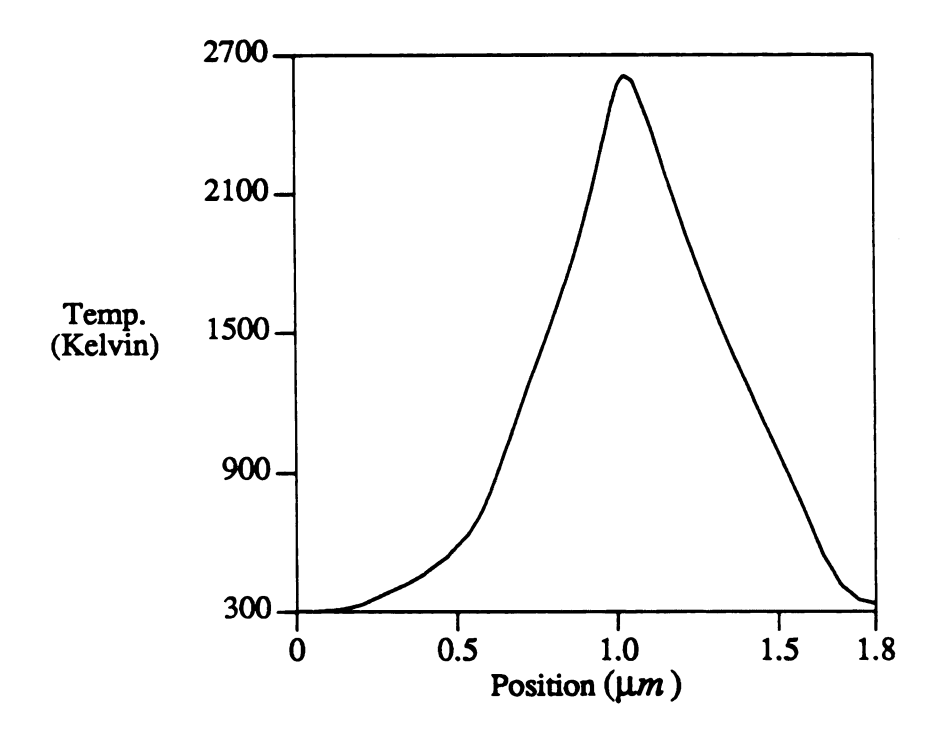


Figure 4.18. Electron temperature versus position between the source and the drain as calculated using the energy transport simulator. The values are plotted at a depth of 0.08  $\mu m$ . The gate extends from 0.6  $\mu m$  to 1.0  $\mu m$ . The drain voltage was 1.0 volts and the gate voltage was 0.3 volts.

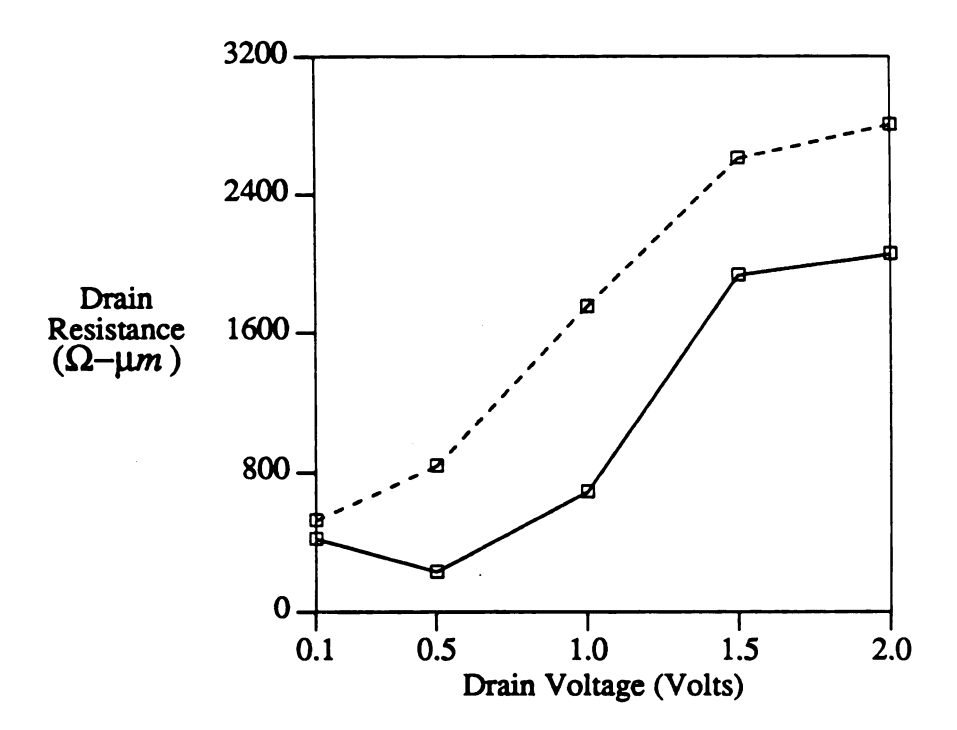


Figure 4.19. Equivalent drain resistance versus drain voltage for a  $L_G = 0.4 \,\mu m$  GaAs MESFET. The resistance values for the dashed curve are calculated using the total power dissipation in the drain resistance region. The resistance values for the solid curve are calculated using the electron heating in the drain resistance region.

movement of the lateral gate depletion region. However, for larger drain voltages the electron heating resistance increases because the electric field increases resulting in a reduced mobility. The  $R_{D1(tot)}$  resistance which includes both the electron heating energy and the transported energy increases monotonically with the drain voltage.

The two-dimensional Monte Carlo particle simulator provides a more detailed description of the drain resistance region since a multivalley band structure is included. The electrons are moving from the source to the drain at moderate or high drain voltages scattering into the L and X valleys. When these electrons enter the drain resistance region the potential energy associated with being in a higher valley must be dissipated. The dissipation of the energy can be observed in Figure 4.20 where the total energy of the electrons above the  $\Gamma$  valley minimum and the kinetic energy of the electrons are both plotted versus position between the source and the drain. This plot shows the loss of the higher valley potential energy as the electrons move across the drain resistance region.

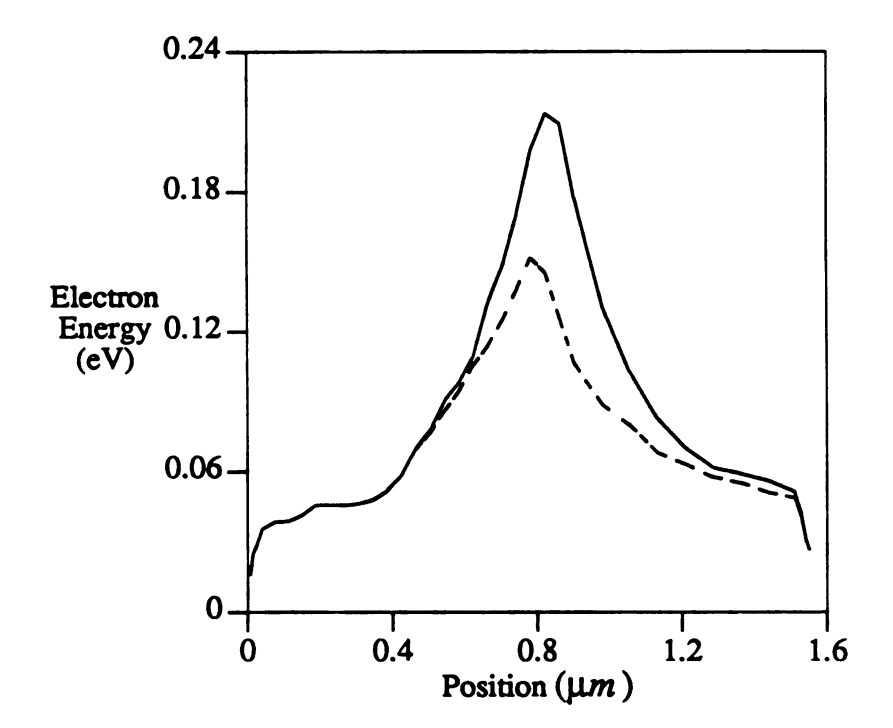


Figure 4.20. Total electron energy above the  $\Gamma$  valley minimum (solid line) and the electron kinetic energy (dashed line) versus position between the source and drain at a depth of 0.08  $\mu m$ . The gate extended from 0.5  $\mu m$  to 0.9  $\mu m$ . The drain voltage was 0.5 volts and the gate voltage was 0.3 volts. Calculations were done using a Monte Carlo particle simulator.

#### CHAPTER 5

## AC SIMULATION OF MESFETS USING THE SEMICONDUCTOR HYDRODYNAMIC TRANSPORT EQUATIONS

## 5.1 AC Simulation Methods

Simulation programs providing DC and transient solutions to the hydrodynamic transport equations in two dimensions can be found in the literature[7,9]. The third device operating mode, namely small-signal AC operation, has received less attention to date in the context of numerical device simulation. This is due partly to the need to have an existing DC device solution upon which to build the small-signal AC analysis and partly to the nature of the AC computation. This can be understood by knowing that HTM is much more complex than DDM, even for the DC solution. Additionally, the HTM becomes more complex for compound semiconductor devices. This chapter will develop an AC model using the HTM for the GaAs MESFET.

The techniques for AC analysis of semiconductor devices using the DDM can be found in the work of Laux[48]. Three standard approaches are Fourier Decomposition (FD), Incremental Charge Partition (CP), and Sinusoidal Steady-State Analysis ( $S^3A$ ). This section will briefly review the first two methods, the third method will be discussed in the next section.

## (i) Fourier Decomposition of Transient Excitations (FD)

The FD method applies a step perturbation  $\Delta V_j$  to terminal j about a DC operating point as shown in Figure 5.1. The FD method gives the small-signal admittance matrix component  $\tilde{Y}_{ij}(\omega)$  as

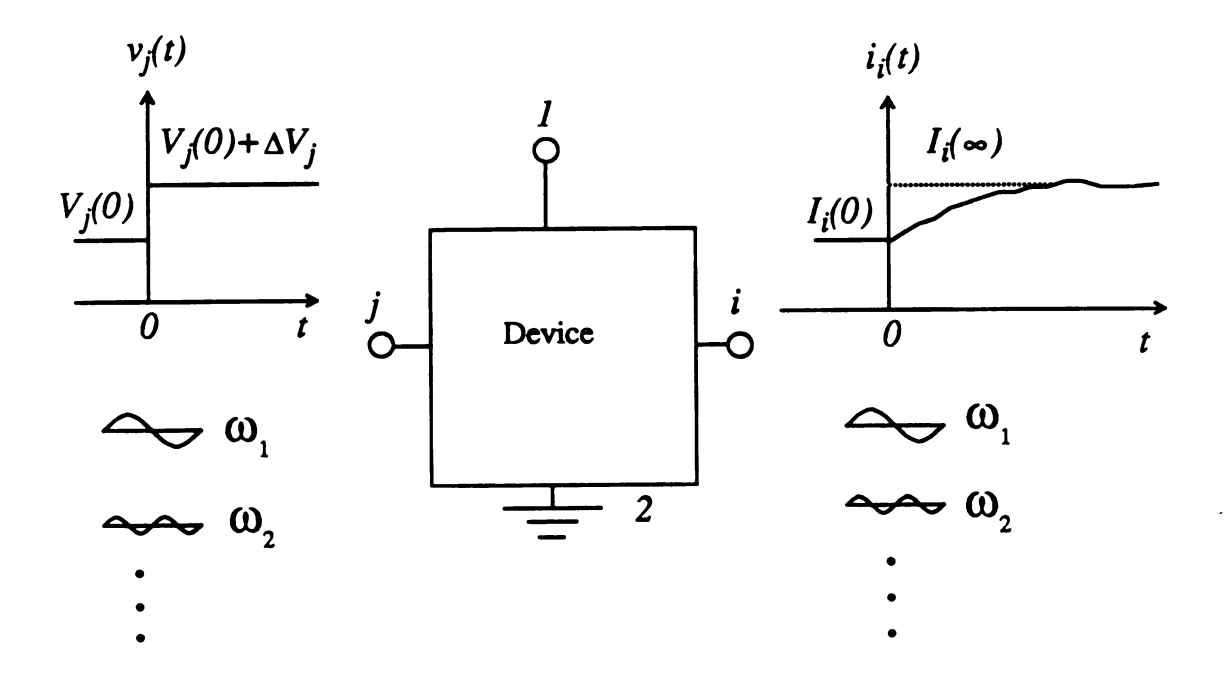


Figure 5.1. Fourier decomposition method.

$$\tilde{Y}_{ij}(\omega) = \frac{\mathbf{F}\left\{i_i(t) - I_i(0)\right\}}{\mathbf{F}\left\{v_j(t) - V_j(0)\right\}}$$

$$= \frac{I_i(\infty) - I_i(0)}{\Delta V_j} + \frac{j\omega}{\Delta V_j} \mathbf{F} \left\{ i_i(t) - I_i(\infty) \right\}$$
 (5.1)

where **F** is Fourier transform operator,  $I_i(0)$  is the steady-state current,  $V_j(0)$  is the steady-state voltage,  $v_j(t) = V_j(0) + \Delta V_j u(t)$ , and  $i_i(t)$  is the transient response at terminal i. Upon separating (5.1) into real and imaginary parts, the conductance and capacitance matrix entries become

$$G_{ij} = \left\{ \frac{I_i(\infty) - I_i(0)}{\Delta V_j} + \frac{\omega}{\Delta V_j} \int_0^{\infty} \left[ i_i(t) - I_i(\infty) \right] \sin \omega t dt \right\}$$
(5.2)

and

$$C_{ij} = \left\{ \frac{1}{\Delta V_j} \int_0^{\infty} \left[ i_i(t) - I_i(\infty) \right] \cos \omega t dt \right\}.$$
 (5.3)

The FD method needs DC and transient device simulation capabilities. It requires that limitations be placed on the step  $\Delta t$  used in the transient solution in order to reduce the error for high frequency admittance, and it requires that upper and lower limitations be placed on the exciting voltage  $\Delta V_j$  in order to avoid harmonic generation and to dominate numerical noise, respectively.

#### (ii) Incremental Charge Partitioning (CP)

Figure 5.2 shows the incremental charge partitioning method. The CP method finds the capacitance and conductance matrix components as

$$G_{ij} = \frac{\Delta I_i}{\Delta V_j}, V_k = const., k \neq j$$
 (5.4)

and

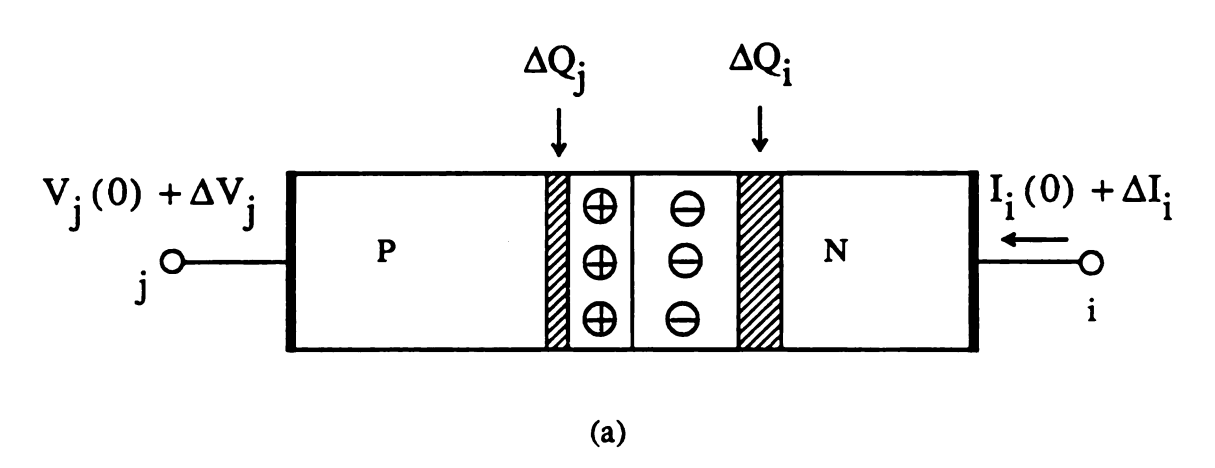
$$C_{ij} = \frac{\Delta Q_i}{\Delta V_j}, V_k = const., k \neq j$$
 (5.5)

where  $\Delta Q_i$  is the incremental charge associated with terminal i,  $\Delta I_i$  is the incremental current at terminal i, and  $\Delta V_j$  is the incremental voltage applied at terminal j. The CP method requires a DC solution only. The total charge Q is calculated by integrating electron density n over the P-region or N-region for a diode, or over the whole simulated region for a MESFET. The  $\Delta Q$  is obtained by subtracting two Q's found from two-successive  $V_{GS}$  biases. The CP method provides only quasi-static (low frequency) admittance. A disadvantage of this method is that the CP method depends on insight into the physics of device operation in order to partition the incremental charge to each contact. For an N-terminal device such physical insight is rarely available.

# 5.2 Sinusoidal Steady-State Analysis ( $S^3A$ ) using Hydrodynamic Transport Model

#### 5.2.1 Model Development

The third technique for the AC analysis of semiconductor devices is the Sinusoidal Steady-State Analysis ( $S^3A$ ) method. The  $S^3A$  method works directly in the frequency domain, and it requires DC and AC device simulation capabilities. The admittance matrix obtained for the  $S^3A$  method is rigorously correct as was the case for the FD method. However, two characteristics of the  $S^3A$  make the technique extremely accurate: (1) no time steps need be selected using the  $S^3A$  and hence no



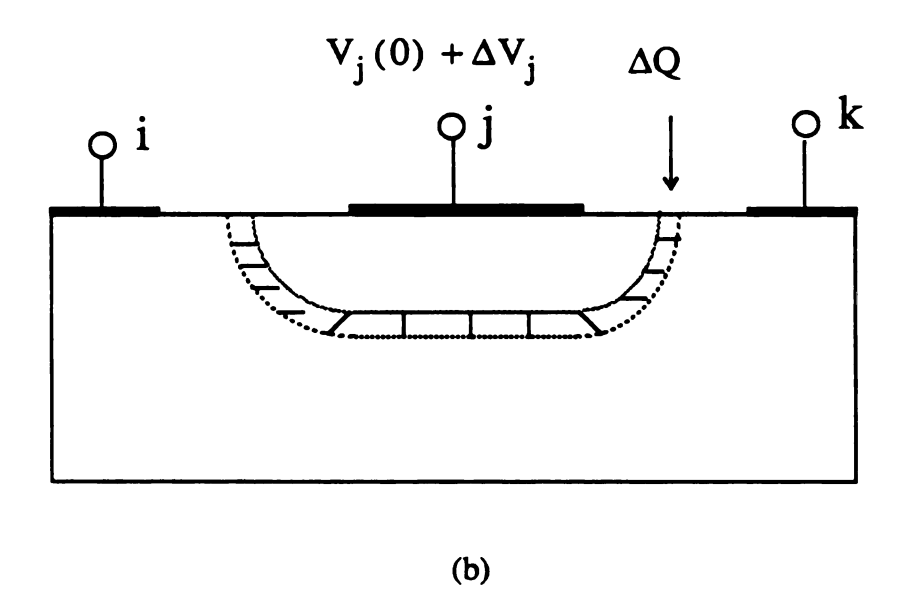


Figure 5.2. Charge partitioning method for (a) a two terminal device, and (b) a three terminal device.

inaccuracies related to time discretization occur, and (2) the device is linearized about the DC operating point so that harmonic generation within the device is precluded.

The  $S^3A$  method is performed after a DC solution has been achieved. Starting from a DC bias condition, an input of given amplitude and frequency can be applied to a device structure from which sinusoidal terminal currents are calculated. Then using the relationship

$$\tilde{Y}_{ij} = G_{ij} + j\omega C_{ij} = \frac{\tilde{I}_i}{\tilde{V}_j}, \, \tilde{V}_k = 0, \, k \neq j$$
(5.6)

the frequency dependent admittance matrix, and hence conductances and capacitances, can be calculated. Note also that by varying the frequency and examining the various device admittances, the current, voltage and power gains versus frequency can be directly determined.

Special numerical techniques are often adopted for the  $S^3A$  method. The Poisson equation, electron continuity equation, and energy conservation equation are expressed as [see Section 3.6.2]

$$F_{\psi}(\psi, n, \xi) = 0$$

$$F_{n}(\psi, n, \xi) + \frac{\partial n}{\partial t} \overline{dx} \overline{dy} = 0$$

$$F_{\xi}(\psi, n, \xi) + \frac{\partial n \xi}{\partial t} \overline{dx} \overline{dy} = 0$$
(5.7)

where  $\overline{dx} \ \overline{dy}$  exists due to the integrated form for  $F_{\psi}$ ,  $F_n$ , and  $F_{\xi}$ .

The AC system is obtained by substituting time dependent functions of the form  $\zeta(t) = \zeta_0 + \zeta e^{j \omega t}$  into (5.7), where  $\zeta = \psi$ , n, or  $\xi$ , and the 0 subscript denotes a steady-state solution for the device. Performing a Taylor's series expansion on (5.7), and keeping only the linear terms, we have

$$(F_{\psi})_{dc} + \left[\frac{\partial F_{\psi}}{\partial \zeta}\right]_{dc} \zeta = 0$$

$$(F_n)_{dc} + \left[\frac{\partial F_n}{\partial \zeta}\right]_{dc} \zeta + j \omega \overline{dx} \, \overline{dy} \, \tilde{n} = 0$$

$$(F_{\xi})_{dc} + \left[\frac{\partial F_{\xi}}{\partial \zeta}\right]_{dc} \zeta + j \omega \overline{dx} \, \overline{dy} (n_0 \xi + \xi_0 \tilde{n}) = 0$$
(5.7b)

where  $(F_{\psi})_{dc}$ ,  $(F_n)_{dc}$  and  $(F_{\xi})_{dc}$  are expressions for the DC solution and therefore should be zero when the DC solution has been reached. Hence, the AC solution becomes

$$\left[\frac{\partial F_{\psi}}{\partial \zeta}\right]_{dc} \ddot{\zeta} = 0$$

$$\left[\frac{\partial F_{n}}{\partial \zeta}\right]_{dc} \ddot{\zeta} + j \omega dx dy \tilde{n} = 0$$

and

$$\left(\frac{\partial F_{\xi}}{\partial \zeta}\right)_{dc} \zeta + j \omega \overline{dx} \, \overline{dy} (n_0 \xi + \xi_0 \tilde{n}) = 0.$$
 (5.7c)

For numerical implementation, the AC system (5.7c) at point i becomes

$$\sum_{j=1}^{N} \begin{bmatrix} \frac{\partial F_{\psi i}}{\partial \psi_{j}} & \frac{\partial F_{\psi i}}{\partial n_{j}} & \frac{\partial F_{\psi i}}{\partial \xi_{j}} \\ \frac{\partial F_{n i}}{\partial \psi_{j}} & \frac{\partial F_{n i}}{\partial n_{j}} + j \omega d\overline{x} d\overline{y} & \frac{\partial F_{n i}}{\partial \xi_{j}} \\ \frac{\partial F_{\xi j}}{\partial \psi_{j}} & \frac{\partial F_{\xi j}}{\partial n_{j}} + j \omega \xi_{0} d\overline{x} d\overline{y} & \frac{\partial F_{\xi j}}{\partial \xi_{j}} + j \omega n_{0} d\overline{x} d\overline{y} \end{bmatrix}_{dc} \begin{bmatrix} \tilde{\psi}_{j} \\ \tilde{n}_{j} \\ \tilde{\xi}_{j} \end{bmatrix} = 0$$
 (5.8)

where  $F_{\psi i}$  denotes the DC portion of the Poisson equation solution in integrated form at point i, similar interpretations hold for  $F_{ni}$  and  $F_{\psi i}$ . In particular, all the terms without any  $\omega$  frequency dependence form the Jacobian matrix which is available from the DC solution done to get the operating point.

After assembling the global AC matrix, the AC system becomes

$$[J+jD]\tilde{X}=B \tag{5.10}$$

where J is the Jacobian matrix, D contains the contributions of the time derivative terms in (5.7) to the matrix, B is a real vector dependent on AC driving voltages and  $\tilde{X}$  is the AC solution vector given by  $\tilde{X}_j = [\tilde{\psi}_j, \tilde{n}_j, \tilde{\xi}_j]^T$ .

For the evaluation of (5.10), recall that the arrangement of unknown variables in the DC case discussed in Section 3.6.2 gives the matrix J a size of  $(6ny+5)\times 3N$ . D in (5.10) contains two non-zero diagonal bands, hence the reduced size of D is  $2\times 3N$ . Usually D is very small compared to that of J.

Equation (5.10) is a complex matrix equation. By splitting the AC solution vector  $\tilde{X}$  into real and imaginary parts  $X_R + jX_I$ , (5.10) can be written using only real arithmetic as

$$\begin{bmatrix} J-D \\ D \end{bmatrix} \begin{bmatrix} X_R \\ X_I \end{bmatrix} = \begin{bmatrix} B \\ 0 \end{bmatrix}. \tag{5.11}$$

The system order doubles compared to the DC case. Computation time for the direct factorization of the AC system can be excessive, but the computation time can be reduced by using a block-SOR indirect solution techniques. The block-SOR ( successive-over-relaxation ) solution procedure alternates between the following two equations until convergence is obtained:

$$X_R^{k+1} = (1 - \omega_R) X_R^k + \omega_R J^{-1} (DX_I^k + B)$$
 (5.12a)

$$X_I^{k+1} = (1 - \omega_R)X_I^k + \omega_R J^{-1}(-DX_R^{k+1})$$
 (5.12b)

where the superscript k denotes iteration number and  $\omega_R$  is the SOR parameter. Laux [48] set  $\omega_R < 1$  when using  $f \ge f_T / 10$  for the DDM.

## 5.2.2 Boundary Conditions

The AC boundary conditions are based on the boundary conditions use for the DC solution. The AC boundary used are as follows:

- (i) Neumann boundary conditions are applied to all free surfaces. This AC boundary condition carries over directly from the DC simulation, hence this boundary condition has been already set in the Jacobian matrix J.
- (ii) Dirichlet boundary conditions are applied to the source and drain contacts,

$$\tilde{\Psi} = \tilde{V}_{ss}$$
,  $\tilde{n}_s = \tilde{n}_d = 0$ , and  $\tilde{\xi} = 0$  (5.13)

where  $\tilde{V}_{ss}$  is the small signal directly applied at the contact.  $\tilde{n}_s$  and  $\tilde{n}_d$  are respectively the small signal carrier concentrations at the source and the drain.

(iii) The Schottky contact at the gate is described by the boundary condition

$$\tilde{\Psi} = 0$$
 and  $\tilde{\xi} = 0$ . (5.14)

Here, because a thermionic emission diffusion model is used to calculate the electron concentration at the Schottky contact, the AC electron concentration at the gate carries over directly from the DC simulation.

#### 5.2.3 Small Signal Current Calculation

After solving equations (5.12a) and (5.12b), the small signal current can be calculated by using the small signal variables at each node. For a given branch between nodes i and i+1 as shown in Figure 5.3, the current density is expressed in terms of conduction current and displaced current as

$$\tilde{J} = \tilde{J}_{cond} + \tilde{J}_{disp} \tag{5.15}$$

where

$$\tilde{J}_{cond} = \sum_{i} \frac{\partial J}{\partial \zeta_{i}} \xi_{i}, \quad \zeta_{i} = \psi_{i}, \psi_{i+1}, n_{i}, n_{i+1}, \xi_{i} \text{ and } \xi_{i+1}$$
(5.16)

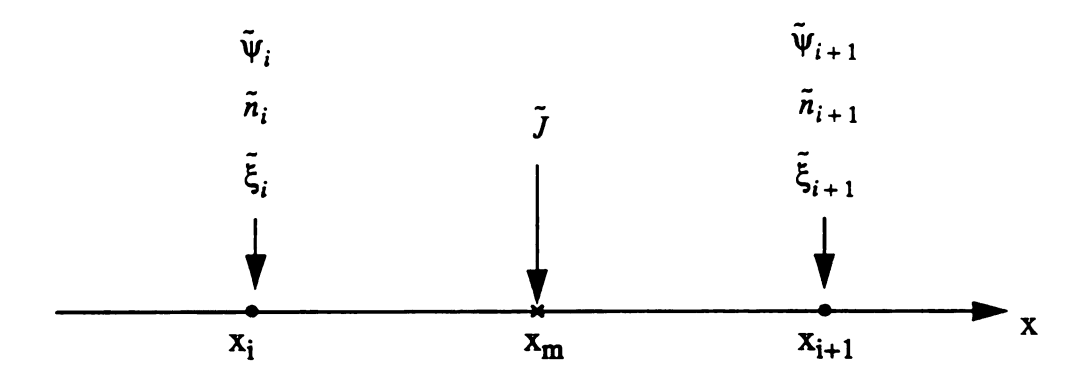


Figure 5.3 Notation for small-signal current density calculation.

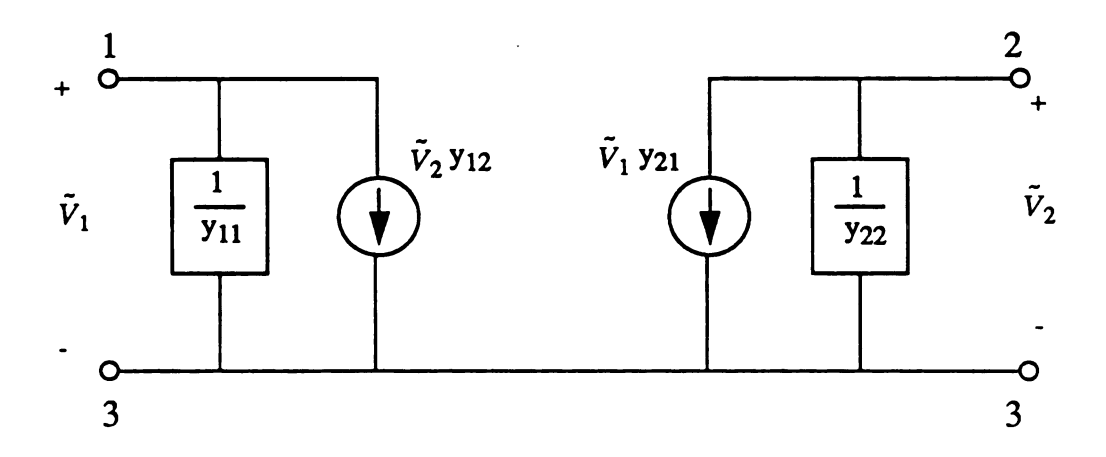


Figure 5.4. The three-terminal y-parameter equivalent circuit.

and

$$\tilde{J}_{disp} = j \omega \varepsilon \tilde{E} = j \omega \varepsilon \left[ \frac{\tilde{\psi}_i - \tilde{\psi}_{i+1}}{h} \right] \\
= -\left[ \omega \varepsilon \frac{(\tilde{\psi}_i - \tilde{\psi}_{i+1})_{imag}}{h} \right] + j \left[ \omega \varepsilon \frac{(\tilde{\psi}_i - \tilde{\psi}_{i+1})_{real}}{h} \right]$$
(5.17)

where h is the spacing between nodes i and i+1.

## 5.2.4 Y-parameter Calculation

The frequency dependent admittance matrix Y can be calculated as

$$\tilde{Y}_{ij} = \frac{\tilde{I}_i}{\tilde{V}_j}, \, \tilde{V}_k = 0, \, k \neq j . \tag{5.6}$$

Applying a small signal at one terminal, and only one, will provide the frequency dependence of *one* column in the Y matrix. For an N-terminal device, N-1 small signal excitations are required to determine the Y matrix at a given DC bias point. For example, two excitations is needed for a three terminal device. For this three terminal device, the first step is to apply a small signal perturbation at terminal 1 to get  $y_{11}$ , and  $y_{21}$ . The second step is to apply a signal at terminal 2 to get  $y_{12}$  and  $y_{22}$ . The y-parameter equations can be expressed as

$$\begin{bmatrix} \tilde{I}_1 \\ \tilde{I}_2 \end{bmatrix} = \begin{bmatrix} y_{11} \ y_{12} \\ y_{21} \ y_{22} \end{bmatrix} \begin{bmatrix} \tilde{V}_1 \\ \tilde{V}_2 \end{bmatrix} .$$
 (5.18)

The equivalent circuit is shown in Figure 5.4. Once the Y parameters have been found, other equivalent parameters, e.g., hybrid parameters: H, scattering parameters: S, impedance parameters: Z, etc., can be calculated using existing parameter transformation tables[49].

## 5.3 HTM Y-parameters Compared with Monte Carlo and Drift Diffusion Models

The structure used for the Y-parameter simulations had  $L_{GS}$ =0.6 $\mu m$ ,  $L_G = 0.4 \mu m$ , and  $L_{GD} = 0.6 \mu m$  [See Figure 4.1]. The device doping was a constant n-type doping of  $5.0 \times 10^{16} cm^{-3}$  for the active layer. The depth of the active layer was  $0.22 \mu m$ . The Schottky barrier potential was 0.75 V.

A complete set of Y-parameters versus frequency at  $V_{DS}=1.5V$  and  $V_{G}=-0.1V$  has been calculated using the  $S^3A$  method. The seven frequencies are from 24.4 GHz to 170.8 GHz in steps of 24.4 GHz. Figure 5.5 presents a comparison of this data and data obtained with the Monte Carlo particle simulator. In Figure 5.5, at low frequencies all the imaginary parts of the y-parameters are small and at higher frequencies all the y-parameters depart from the Imag(y)=0 axis. The Fourier-decomposition method was used to generate the y-parameters versus frequency in the Monte Carlo simulation. There is a general agreement in this comparison. All four HTM y-parameters have the same behavior as the Monte Carlo results. The Y-parameters versus frequency for the HTM and the DDM are shown in Figure 5.6. This Figure shows that the HTM has a larger  $Re(y_{21})$  than does the DDM. Also, the  $y_{12}$  and  $y_{22}$  for DDM go different directions with those for the HTM. This means that the DDM loses accuracy for short channel length devices.

The complete y-parameter set permits many useful device attributes to be calculated such as current gain  $A_I$ , voltage gain  $A_V$  [48], and unilateral power gain  $G_U$  [49]. This is done as follows:

$$A_I(\omega) = \frac{|y_{21}|}{|y_{11}|} \tag{5.19}$$

$$A_V(\omega) = \frac{|y_{21}|}{|y_{22}|} \tag{5.20}$$

$$G_U(\omega) = \frac{|y_{21} - y_{12}|^2}{4\left[\text{Re}(y_{11})\text{Re}(y_{22}) - \text{Re}(y_{12})\text{Re}(y_{21})\right]}$$
(5.21)

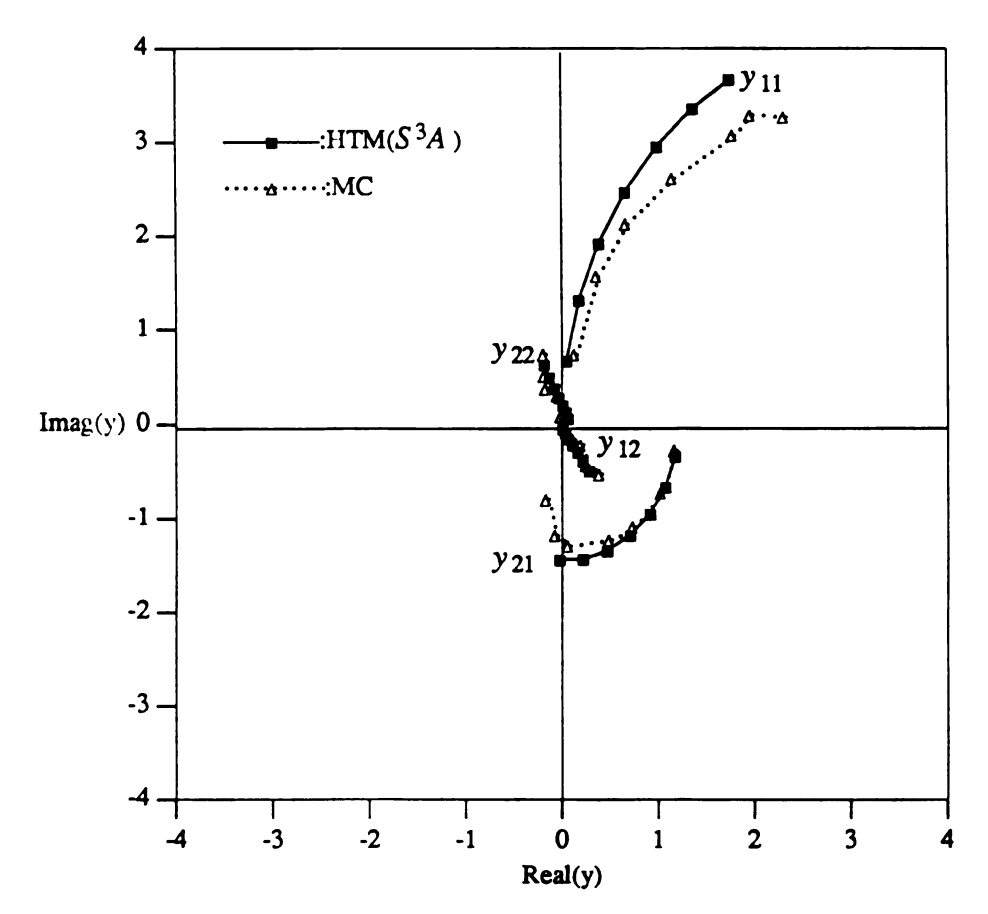


Figure 5.5. A comparison of y-parameters versus frequency for both the HTM method and the Monte Carlo method. The seven frequencies vary from 24.4 GHz to 170.8 GHz in steps of 24.4 GHz.

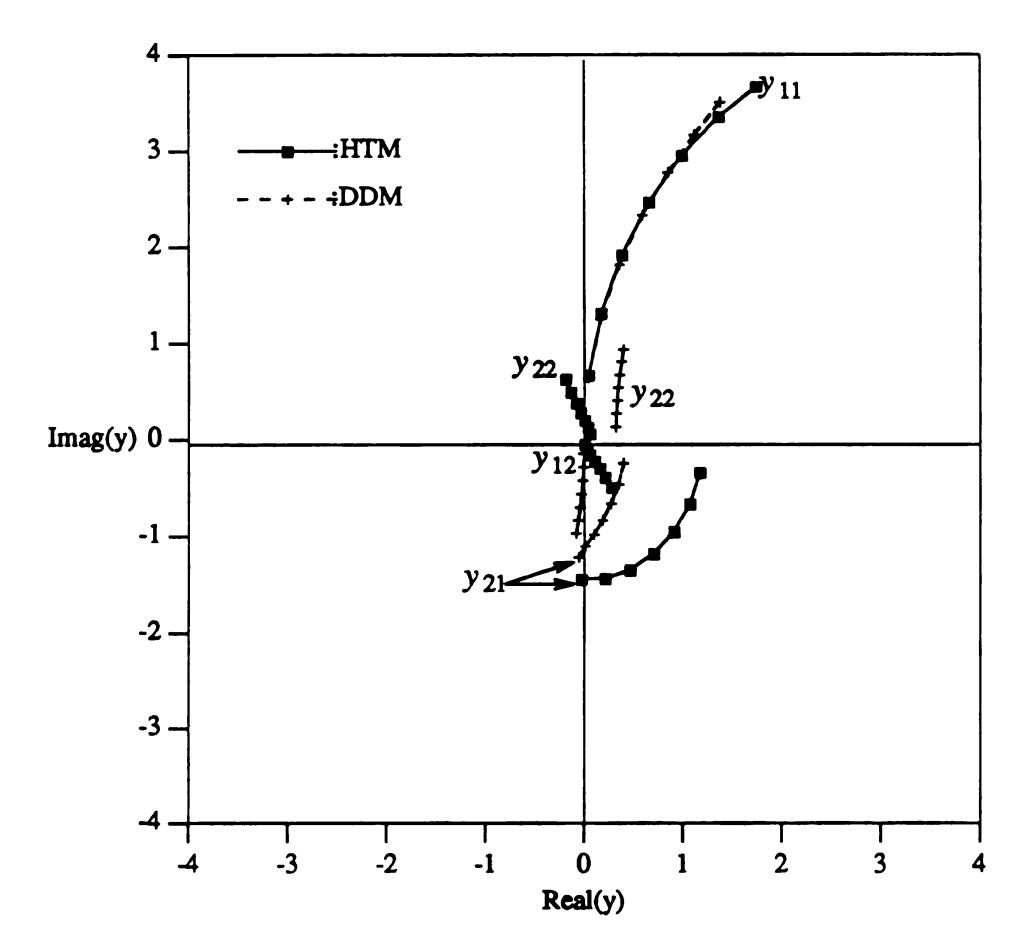


Figure 5.6. A comparison of y-parameters versus frequency for both the HTM method and the DDM method. The seven frequencies vary from 24.4 GHz to 170.8 GHz in steps of 24.4 GHz.

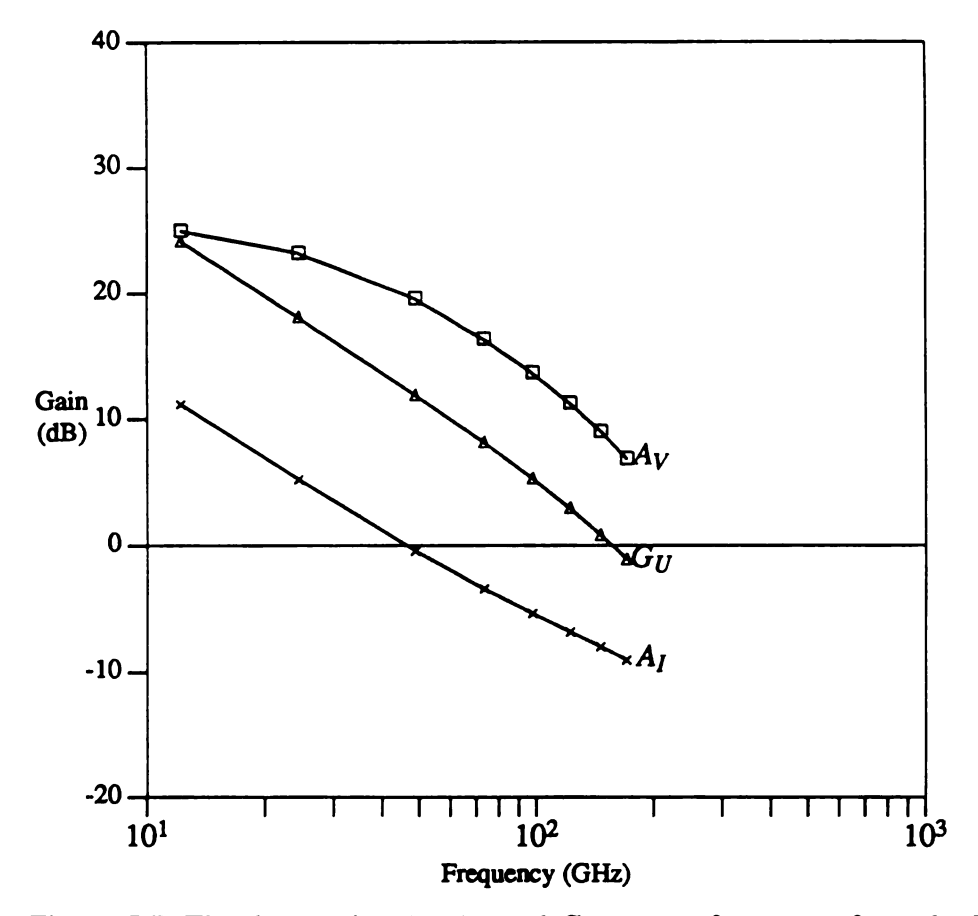


Figure 5.7. The three gains  $A_I$ ,  $A_V$  and  $G_U$  versus frequency from the HTM. The eight frequencies are 12.2, 24.4, 48.8, 73.2, 97.6, 122, 146.4 and 170.8 GHz.

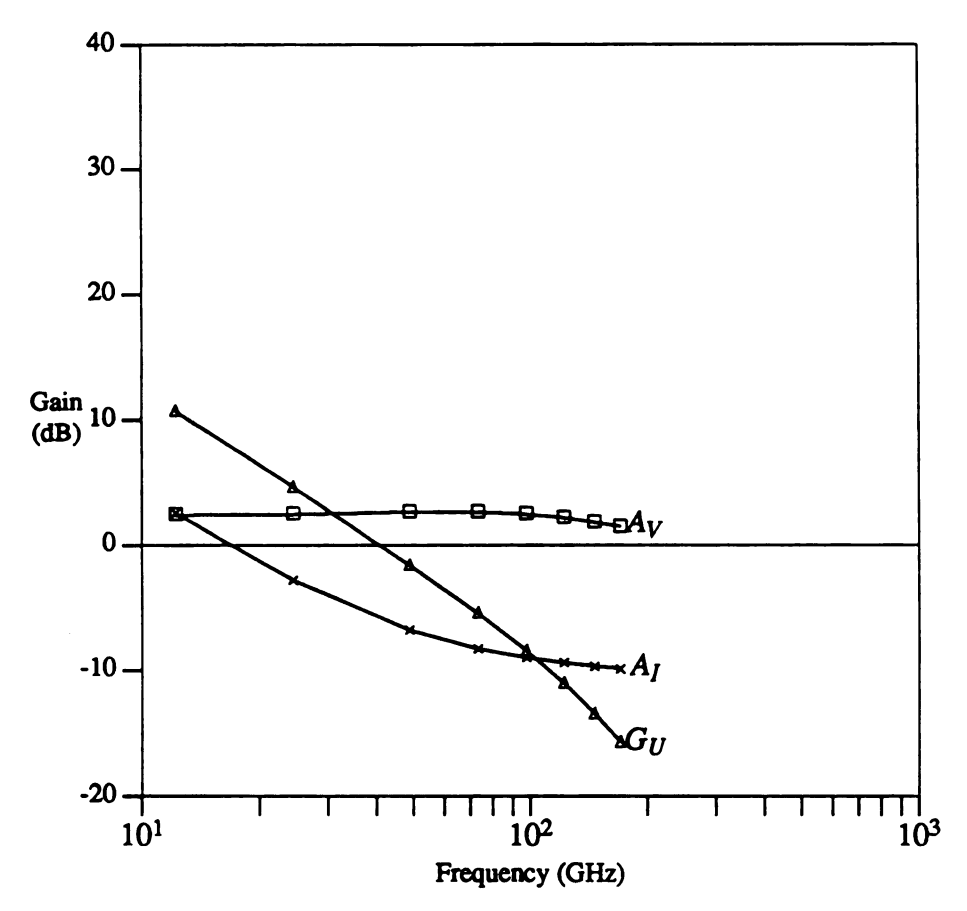


Figure 5.8. The three gains  $A_I$ ,  $A_V$  and  $G_U$  versus frequency from the DDM. The eight frequencies are 12.2, 24.4, 48.8, 73.2, 97.6, 122, 146.4 and 170.8 GHz.

where  $Re(y_{11})$  expresses the real part of  $y_{11}$ . The unity-current-gain frequency  $f_T$  and the maximum frequency of oscillation  $f_{max}$  are both figures-of-merit that are correlated to the microwave and millimeter-wave performance.  $f_T$  and  $f_{max}$  are the frequencies at which equations (5.19) and (5.21) are equal to unity, respectively.

In Figure 5.6, the HTM gives a transconductance  $g_m = 120.28 \, mS/mm$ , and the DDM gives  $g_m = 41.44 \, mS/mm$  for low frequences. These values came from the real part of  $y_{21}$ . Similarly, the gate capacitance  $c_g$  at low frequencies can be calculated from the imaginary part of  $y_{11}$ . Figure 5.7 and Figure 5.8 shows the three gain values versus frequency for the HTM and DDM models, respectively. The eight frequencies are 12.2, 24.4, 48.8, 73.2, 97.6, 122, 146.4 and 170.8 GHz. By setting current gain  $A_I(\omega) = \frac{|y_{21}|}{|y_{11}|} = 1$  [48], which corresponds to 0dB on the plot, the HTM gives a unity current gain frequency of  $f_T$ =45.98 GHz and the DDM gives  $f_T$ =17.1 GHz. By setting the unilateral power gain  $G(\omega) = 1$ , the HTM gives  $f_{max} = 154.95 \, GHz$ , and the DDM gives  $f_{max} = 40.49 \, GHz$ . This shows that the DDM underestimates  $f_T$  and  $f_{max}$ , and that the nonstationary effects are important for submicrometer devices.

## 5.4 AC Performance of GaAs MESFETs

The AC performance of MESFETs depends on the geometric structure and the bias. This section applies the HTM AC simulator to the study of these dependencies. The gain and frequency performances of microwave and millimeter-wave transistors are generally specified in terms of  $G_U$  (5.21) and  $f_{\rm max}$ .  $f_{\rm max}$ , the frequency at which  $G_U$  is unity, is a particularly important figure of merit as it is the maximum frequency of oscillation. It indicates the boundary between an active and passive device. Common practice has been to estimate  $f_{\rm max}$  using extrapolation of the microwave frequency gain measurements at -6 dB per octave. However, some works [50-53] have pointed out that parasitic resistance and capacitance cause the unilateral power gain of

FETs to roll off at a -12 dB per octave. Hence, the extrapolated  $f_{\rm max}$  value are considerably greater than the actual  $f_{\rm max}$  value.

The gain slope changes are explained in the work of Steer [51] as follows. The circuit model of a common source MESFET is shown in Figure 5.9. The best possible gain and frequency performance of the transistor will be obtained when the parasitics are negligible, so Steer considered the performance of the intrinsic transistor alone which has the unilateral power gain

$$G_U = \left[ \frac{g_{m0}^2 R_{DS}}{4 C_{GS} R_I (C_{GS} - C_{DC} g_{m0} R_{DS})} \right] \left[ \frac{1}{\omega^2 (1 - p^2 \omega^2)} \right]$$
 (5.22)

where

$$p^{2} = \frac{(R_{I}^{2}C_{GS})(C_{DC} + C_{GS})^{2} + C_{DC}g_{m0}R_{DS}\tau^{2}/2}{(C_{DC}g_{m0}R_{DS} - C_{GS})}.$$
 (5.23)

At frequencies much less than  $(2\pi R_I C_{GS})^{-1}$  and ignoring  $C_{DC}$ ,  $G_U$  reduces to

$$G_U = \frac{g_{m0}^2 R_{DS}}{4\omega^2 C_{GS}^2 R_I} \ . \tag{5.24}$$

The commonly used expression for  $G_U$ , (5.24), rolls off at -6 dB/octave because of  $1/\omega^2$  term. However, with  $C_{DC}$  in (5.22), there is an additional -6 dB/octave roll-off at high frequencies due to the complex pole pair contained in the  $1/(1-p^2\omega^2)$  term. The complex conjugate poles are at the frequency

$$f_p = \frac{1}{2\pi |p|}. (5.25)$$

For millimeter-wave transistors this pole frequency is typically below  $f_{\text{max}}$  so that the pole has a limiting effect on frequency performance [51].

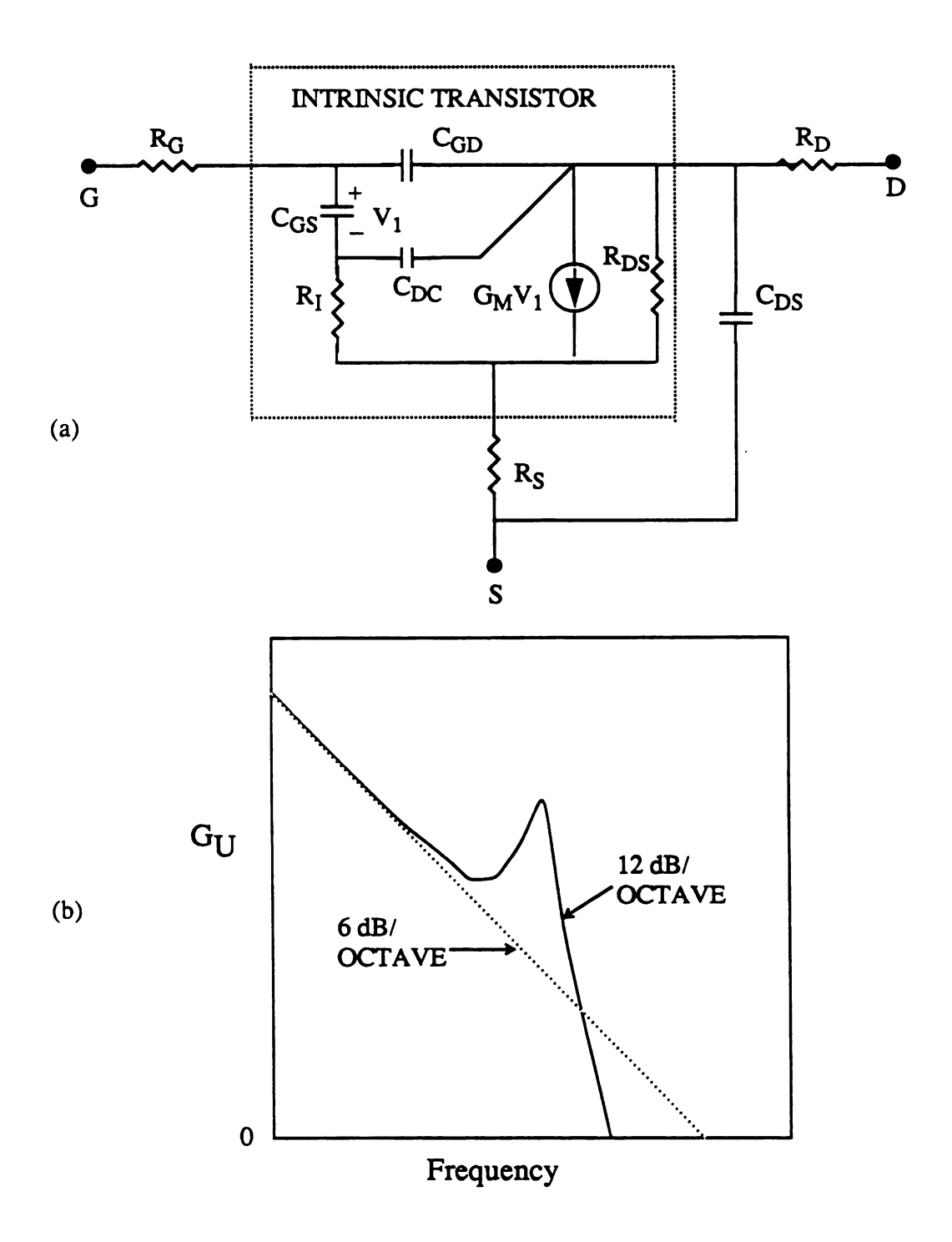


Figure 5.9. (a) Circuit model of a MESFET. (b) The extrapolation of the low-frequency gain overestimates the unity power gain frequency,  $f_{max}$ .

One approach to estimating  $f_{\text{max}}$  is to use an equivalent circuit model developed from physical insight as well as 2-port measurements to determine the value for each model component [51]. However, errors can be made due to the inaccuracy of the equivalent circuit model, due to uncorrected parasitics in the measurement and due to the extrapolation of low frequency measurements to high frequencies. Another more accurate approach to estimate  $f_{\text{max}}$  for short channel FETs is to extract the y-parameters from a device simulator using the HTM directly in the frequency domain. In this case, errors due to the equivalent circuit model and due to the quasi-static assumption can be precluded.

Using the HTM model the frequency behavior of the MESFET with various geometric and bias parameters have been simulated. In particular, investigations of the  $G_U$  versus frequency dependence on device parameters have been studied. The device parameters studied include (1) drain bias dependence, (2) gate bias dependence, (3) gate length dependence, (4) gate-source spacing dependence, (5) gate-drain spacing dependence, (6) epilayer thickness dependence, and (7) substrate dependence. The nominal device has  $L_{GS}$ =0.4 $\mu m$ ,  $L_G$  = 0.4 $\mu m$ , and  $L_{GD}$  = 0.6 $\mu m$  as shown in Figure 4.1. The device doping was a constant n-type doping of  $2.0\times10^{17}cm^{-3}$  for the active layer. The depth of the active layer was  $0.1\mu m$  and the Schottky barrier potential was  $0.75\,V$ .

## 5.4.1 Drain Bias Dependence

Figure 5.10 shows  $G_U$  versus frequency for  $V_D = 1.0$ , 1.5 and 2.0 V. The  $f_{\rm max}$  determined from Figure 5.10(a) is shown in Figure 5.10(b). This maximum  $f_{\rm max}$  is near  $V_{DS} = 1V$ .

#### 5.4.2 Gate Bias Dependence

Figure 5.11 shows  $G_U$  versus frequency for  $V_G = 0.0, -0.2$  and -0.4 V. The  $f_{\text{max}}$  determined from Figure 5.11(a) is shown in Figure 5.11(b).

#### 5.4.3 Gate Length Dependence

Figure 5.12 shows  $G_U$  versus frequency for  $L_G = 0.2,0.4$  and  $0.6 \,\mu m$ . The  $f_{\rm max}$  determined from Figure 5.12(a) is shown in Figure 5.12(b). Some features can be observed: (1) the  $f_{\rm max}$  decreases with increasing  $L_G$ , (2) the slope changes from -6 dB/octave to -12 dB/octave particularly for the long channel device. The unity power gain frequency using a -6dB/octave extrapolation over-estimates the  $f_{\rm max}$  and results in a larger error for the longer channel device  $f_{\rm max}$  than for the short channel device.

## 5.4.4 Gate-Source Spacing Dependence

Figure 5.13 shows  $G_U$  versus frequency for  $L_{GS} = 0.2,0.4$  and  $0.8 \, \mu m$ . The  $f_{\rm max}$  determined from Figure 5.13(a) is shown in Figure 5.13(b). The  $f_{\rm max}$  decreases only slightly with increasing  $L_G$ . For this particular structure the parasitic source resistance is seen to have only a small effect on  $f_{\rm max}$ .

#### 5.4.5 Gate-Drain Spacing Dependence

Figure 5.14(a) shows  $G_U$  versus frequency for  $L_{GD}=0.2,0.4$ , and  $0.8\,\mu m$ . The  $f_{\rm max}$  determined from 5.14(a) is shown in Figure 5.14(b). The longer  $L_{GD}$  value gives a smaller drain-to-gate feedback capacitance, hence, a longer  $L_{GD}$  gives a higher  $f_{\rm max}$ .

#### 5.4.6 Epilayer Thickness Dependence

Figure 5.15(a) shows  $G_U$  versus frequency for a=0.1 and  $0.12\mu m$ . The smaller epilayer thickness gives the larger  $f_{\rm max}$  because of the tighter control by the gate voltage  $V_{GS}$ . Since a non-ideal substrate permits both current flow and a reduction in fields at the substrate/epilayer interface, the sensitivity of performance to epilayer thickness in a real device will be somewhat less than that presented here [11].

# 5.4.7 Substrate Dependence

Figure 5.16(a) shows  $G_U$  versus frequency with substrate and without substrate. The doping profile with substrate is shown in Figure 5.16(b). The bias point is  $V_{DS}=1.0\ V$  and  $V_{GS}=-0.2\ V$ . The device with substrate has a lower  $f_{\rm max}$ .

Table 5.4.1 shows the various simulation with different dependence, the  $f_{\rm max}$  corresponding to each case is also included.

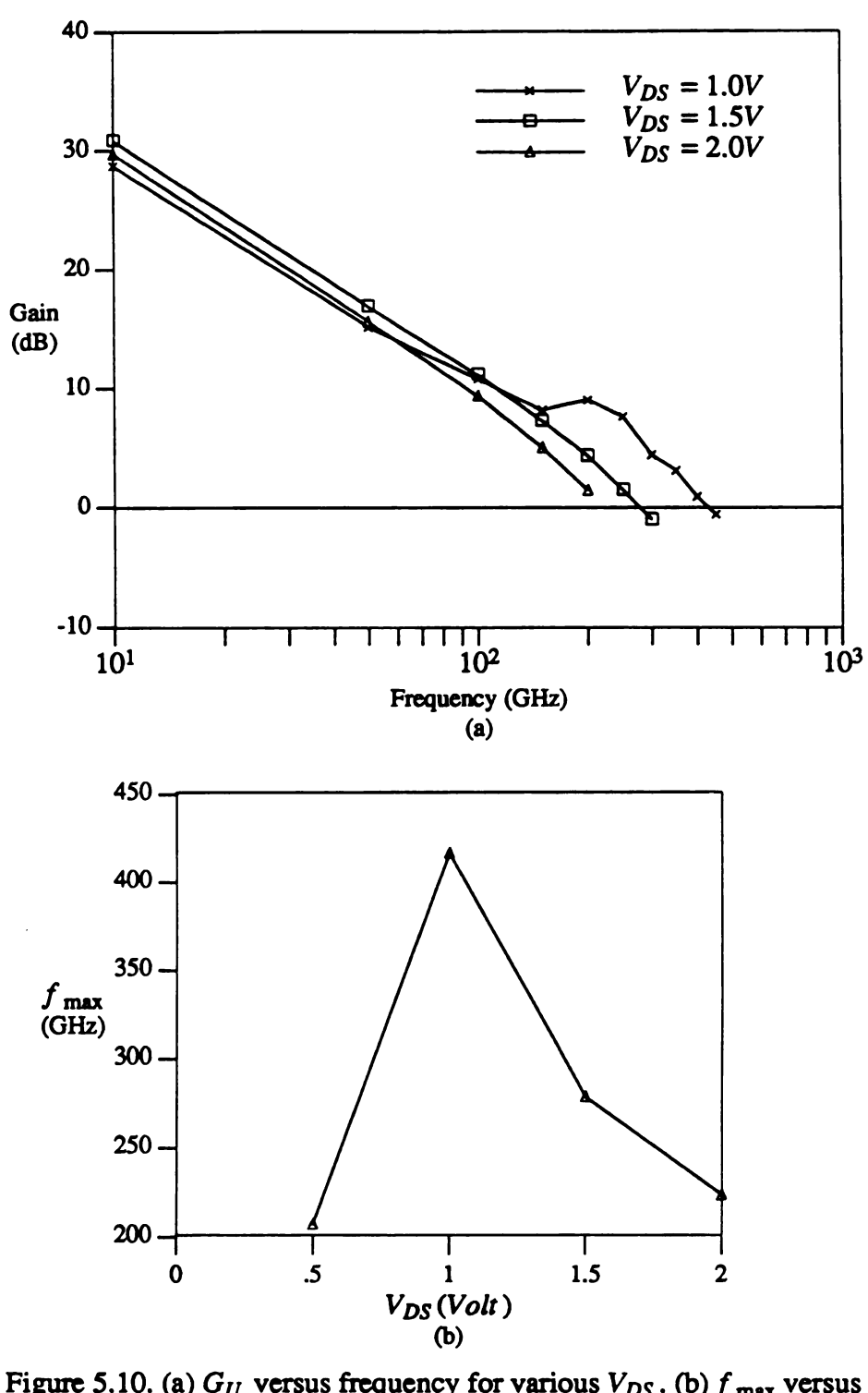


Figure 5.10. (a)  $G_U$  versus frequency for various  $V_{DS}$ . (b)  $f_{\max}$  versus  $V_{DS}$ .

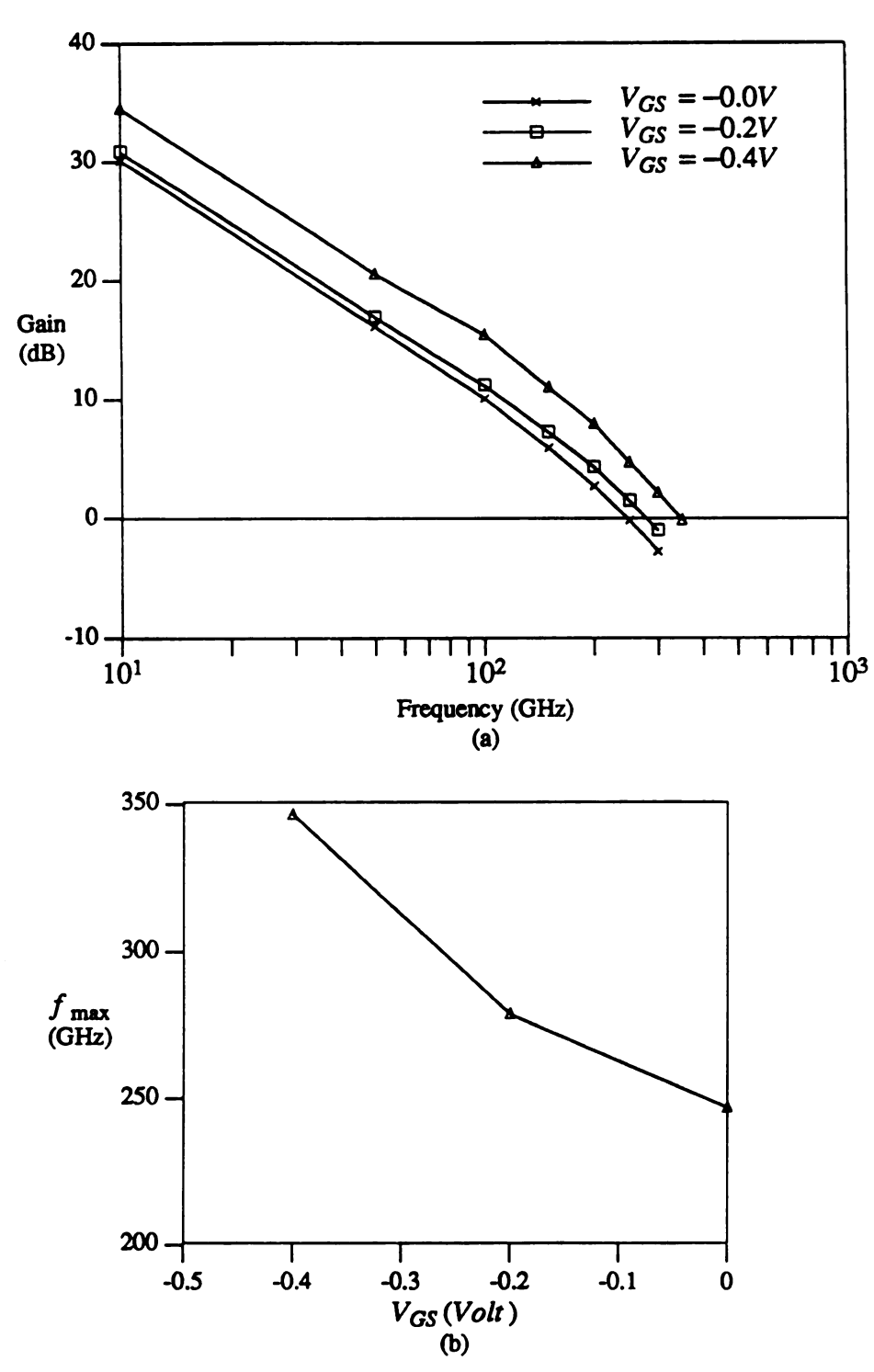


Figure 5.11 (a)  $G_U$  versus frequency for various  $V_{GS}$ . (b)  $f_{\max}$  versus  $V_{GS}$ .

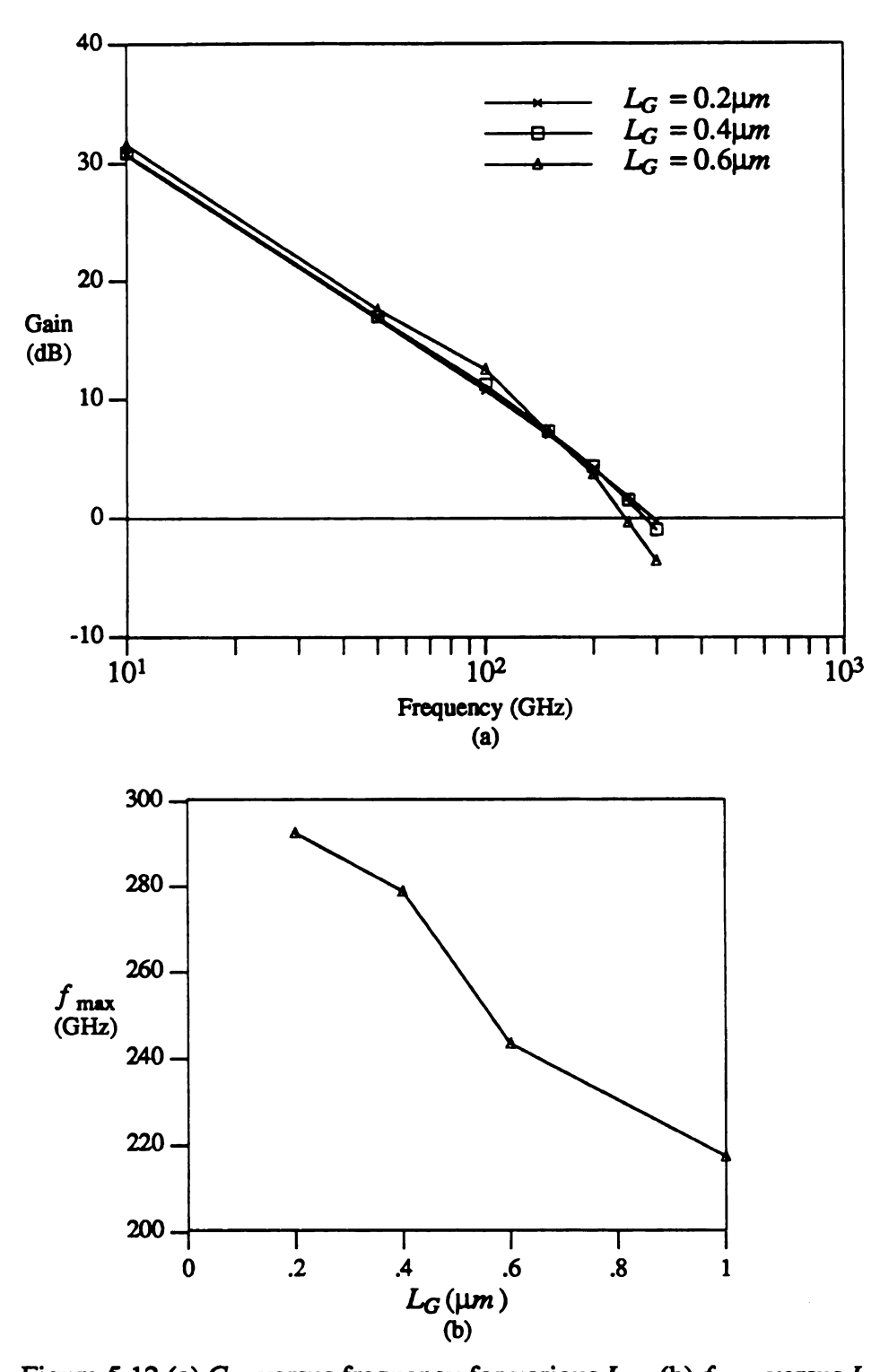


Figure 5.12 (a)  $G_U$  versus frequency for various  $L_G$ . (b)  $f_{\max}$  versus  $L_G$ .

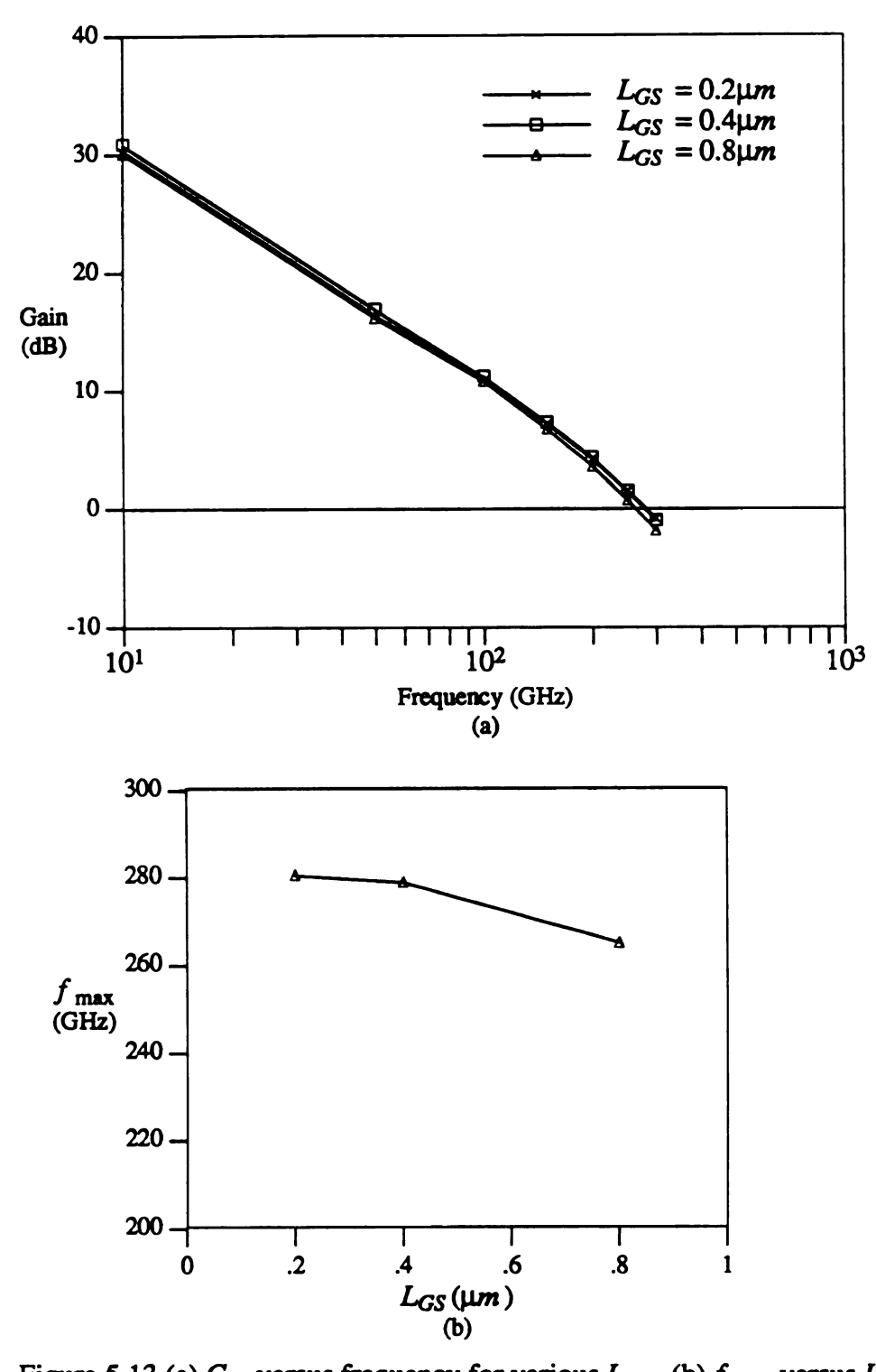


Figure 5.13 (a)  $G_U$  versus frequency for various  $L_{GS}$ . (b)  $f_{\max}$  versus  $L_{GS}$ .

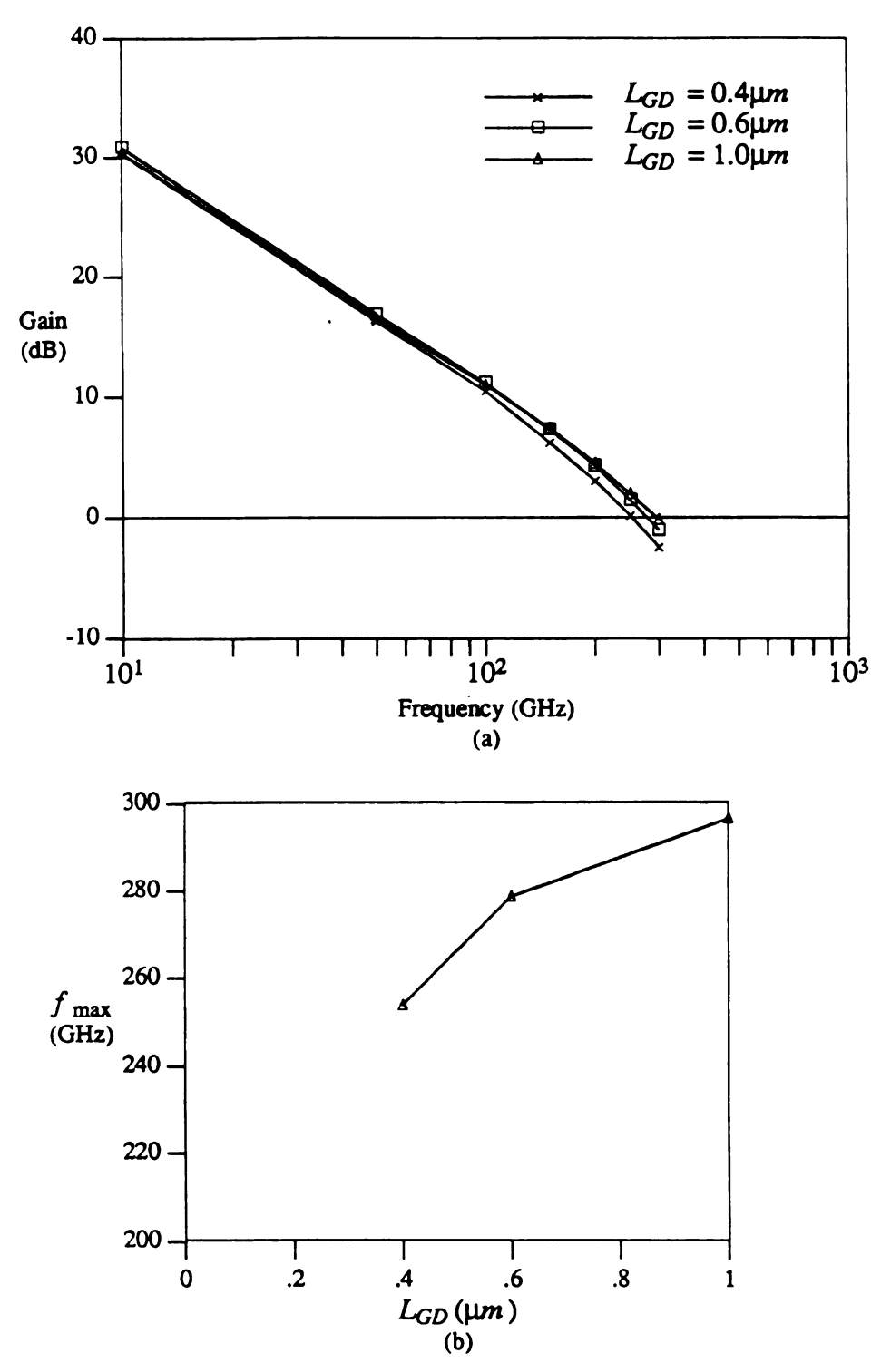


Figure 5.14. (a)  $G_U$  versus frequency for various  $L_{GD}$ . (b)  $f_{\max}$  versus  $L_{GD}$ .

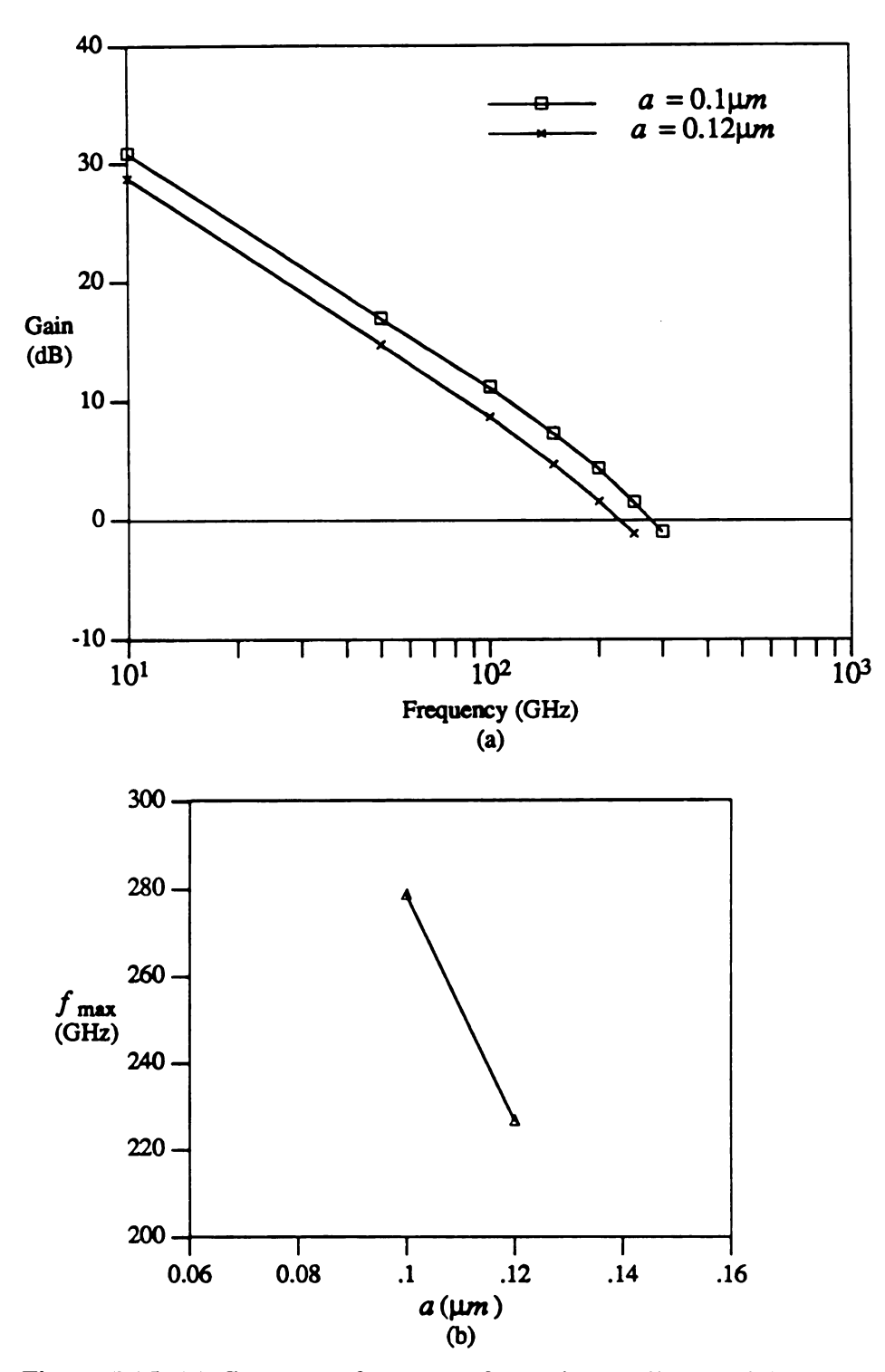


Figure 5.15. (a)  $G_U$  versus frequency for various epilayer thickness a. (b)  $f_{\max}$  versus a.

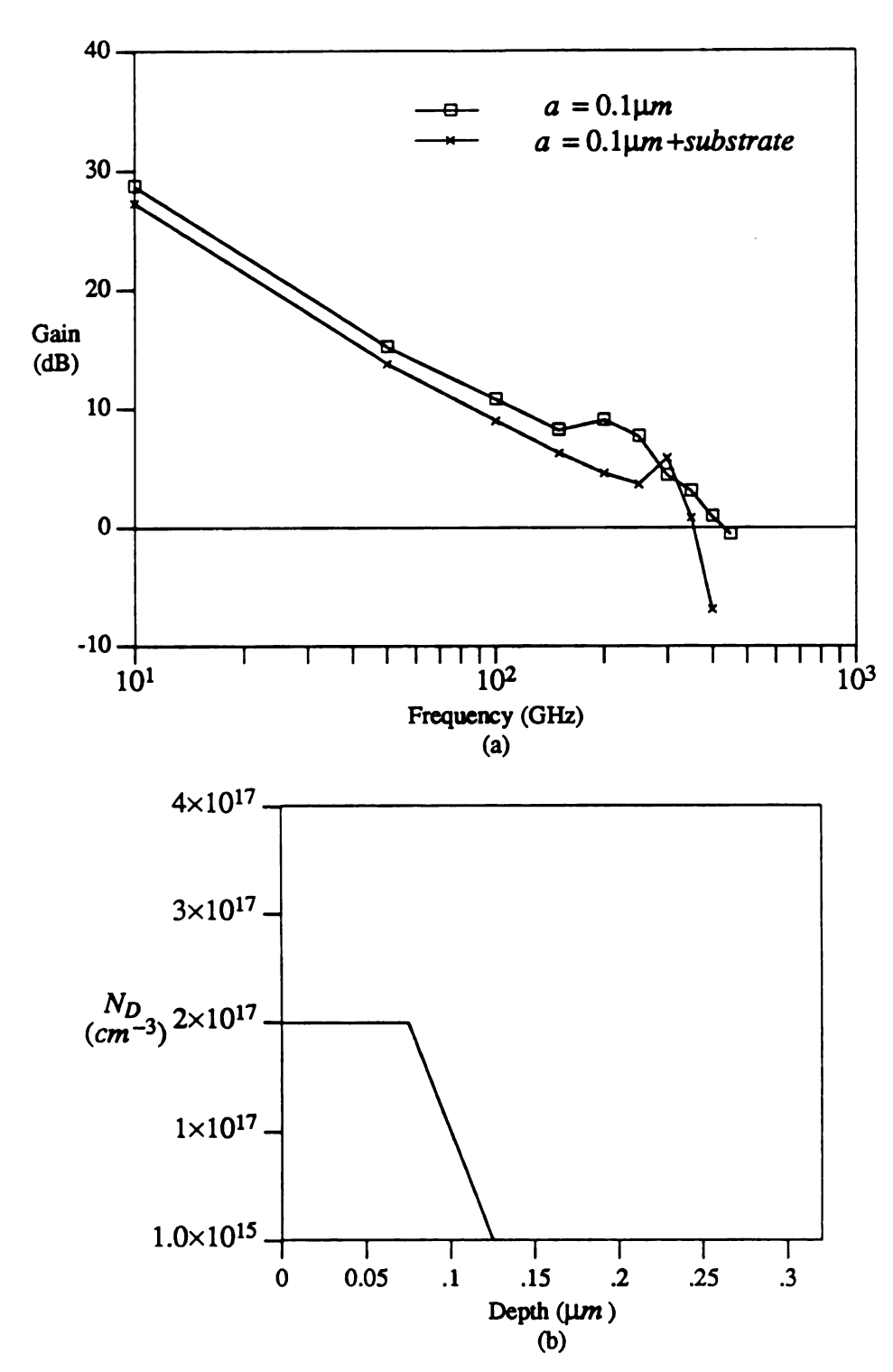


Figure 5.16. (a)  $G_U$  versus frequency with or without substrate. (b)  $N_D$  versus depth.

Table 5.1  $f_{max}$  dependence on device parameters for  $N_D = 2 \times 10^{17} cm^{-3}$ .

L <sub>D</sub> (μm)	L <sub>GS</sub> (µm)	L <sub>GD</sub> (µm)	a(µm)	V <sub>DS</sub> (V)	V <sub>GS</sub> (V)	f <sub>max</sub> (GHz)
0.4	0.4	0.6	0.1	1.5	-0.2	278.8
				0.5		207.2
				1.0		416.5
				2.0		223.7
					-0.0	246.9
					-0.4	346.6
0.2						292.6
0.6						243.5
1.0						217.5
	0.2					280.4
	0.8					265.0
		0.4				254.0
		1.0				296.8
			0.12			226.9
			0.15	1.0		361.6

0.1<sup>s</sup> means device with substrate.

#### **CHAPTER 6**

### HYDRODYNAMIC TRANSPORT MODEL FOR THE MODFET

## 6.1 Hydrodynamic Transport Equations for the MODFET

The basic device topology of the MODFET (modulation-doped field effect transistor) is shown in Figure 6.1, and the energy band diagram along the y direction is shown in Figure 6.2. Electrons accumulate at the interface between the two materials as a result of band bending. The ionized donor impurities in the AlGaAs and the conduction band electrons in the quantum well are spatially separated. This results in a substantial reduction in the ionized impurity scattering in the GaAs layer which leads to enhanced electron mobilities, particularly at low temperatures. The potential well formed at the heterojunction is normally narrow enough to have quantized energy levels in the y-direction and behaves as a two-dimensional electron gas. Up to this date there are relatively few numerical MODFET solutions using the hydrodynamic equations. Two reports are those of Widiger et al. [15] and Shawki et al. [54].

In Widiger's model, electron transport in the MODFET can take place in both the bulk GaAs and in the quantum well (assuming the AlGaAs is depleted). In the region near the source where the fields are small the conduction process may be attributed mainly to the lowest quantum sub-band. In contrast, at the pinchoff region towards the drain end of the gate, the electron current will be principally in the bulk. Electron transfer between the quantized subbands 2-D gas and the bulk 3-D gas is present whenever the average electron energies are comparable to the subband energy spacings. Widiger assumed only the lowest subband was a two-dimensional gas system. The higher subbands were all treated as part of the three dimensional gas system. This may be assumed since, when conditions allow significant transfer out of the lowest subband, the higher subbands will be spaced sufficiently close so as to approach

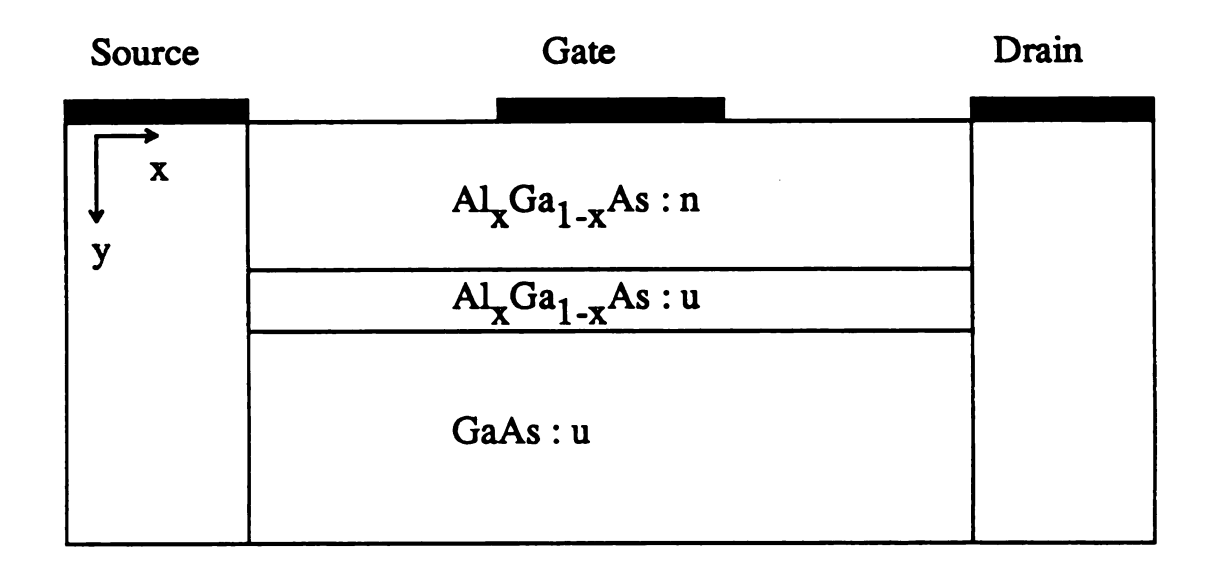


Figure 6.1 Basic device topology of the MODFET.

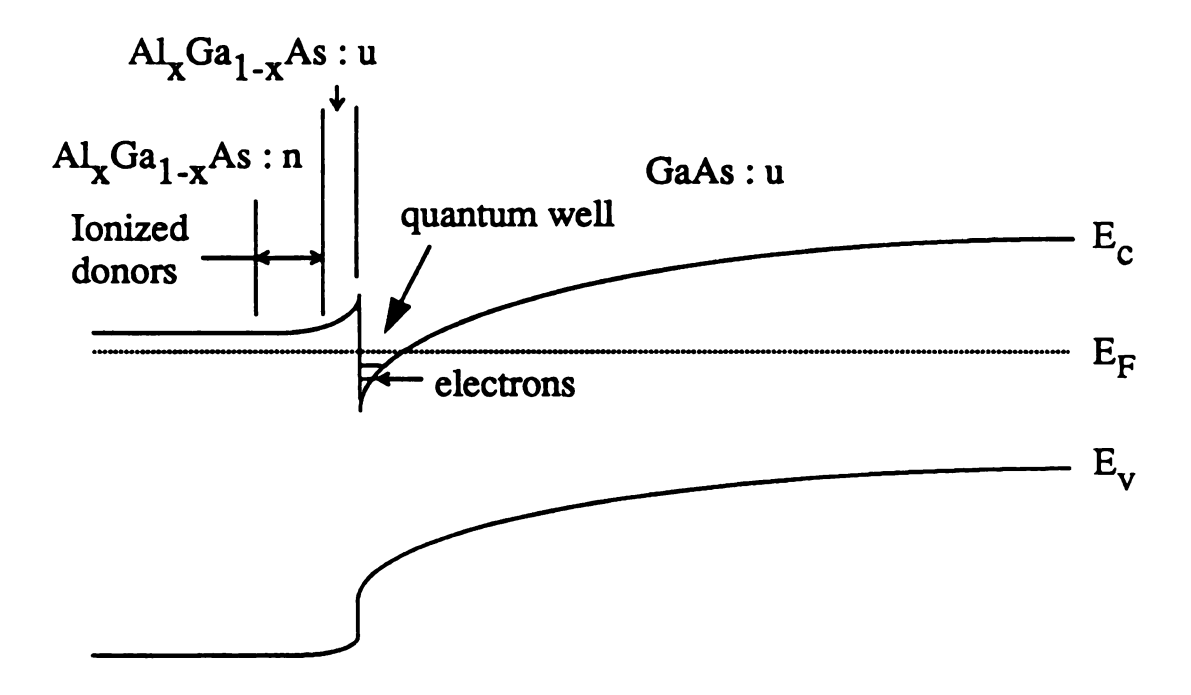


Figure 6.2 Energy band diagram for a MODFET.

three-dimensional properties. The quantum well and bulk systems are then coupled by allowing the electrons to scatter between the two-dimensional and three-dimensional gas systems. The equation for transport in the quantum well are similar to those of a three-dimensional gas ((2.44)-(2.46)) with the addition of coupling terms since electrons can transfer to the bulk system. These coupling terms are analogous to generation-recombination terms. Widiger assumed no current conduction in the AlGaAs layer.

Shawki et al. [54] applied a hydrodynamic energy model that is valid in the framework of a gradual variation in Al alloy composition to simulate the entire MOD-FET region including the top AlGaAs layer. This model treats the electrons as a three-dimensional electron gas without considering two-dimensional quantum well effects. This is justified from Monte Carlo simulations of submicron MODFET's[55] which demonstrated that electrons during the major part of their travel under the gate are not confined in quantum subbands if the drain bias is high enough to heat the electrons (for  $V_{DS} = 0.5$  V, the total subband population is found to be less than 15 percent of the equilibrium one). Also, the literature results for the two-dimensional electron gas (2DEG) behavior obtained from classical models based on either Boltzmann or Fermi-Dirac statistics are generally comparable with those obtained from the exact self-consistent solution of Schrodinger's and Poisson's equations [56]. This model without 2DEG treatment makes the model more compatible with that of MESFET's.

This study will extend the MESFET HTM model in previous chapters to include a heterojunction for MODFET simulation. The electron transport dynamics based on the particle, momentum, and energy conservation equations for a heterojunction are described[54] by:

$$\frac{\partial n}{\partial t} + \nabla \cdot (n \, \mathbf{v}) = 0 \tag{6.1}$$

$$\frac{\partial}{\partial t} \frac{(nm^*(\xi)v)}{q} + \nabla \cdot \frac{vnm^*(\xi)v}{q} + n \frac{v}{\mu(\xi)}$$

$$= n \left[ \nabla (\psi + \frac{\chi}{q}) - \frac{\nabla (nk_B T(\xi)\gamma)}{nq} + \frac{w}{q} \nabla \ln^*(\xi) \right]$$
(6.2)

$$\frac{\partial(n\,\xi)}{\partial t} + \nabla \cdot n\,\mathbf{v}(\xi + k_B T(\xi)\gamma) + \nabla \cdot \mathbf{Q} = -n\,\mathbf{v} \cdot \nabla(-q\,\psi - \chi) - n\frac{\xi - \frac{3}{2}k_B T_0\gamma}{\tau_{\xi}(\xi)} \tag{6.3}$$

$$\gamma(\eta) = \frac{F_{3/2}(\eta)}{F_{1/2}(\eta)} \tag{6.4}$$

$$\eta = \frac{(E_{fn} - E_c)}{k_B T(\xi)} \tag{6.4b}$$

$$w = \frac{1}{2}m^{*}(\xi)v^{2} + \frac{3}{2}k_{B}T(\xi)$$
 (6.5)

$$\xi = w + U_p . \tag{6.6}$$

The three moment equations are solved together with Poisson equation

$$\nabla \cdot (\varepsilon \nabla \psi) = -q \left( N_D^+ - n \right) \tag{6.7}$$

where

$$N_D^{+} = \frac{N_D}{\frac{(E_{fa} - E_{d})}{k_B T(\xi)}}.$$
(6.8)

It should be mentioned that the conservation equations (6.1)-(6.3) presented above are different from those we used for the simulation of MESFET's in previous chapters in two aspects. The first difference is the terms describing the gradient in electron affinity and the second difference is the dependence of effective mass on position.

The model described above can be simplified as

$$\nabla \cdot \varepsilon \nabla \psi = -q \left( N_D - n \right) \tag{6.9}$$

$$\frac{\partial n}{\partial t} - \nabla \cdot \mathbf{J} = 0 \tag{6.10}$$

$$\frac{\partial n \, \xi}{\partial t} + \nabla \cdot \mathbf{S} = \mathbf{J} \cdot \mathbf{E} - n \frac{\xi - \xi_0}{\tau_{\xi}} \tag{6.11}$$

where

$$J = -qnv$$

$$= \mu(qn\mathbf{E} + \nabla(nk_BT)) \tag{6.12}$$

$$S = -\frac{\mathbf{J}}{q}(\xi + k_B T) + \mathbf{Q} \tag{6.13}$$

$$\mathbf{E} = -\nabla \left[ \Psi + \frac{\chi}{q} + \frac{k_B T}{q} \ln N_c \right]. \tag{6.14}$$

Notice that the term associated with  $\ln N_c$  came from  $\nabla \gamma$  in the momentum and energy conservation equations (6.1) and (6.2) which can be derived by following the work of Azoff [57]. Q is the heat flow shown in equation (2.54). The equations (6.9)-(6.14) are the same as those used in the work of Horio for the heterojunction bipolar transistor [58].

The boundary conditions for the MODFET are the same as those for the MESFET except for the ohmic contacts and the heterojunction. Usually there is a highly doped region under source and drain contact to reduce the source and drain resistance. The current across the heterojunction in the highly doped ohmic contact region is mostly due to tunneling conduction [59]. The highly doped ohmic contact regions behave as a small resistor r to parallel with the large heterojunction resistor R as shown schematically in Figure 6.3(a). This will reduce the current across the heterojunction in non-ohmic contact region. Hence, it is expected that most current flows as shown in Figure 6.3(b). Very little current flows across the heterojunction in the non-ohmic region. Also, the current flow in the top layer is very small due to depletion by the gate. This is similar to Widiger's work[15]. Different boundary conditions have

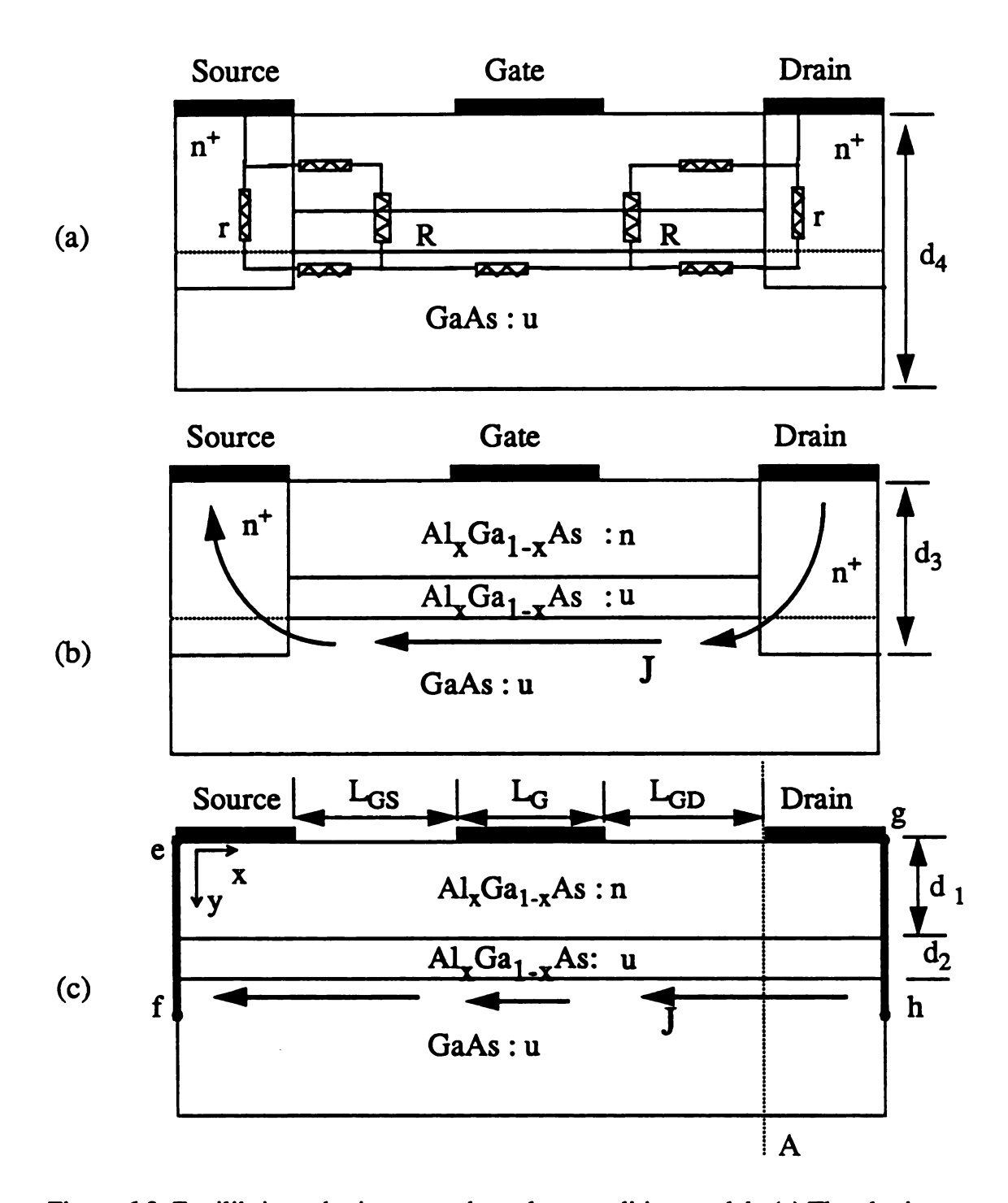


Figure 6.3. Equilibrium ohmic contact boundary condition model. (a) The ohmic contact behaves as a small resistance r in parallel with the large heterojunction resistance R. (b) Most current flows through r, not R. (c) A simplification of (b) based on equilibrium ohmic contact boundary condition at (e-f) and (g-h).

been used in the works of Loret [60] and Shawki [54], which results in wide spread current distribution across the heterojuction, not just confined to the source and drain ohmic contact regions. In this study, the ohmic contacts (e-f) and (g-h) in Figure 6.3(c) are used. The potential, electron concentration and electron energy are calculated for this vertical boundary by assuming local thermal equilibrium conditions. Specifically, the electric field and current can terminate at these boundaries and no current flows in the vertical direction as shown in Figure 6.3(c). This is achieved by solving the potential  $\psi$  and the electron density n subject to the energy condition  $T = T_0$ . The current J and the energy flux S which cross the heterojunction are assumed to be zero. The drain current is calculated by summing the current through the cross section A in Figure 6.3(c).

#### 6.2 Simulation Results and Discussion

The structure used for the simulations had  $L_{GS}$ =0.6 $\mu m$ ,  $L_{G}$  = 0.4 $\mu m$ ,  $L_{GD}$  = 0.6 $\mu m$ ,  $d_1$ =50nm,  $d_2$ =5nm,  $d_3$ =150nm, and  $d_4$ =320nm as shown in Figure 6.3. The doped  $Al_xGa_{1-x}As$  has n-type doping  $N_D$ =5×10<sup>17</sup> $cm^{-3}$ , the undoped  $Al_xGa_{1-x}As$  has n-type doping  $N_D$ =1×10<sup>14</sup> $cm^{-3}$  and the undoped GaAs has n-type doping  $N_D$ =1×10<sup>14</sup> $cm^{-3}$ . For GaAs, the relative dielectric constant is 12.9 and the density of states in the conduction band is  $N_c$ =4.350×10<sup>17</sup> $cm^{-3}$ . For  $Al_xGa_{1-x}As$ , the fraction x in  $Al_xGa_{1-x}As$  is 0.3 with a correspond relative dielectric constant of 12.3, and a density of states in conduction band of  $N_c$ =6.988×10<sup>17</sup> $cm^{-3}$ . The conduction band discontinuity is 0.23 eV. The Schottky barrier potential is 0.75 V [54,56] and the low field mobility is assumed to be 0.5  $m^2V^{-1}S^{-1}$ .

Figure 6.4 shows the current-voltage characteristics for  $V_G$ =0.0V and  $V_G$ =0.2V. Figure 6.5 shows the conduction band edge distribution. It is seen that most of the voltage drop is under the gate edge near the drain. Figure 6.6 shows the electron distribution where electrons have accumulated at the heterojunction due to the conduction

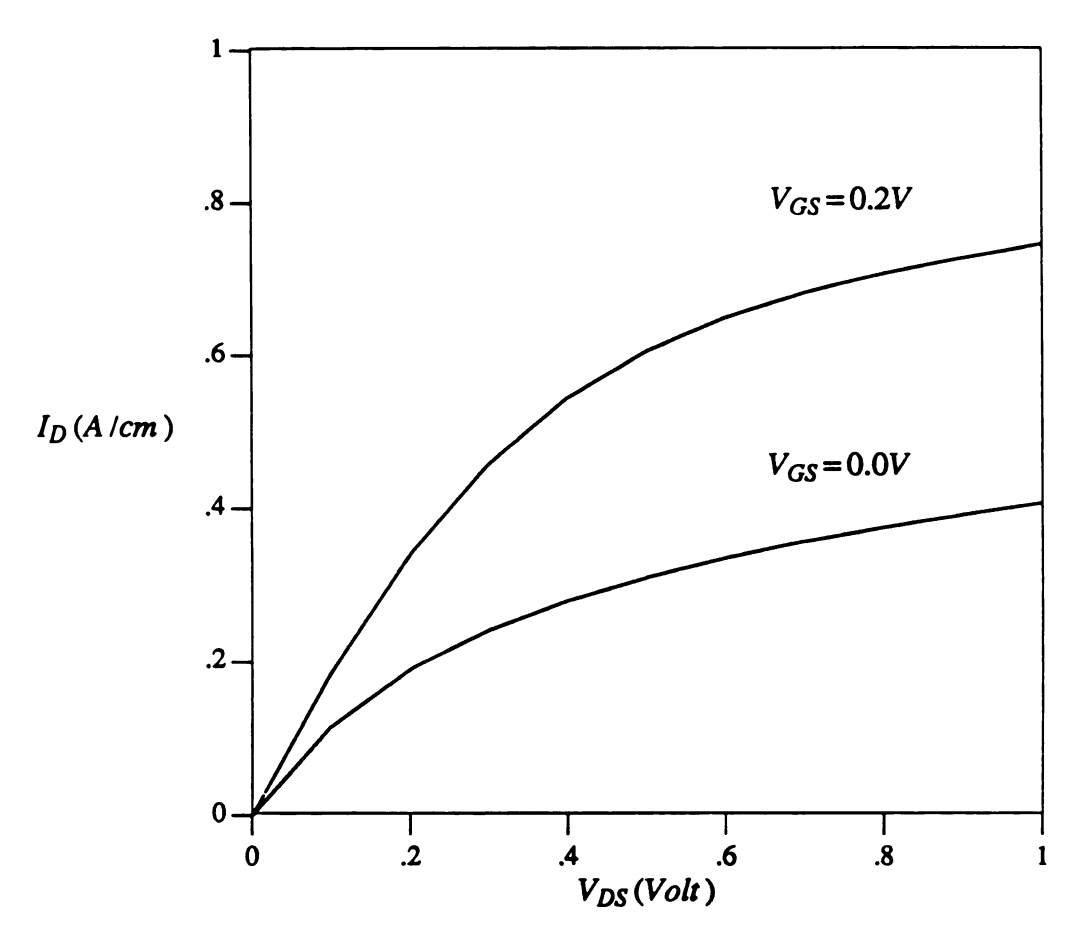


Figure 6.4. The current-voltage characteristics of the MODFET for  $V_{GS} = 0.0V$  and  $V_{GS} = 0.2V$ .

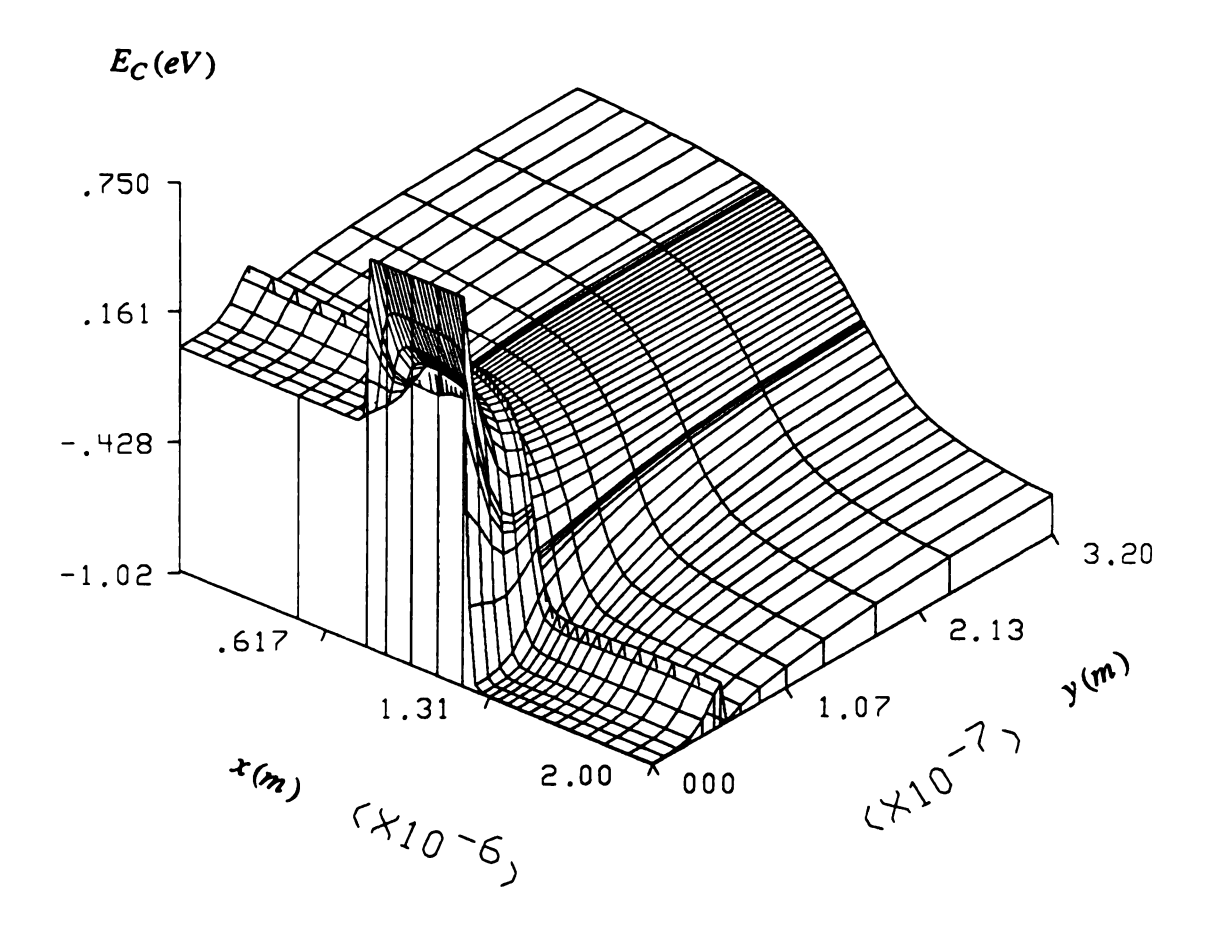


Figure 6.5. The conduction band distribution (eV) over the entire device for  $V_{GS} = 0.0 V$  and  $V_{DS} = 1.0 V$ . The source is the front left region and the drain is the front right region. The gate extends from  $0.8 \ \mu m$  to  $1.2 \ \mu m$ .

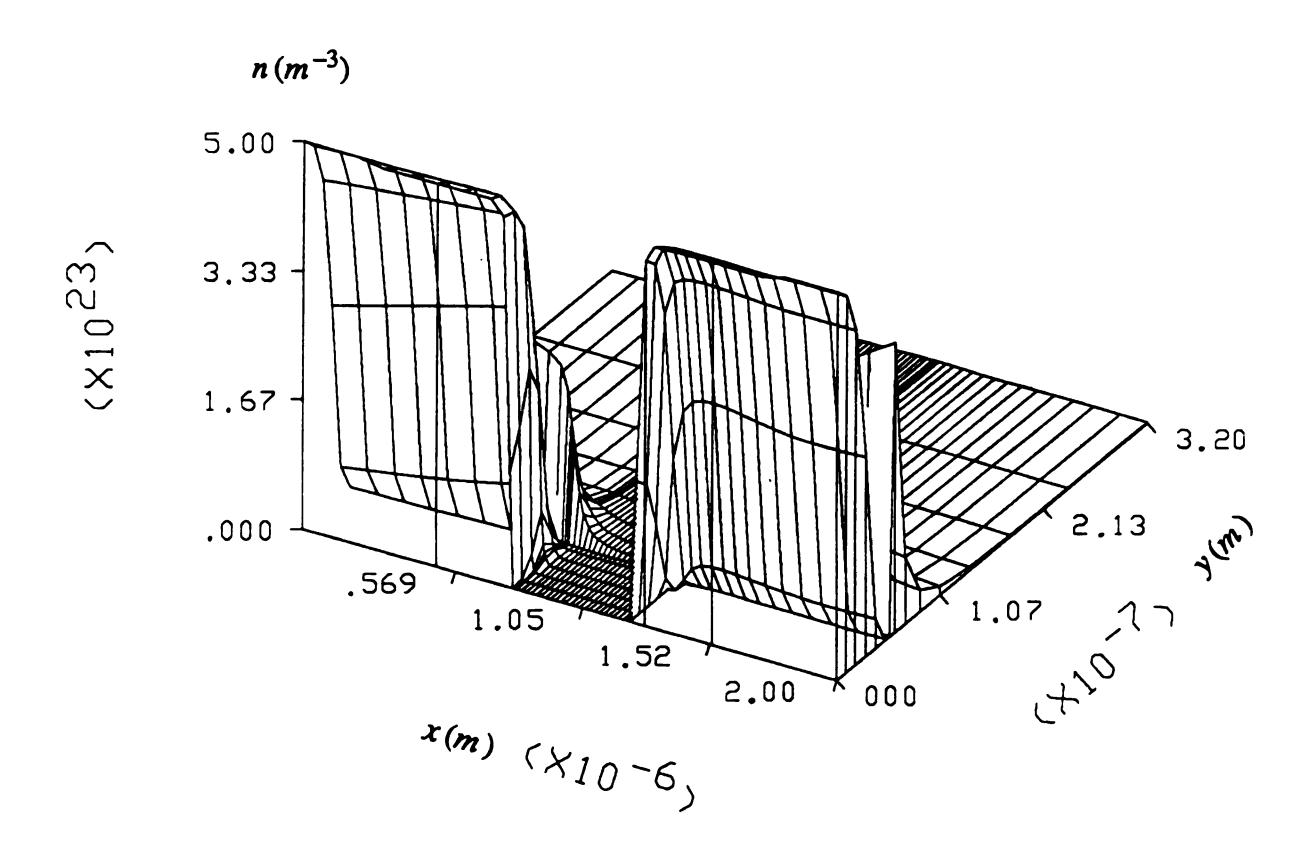


Figure 6.6. Electron density distribution ( $m^{-3}$ ) over the entire device for  $V_{GS} = 0.0 V$  and  $V_{DS} = 1.0 V$ . The source is the front left region and the drain is the front right region. The gate extends from  $0.8 \, \mu m$  to  $1.2 \, \mu m$ .

band discontinuity. The density of accumulated electrons under the gate region is less than the density under the source and drain contacts due to the gate depletion. The electron energy is shown in Figure 6.7 in the GaAs layer. Note that the electron energy is relaxed to the room temperature energy at the drain ohmic contact. The drain ohmic contact has a depth of  $d_3=150nm$  and the total simulated depth is  $d_4=320nm$ . Figure 6.8 shows the longitudinal current density in the GaAs layer where most of the current flows close to the heterojunction.

The charge-partitioning method has used to calculate the current unity gain. For  $V_{DS}=1~V$ ,  $V_{GS}=0.0~V$ , the CP method gives  $g_m=134mS/mm$ ,  $c_g=4.7\times10^{-10}mF/mm$  and  $f_T=45.37GHz$ . For  $V_{DS}=1~V$ ,  $V_{GS}=0.2~V$ , the CP method gives  $g_m=266mS/mm$ ,  $c_g=6.44\times10^{-10}mF/mm$ , and  $f_T=65.73GHz$ .

For the  $S^3A$  simulation of the MODFET, one change has been made to the equilibrium boundary conditions (e-f) and (g-h) in Figure 6.3(c). The temperature at equilibrium is fixed at room temperature,  $T=T_0$ , so the small signal temperature is  $\tilde{T}=0$ . The MODFET is biased at  $V_{DS}=1\,V$  and  $V_{GS}=0.0\,V$ . Figure 6.9 shows the y-parameters at the frequencies 10, 20, 30, 40, 50, 100 and 150 GHz. Using the y-parameters, the unilateral power gain  $G_U$  and the current gain  $A_I$  are calculated as shown in Figure 6.10 using equations (5.19) and (5.21). Note that the unity current gain  $f_T$  using y-parameters gives 51.48 GHz and recall that the CP method gives 45.37 Ghz. This means that the CP method underestimates by 10 percent. The simulator had slow convergence for higher frequencies making the determination of  $f_{\rm max}$  difficult. However, the device performance can still be studied through the unity gain frequency  $f_T$ .

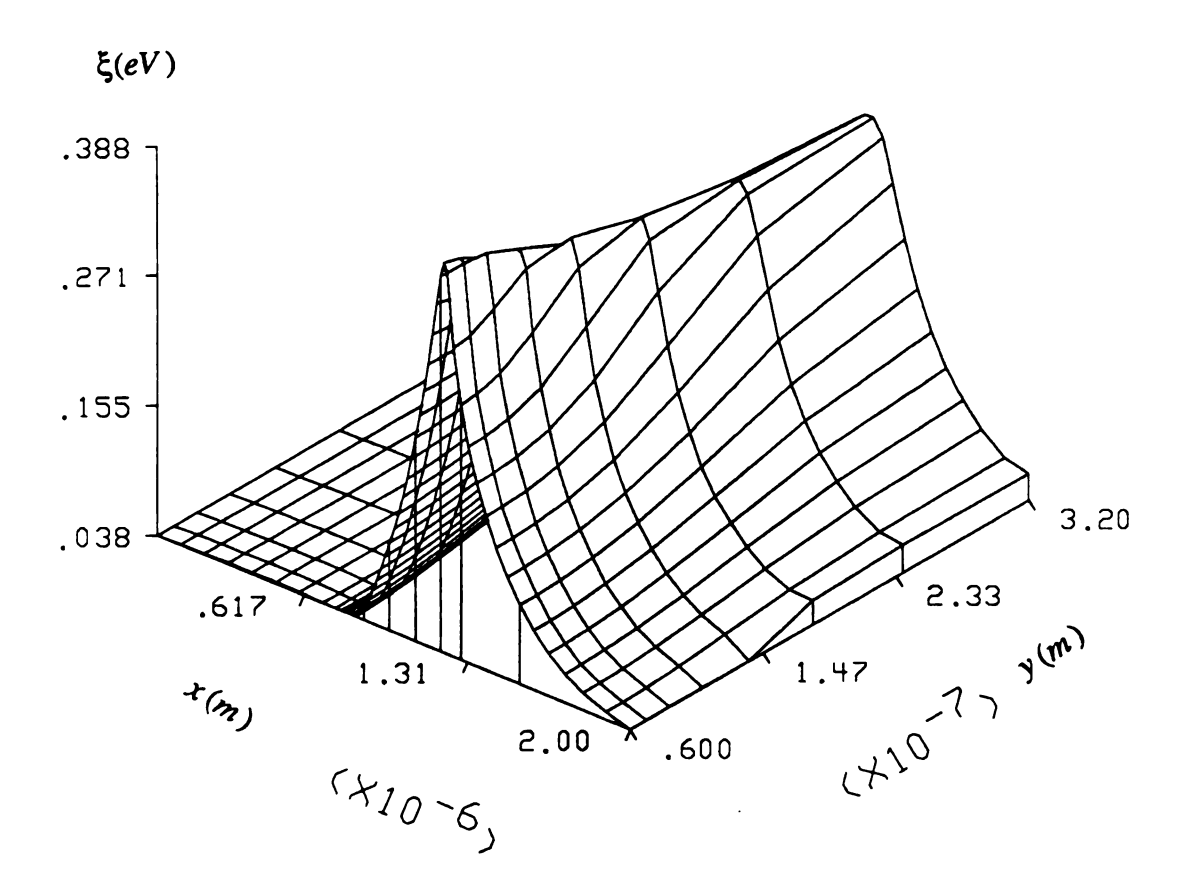


Figure 6.7. Electron energy distribution (eV) over the GaAs layer for  $V_{GS} = 0.0 \, V$  and  $V_{DS} = 1.0 \, V$ . The source is the front left region and the drain is the front right region. The gate extends from  $0.8 \, \mu m$  to  $1.2 \, \mu m$ .

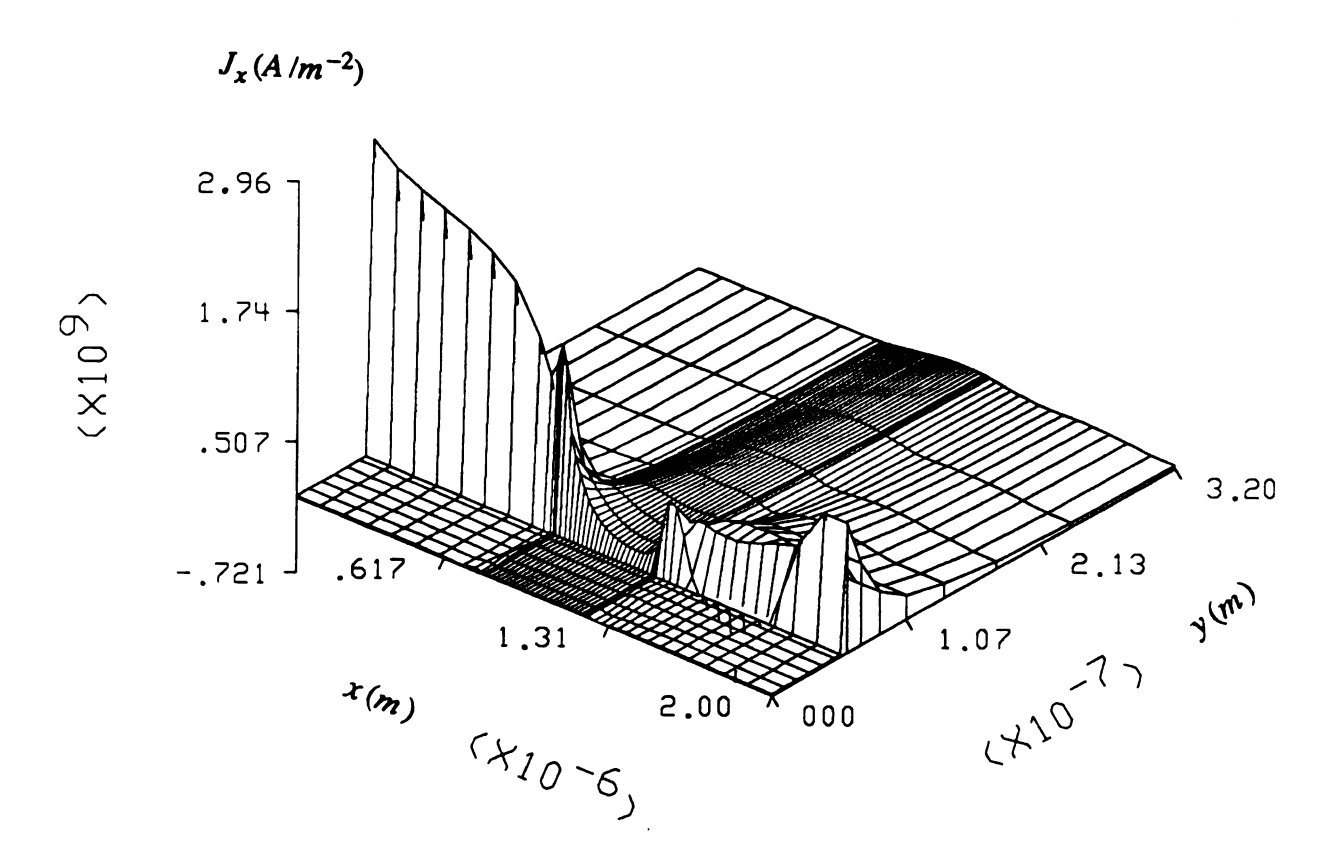


Figure 6.8. Longitudinal electron current density distribution  $(A/m^2)$  over the entire device for  $V_{GS} = 0.0 V$  and  $V_{DS} = 1.0 V$ . The source is the front left region and the drain is the front right region. The gate extends from  $0.8 \, \mu m$  to  $1.2 \, \mu m$ .

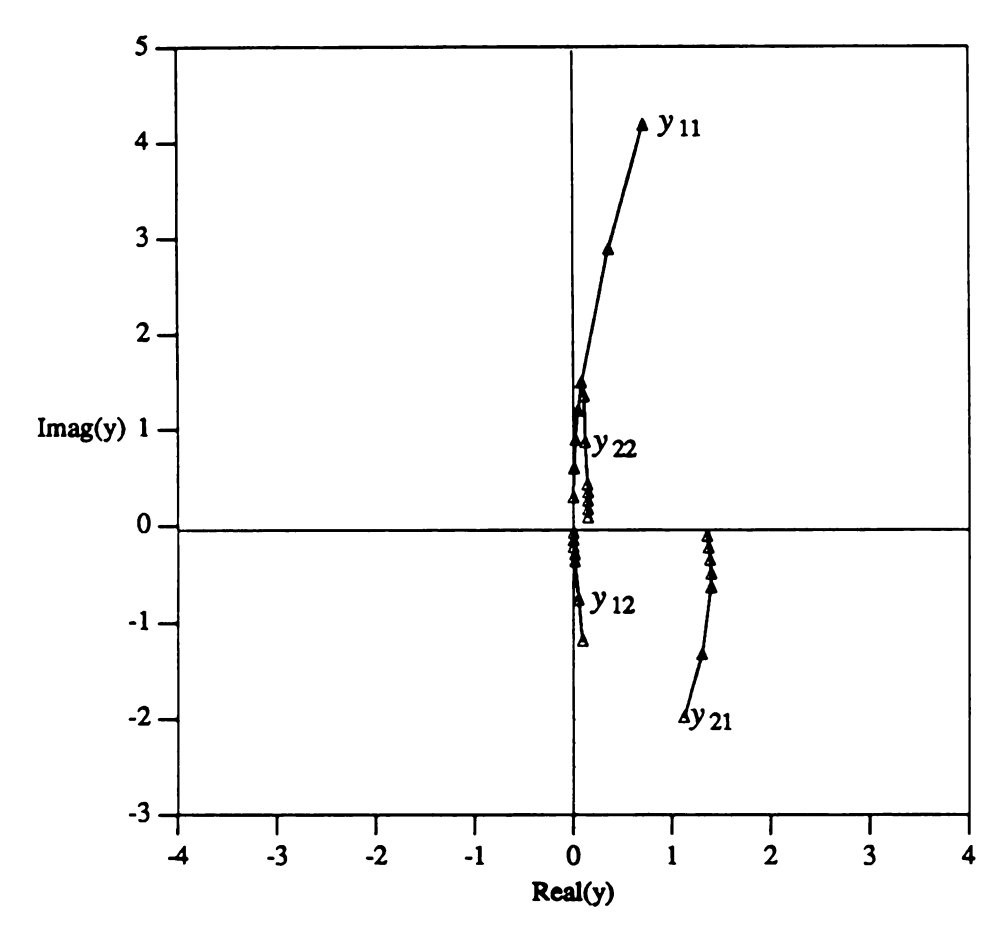


Figure 6.9. The y-parameters versus frequency for the MODFET using HTM. The seven frequencies are 10, 20, 30, 40, 50, 100 and 150 GHz.

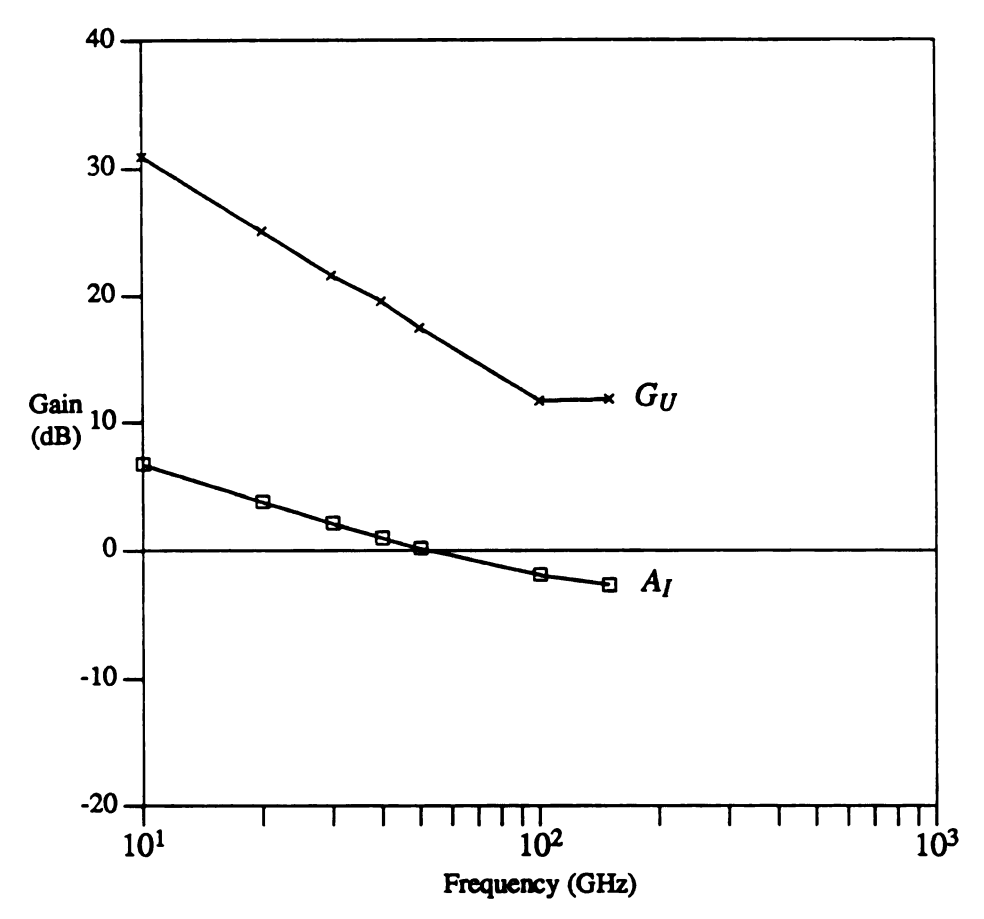


Figure 6.10.  $G_U$  and  $A_I$  versus frequency for the MODFET using HTM. The seven frequencies are 10, 20, 30, 40, 50, 100 and 150 GHz.

### **CHAPTER 7**

### CONCLUSIONS AND RECOMMENDATIONS

The hydrodynamic transport model applied to semiconductor device simulation is an important area of investigation. The HTM makes a large improvement over the DDM with only moderate increases in computation time. Additionally, it takes much less computation time than Monte Carlo simulation and provides results that agree well with those from Monte Carlo simulation.

Chapter 2 of this dissertation derived the moment equations from the Boltzmann transport equation based on a parabolic band structure. Instead of solving the Boltzmann transport equation directly, this moment equations model solves for three characteristic quantities to describe the carrier distribution function. This model was then applied to modeling the short channel MESFET after reviewing modeling work by other authors based on somewhat different approximations.

Up to this date, the simulators using the HTM were primarily developed using the finite-difference method due to its simplicity and regularity. Also, the finite-difference method allows the application of the Scharfetter-Gummel discretization in order to handle the exponential dependence of electron concentration on potential and temperature. The finite-element method is difficult to apply to HTM because the electron density is exponentially dependent on voltage and temperature. The box-integration method, which is essentially a finite-difference method based on a triangular mesh or rectangular mesh, links both methods and is a good approach to discretize the semiconductor equations since the Scharffeter-Gummel technique can also be used in the discretization. It was the box-integration method which was used in this study.

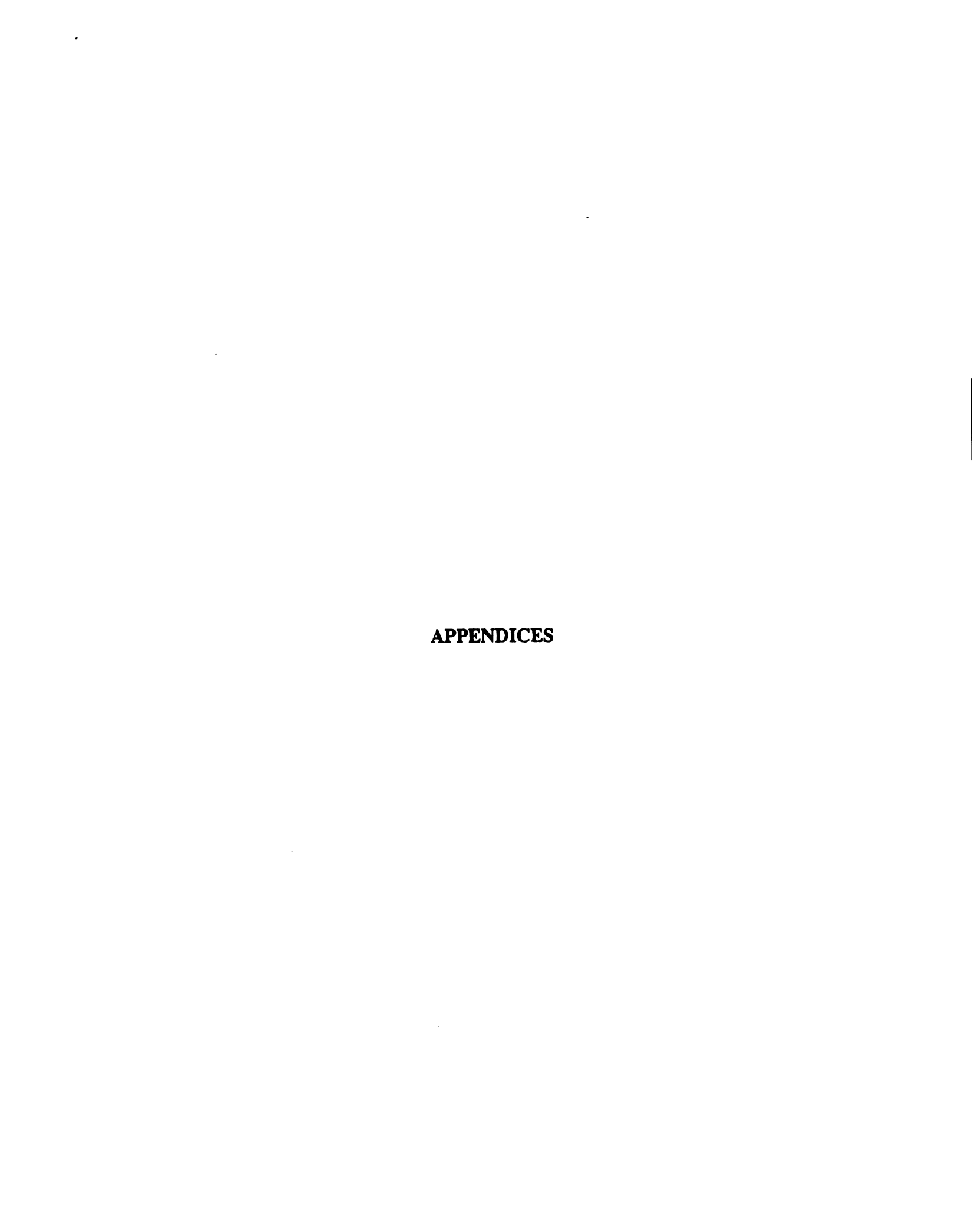
The HTM simulator was applied to the DC solution of the MESFET in Chapter 4.

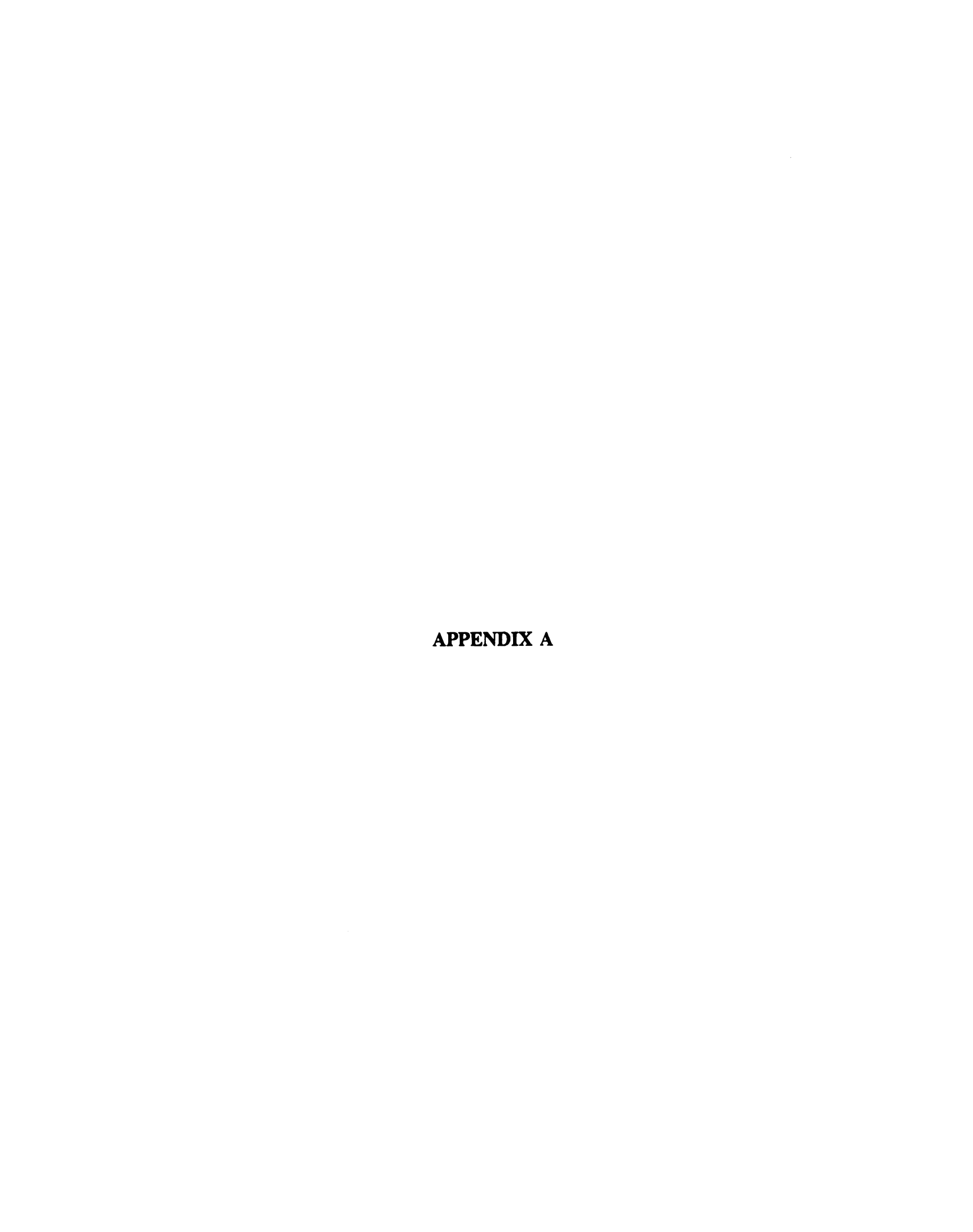
The material dependent parameters including electron velocity, electron energy and

energy relaxation time were calculated using a one-particle Monte Carlo simulator. The accuracy and the validity of the HTM simulator was checked by simulating a GaAs MESFET in two-dimensions using both the HTM simulator and a Monte Carlo FET simulator. Since both simulations originated from a common set of material parameters, any differences were due to the different models. The two simulator showed good agreement. The HTM simulator was then used as part of a study to investigate the bias dependence of the parasitic source and drain resistances in the MESFET. It was shown that the high energy of the electrons entering the drain region significantly changes the drain resistance at high drain voltage values.

The AC solution of FETs using the sinusoidal steady-state analysis  $(S^3A)$  technique applied to the HTM was developed in Chapter 5. The previous AC solution methods for the hydrodynamic transport equation were conducted by using either the charge-partitioning method or Fourier decomposition method. The  $S^3A$  method has an advantage in that the accuracy of the AC solution is easier to obtain and verify. This application of the  $S^3A$  method to the hydrodynamic transport equations is one of the key contributions of this work. The  $S^3A$  method was then used to simulate and study the millimeter wave performance of submicrometer GaAs MESFETs.

The HTM model was then modified and applied to simulating the DC and AC behavior of MODFETs. The MODFET model included the effects of the heterojunction in the solution of the Poisson equation and the transport equations. The MODFET study showed that the current implementation of the HTM to heterojunctions has some limitations for the  $S^3A$  AC solutions at high frequencies. Some areas for future work include the flow of currents across the heterojunction in MODFETs and the solution of MODFETs at very high frequencies.





## APPENDIX A

# FINITE-ELEMENT DISCRETIZATION FOR DRIFT-DIFFUSION MODEL

The finite-element method [24,63] produces approximations  $\psi_j^h$  and  $n_j^h$  to the exact solution for potential  $\psi_j$  and concentration  $n_j$  at point j. The approximations may be conveniently formulated by defining a 'shape function'  $\theta_i$  so that the approximations to  $\psi$  and n becomes for m degrees of freedom

$$\psi^h = \sum_{i=1}^m \psi_i^h \theta_i(x, y) \tag{A1}$$

and

$$n^h = \sum_{i=1}^m n_i^h \theta_i(x, y) \tag{A2}$$

where  $\psi_i^h$  denotes  $\psi^h(x_i, y_i)$  and  $n_i^h$  denotes  $n^h(x_i, y_i)$ . The shape functions  $\theta_i(x, y)$  are defined in two-dimension such that

$$\theta_i(x_i, y_i) = 0 \text{ for } i \neq j \text{ for } i = 1, 2, ..., m$$
 (A3)

and

$$\theta_i(x_j, y_j) = 1$$
 for  $i = j$  for  $i = 1, 2, ..., m$ . (A4)

The approximations  $\psi_j^h$  and  $n_j^h$  are found using the Galerkin method. The Galerkin method applied in two-dimensions may be defined for each element in terms of the residual  $R_i$ , (error in the solution), in the  $i^{th}$  element as

$$\sum_{i=1}^{n} \int R_i \theta_i^{\ j} dA = 0 \tag{A5}$$

where n is the number of elements.  $\theta_i^{j}$  is the  $j^{th}$  shape function in the  $i^{th}$  element.

Consider the generalized set of non-linear partial differential equations

$$\nabla \cdot \mathbf{F}_i(u, \nabla u) - c_i(u, \dot{u}) = 0 \qquad i = 1, 2, 3, \dots, n \tag{A6}$$

where F represents any physical flow quantity like electric flux density **D** or current density **J**. u denotes the unknown variables such as potential  $\psi$  or electron density n. Applying the two-dimension approximation as shown in (A1) and (A2) gives

$$u(x,y) = \sum_{i=1}^{m} \alpha_i \theta_i(x,y)$$
 (A7)

where

$$\alpha_i = u(x_i y_i) . (A8)$$

The Galerkin condition requires that

$$R_i(\alpha) = \int_{\Omega} \theta_i (\nabla \cdot \mathbf{F} - c) d\Omega = 0.$$
 (A9)

Using the identity

$$\nabla \cdot \mathbf{\theta}_i \mathbf{F} = \mathbf{\theta}_i \nabla \cdot \mathbf{F} + \mathbf{F} \cdot \nabla \mathbf{\theta}_i \tag{A10}$$

we have

$$\int_{\Omega} \theta_{i} \nabla \cdot \mathbf{F} d\Omega = \int_{\Gamma} \theta_{i} \mathbf{F} \cdot \vec{n} dl - \int_{\Omega} \mathbf{F} \cdot \nabla \theta_{i} d\Omega$$
 (A11)

where the divergence theorem is used to transform the area integral over  $\Omega$  into a line integral over  $\Gamma$ . Using (A11), (A9) can be rewritten as

$$R_{i}(\alpha) = \int_{\Gamma} \theta_{i} \mathbf{F} \cdot \vec{n} dl - \int_{\Omega} (\nabla \theta_{i} \cdot \mathbf{F} + \theta_{i} c) d\Omega \qquad i = 1, 2, 3, ..., m . \tag{A12}$$

Hence the sum over the n finite elements is given by

$$R(\alpha) = \sum_{i=1}^{n} \left[ \int_{\Gamma} \theta_{i} \mathbf{F} \cdot \vec{n} dl - \int_{\Omega} (\nabla \theta_{i} \cdot \mathbf{F} + \theta_{i} c) d\Omega \right] = 0.$$
 (A13)

The integrals over  $\Gamma$  vanish because of the boundarys and the definition of the shape functions [24] ( for example  $\nabla \psi \cdot \vec{n} = \partial \psi / \partial \vec{n}$  is the derivative normal to the boundary

which is set to zero for free surfaces). Hence, (A13) reduces to

$$R(\alpha) = \sum_{i=1}^{n} \left[ \int_{\Omega} (\nabla \theta_i \cdot \mathbf{F} + \theta_i c) d\Omega \right] = 0.$$
 (A14)

This matrix expression is used to solve for  $\alpha_i = u(x_i, y_i), i = 1, 2, ..., m$ .

The Poisson equation is expressed as

$$\nabla \cdot \varepsilon \nabla \psi + q(N_D - n) = 0. \tag{A15}$$

Comparing (A15) with (A6),  $\mathbf{F} = \varepsilon \nabla \psi$  and  $c = -q(N_D - n)$  are obtained. Using (A1),(A2) and (A14), the Poisson equation (A15) can be discretized as

$$[K^{\Psi}]\Psi^{h} - q[M][N_{D}^{h} - n^{h}] = 0 \tag{A16}$$

where

$$K_{ij}^{\Psi} = \int_{\Omega} \varepsilon \nabla \theta_i \cdot \nabla \theta_j \, ds \tag{A17}$$

and

$$M_{ij} = \int_{\Omega} \theta_i \, \theta_j \, ds \quad . \tag{A18}$$

Similarly, the continuity equation for electrons is expressed as

$$\nabla \cdot \mathbf{J} - q \frac{\partial n}{\partial t} + qG = 0 \tag{A19}$$

and

$$\mathbf{J} = q \left( n \,\mu_n \mathbf{E} + D_n \,\nabla n \right) \tag{A20}$$

where G is the net generation rate. Comparing (A19) with (A6),  $\mathbf{F} = \mathbf{J}$  and  $c = q(\partial n/\partial t) - qG$  are obtained. Using (A1), (A2) and (A14), the continuity equation for electrons (A19) can be discretized as

$$q[M]\frac{\partial n^h}{\partial t} + [K^n]n^h - B^h = 0 \tag{A21}$$

where

$$K_{ij}^{\ n} = \int_{\Omega} q \, \nabla \theta_i \cdot (\theta_j \, \mu_n^{\ h} \, \mathbf{E}^h \, + D_n^{\ h} \, \nabla \theta_j) ds \tag{A22}$$

and

$$B_i = \int_{\Omega} q \,\theta_i G^h \, ds \quad . \tag{A23}$$

(A16) and (A21) are the discretized equations using finite element method for Poisson and continuity equations, respectively.



#### APPENDIX B

# DERIVATION OF THE CURRENT DENSITY AND ENERGY FLUX EXPRESSIONS USING THE MODFIED SCHARFETTER-GUMMEL TECHNIQUE

This appendix derives in detail the modified Scharfetter-Gummel expression for current density and energy flux expressions used in this study.

# (i) General Scharfetter-Gummel discretization:

Suppose we have the following general expression between nodes i and i+1 in the x-direction.

$$\frac{A}{w}J = a_1 \frac{1}{w}n + \frac{dn}{dx} \,, \tag{B1}$$

where A and  $a_1$  are assumed to be constant between nodes i and i+1, J is any physical flux quantity which is a function of x, w is the independent variable which is also a function of x, n is the electron concentration which exponentially depends on voltage and temperature.

(B1) can be solved by using the solution for linear first-order differential equation as follows.

Integrating factor = 
$$\exp\left[a_1\int \frac{1}{w} dx\right] = \exp\left[a_1\int \frac{1}{w} \frac{1}{(\frac{dw}{dx})} (\frac{dw}{dx}) dx\right]$$
  
=  $\exp\left[a_1\left(\frac{dw}{dx}\right)^{-1} \ln w\right] = \exp\left[a_2\ln w\right]$  (B2)

where

$$a_2 = a_1 \left[ \frac{dw}{dx} \right]^{-1} . ag{B3}$$

Multiplying the integrating factor (B2) to (B1), and integrating (B1) gives

$$n \exp(a_2 \ln w) \Big|_{x_i}^{x_{i+1}} = AJ \int_{x_i}^{x_{i+1}} \frac{1}{w} \exp(a_2 \ln w) dx$$
 (B4)

where J has been assumed constant in the interval and hence is moved out of the integration. The right hand side becomes

$$RHS = JA \int \frac{1}{w} \exp(a_2 \ln w) dx = JA \int \frac{1}{w} w^{a_2} \frac{1}{\left(\frac{dw}{dx}\right)} \frac{(dw)}{dx} dx$$

$$= \frac{JA}{\left(\frac{dw}{dx}\right)} \frac{w^{a_2}}{a_2}$$

$$= JA \frac{\exp(a_2 \ln w)}{a_2 \left(\frac{dw}{dx}\right)}.$$
(B5)

Substituting (B5) into (B4) gives

$$n\exp(a_2\ln w)\Big|_{x_i}^{x_{i+1}} = JA \frac{1}{a_2(\frac{dw}{dx})} \exp(a_2\ln w)\Big|_{x_i}^{x_{i+1}}$$
(B6)

$$n_{i+1} \exp\left[a_2 \ln w_{i+1}\right] - n_i \exp\left[a_2 \ln w_i\right]$$

$$= JA \frac{1}{a_2(\frac{dw}{dx})} \left\{ \exp\left[a_2 \ln w_{i+1}\right] - \exp\left[a_2 \ln w_i\right] \right\}$$
(B7)

$$n_{i+1} \exp\left[a_2 \ln \frac{w_{i+1}}{w_i}\right] - n_i = JA \frac{1}{a_2(\frac{dw}{dx})} \left\{ \exp\left[a_2 \ln \frac{w_{i+1}}{w_i}\right] - 1 \right\}$$
(B8)

$$J = \frac{a_2(\frac{dw}{dx})}{A} \frac{n_{i+1} \exp\left[a_2 \ln \frac{w_{i+1}}{w_i}\right] - n_i}{\exp\left[a_2 \ln \frac{w_{i+1}}{w_i}\right] - 1} .$$
 (B9)

This expression is simplified by defining

$$x_b = a_2 \ln \frac{w_i}{w_{i+1}} = -a_2 \ln \frac{w_{i+1}}{w_i}$$
 (B10)

which gives

$$J = \frac{a_1}{A} \frac{n_{i+1} \exp(-x_b) - n_i}{\exp(-x_b) - 1} . \tag{B11}$$

(B11) can be simplified further by making use of the Bernoulli function according to

$$\frac{\exp(-x_b)}{\exp(-x_b) - 1} = \frac{1}{1 - \exp(x_b)} = \frac{1}{x_b} \frac{x_b}{1 - \exp(x_b)}$$

$$= -\frac{1}{x_b} \frac{x_b}{\exp(x_b) - 1} = -\frac{1}{x_b} B(x_b)$$
(B12)

$$\frac{1}{\exp(-x_b) - 1} = \frac{1}{-x_b} \frac{-x_b}{\exp(-x_b) - 1} = -\frac{1}{x_b} B(-x_b).$$
 (B13)

Therefore,

$$J = \frac{a_1}{A} \left[ \frac{1}{-x_b} \right] \left[ n_{i+1} B(x_b) - n_i B(-x_b) \right]$$

$$= \frac{a_1}{A} \left[ \frac{1}{x_b} \right] \left[ n_i B(-x_b) - n_{i+1} B(x_b) \right]$$

$$= \frac{1}{A} \left( \frac{dw}{dx} \right) \frac{1}{\ln \frac{w_i}{w_{i+1}}} \left[ n_i B(-x_b) - n_{i+1} B(x_b) \right]. \tag{B14}$$

The following conclusion can be made

If

$$\frac{A}{w}J = a_1 \frac{1}{w}n + \frac{dn}{dx} \tag{B1}$$

then

$$J = \frac{1}{A} \left( \frac{dw}{dx} \right) \frac{1}{\ln \frac{w_i}{w_{i+1}}} \left[ n_i B \left( -x_b \right) - n_{i+1} B \left( x_b \right) \right]$$
 (B14)

where

$$x_b = a_2 \ln \frac{w_i}{w_{i+1}} = \left[ \frac{a_1}{\frac{dw}{dx}} \right] \ln \frac{w_i}{w_{i+1}}$$
(B3)

$$B(x_b) = \frac{x_b}{\exp(x_b) - 1}$$
 (B15)

# (ii) Current density J discretion:

Recall (3.20) which is

$$\frac{J}{\mu T} = \nabla T(\alpha + 1) \frac{1}{T} n + \nabla n . \tag{B16}$$

Compared with (B1), if A is replaced by  $\frac{1}{\mu}$ , w by T, and  $a_1$  by  $\nabla T(\alpha + 1)$ , then (B14) becomes

$$J_{m} = \mu_{m} \left(\frac{dT}{dx}\right) \frac{1}{\ln \frac{T_{i}}{T_{i+1}}} \left[ n_{i} B \left(-x_{b}\right) - n_{i+1} B \left(x_{b}\right) \right]$$
(B17)

and (B3) becomes

$$x_b = (\alpha + 1)\ln\frac{T_i}{T_{i+1}} \tag{B18}$$

The mesh point m is midway between points i and i+1. Equations (B16),(B17) and (B18) are the same as (3.20), (3.22) and (3.23), respectively.

# (iii) Energy flux S discretion:

Recall (3.28) which is

$$\frac{S}{-\mu \delta T} = \nabla T (\alpha + \Delta \delta^{-1}) \frac{1}{T} (Tn) + \nabla (nT) . \tag{B19}$$

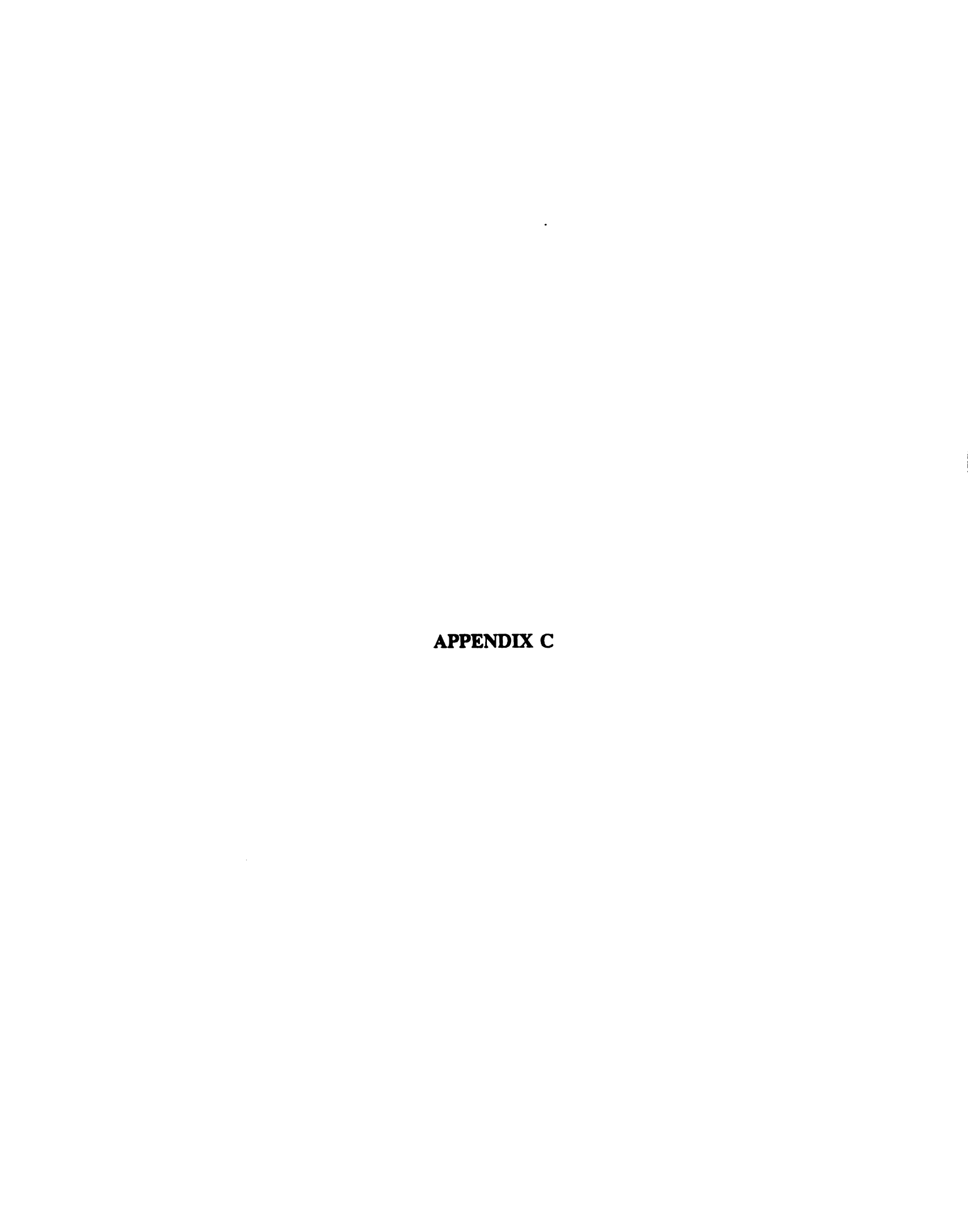
Compared with (B1), if J is replaced by S, A by  $\frac{-1}{\mu\delta}$ , w by T, n by nT, and  $a_1$  by  $\nabla T(\alpha + \Delta\delta^{-1})$ , then (B14) becomes

$$S_{j} = -\mu_{j} \delta_{j} \left(\frac{dT}{dx}\right) \frac{1}{\ln \frac{T_{i}}{T_{i+1}}} \left[ (nT)_{i} B \left(-x_{b}\right) - (nT)_{i+1} B \left(x_{b}\right) \right]$$
(B20)

and (B3) becomes

$$x_b = (\alpha + \Delta \delta^{-1}) \ln \frac{T_i}{T_{i+1}} . \tag{B21}$$

Equations (B19),(B20) and (B21) are the same as (3.28), (3.29) and (3.31), respectively.



## APPENDIX C

## RIGRID ALGORITHM

The correct allocation of the grid is a crucial issue in device simulation. The grid mesh has a direct influence on the simulation time and solution accuracy. In order to maintain the simulation time within reasonable bounds and to have satisfied solution accuracy, it is desirable to design a regrid algorithm to allocate fine grid in some regions and coarse grids in others. The mesh can be regrided based on a triangular element basis as shown in PISCES[28], or based on a rectangular basis as discussed in this appendix.

For a given rectangular mesh with  $nx \times ny$  grid points, there are nx-1 columns and ny-1 rows as shown in Figure C.1(a). There are two phases in this regrid algorithm. The first one is regrid by columns. The second is regrid by rows.

In the first phase, the columns are regrided from column 1 to column nx-1. Each column is checked as shown in Figure C.1(b). The checking may result in two cases: (1) the grid remains unchanged, or (2) the grid is changed as shown in Figure C.1(b). The grid is changed when a column has any two horizontal points across which the chosen variable changes by more than a specified tolerance. The chosen variable can be potential  $\psi$ , electron density n, or electron energy  $\xi$ . The refinement is done by adding a vertical line inside this column as shown in Figure C.1(b) and by evaluating the variables on the new added line using interpolation. If a line is added, then the total number of grid points is increased by ny. Note that the grid points are renumbered during the process of regriding due to these added new lines. After the first phase is done, the new nx will be larger than or equal to the initial nx depending on the regrid tolerance.

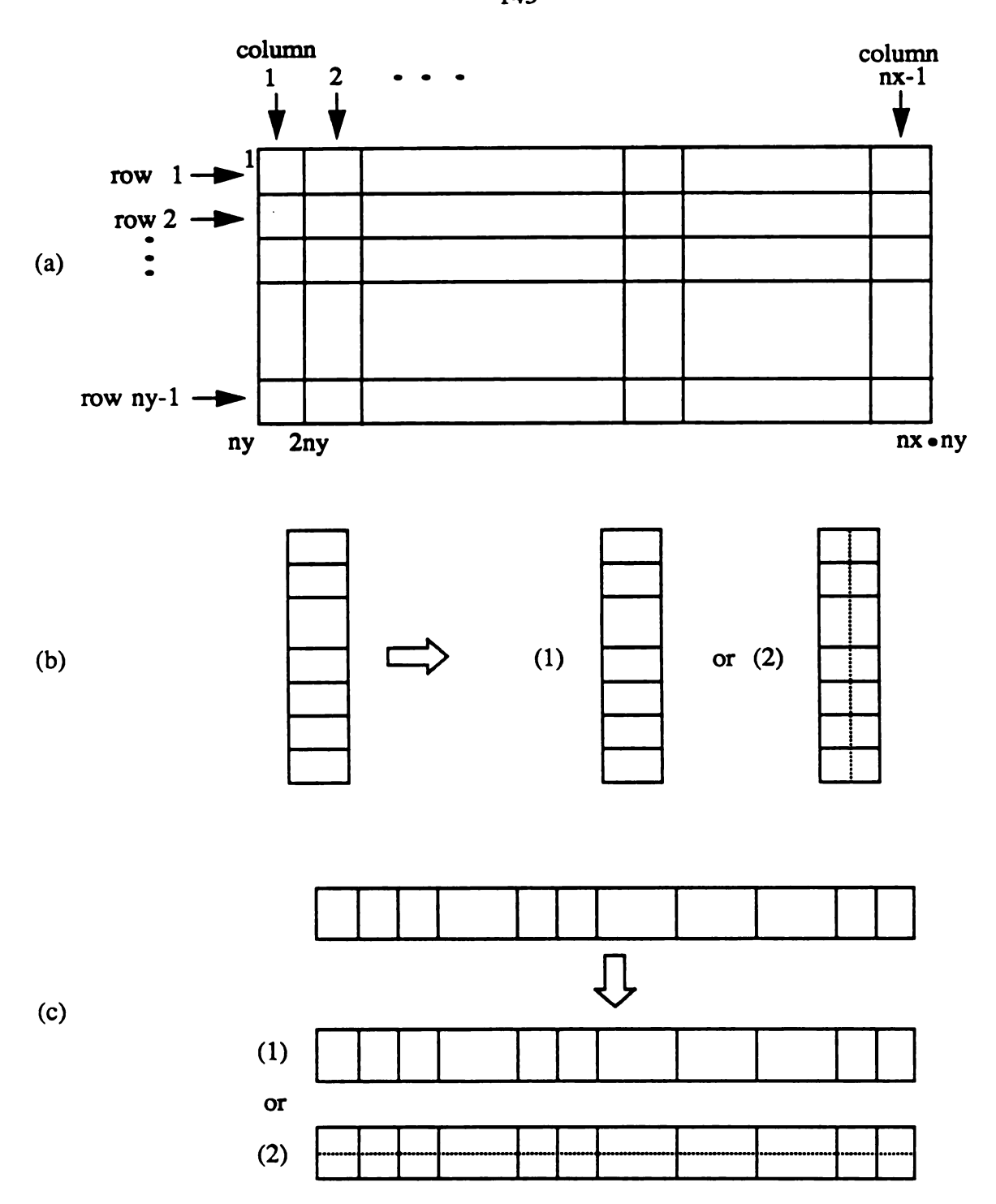
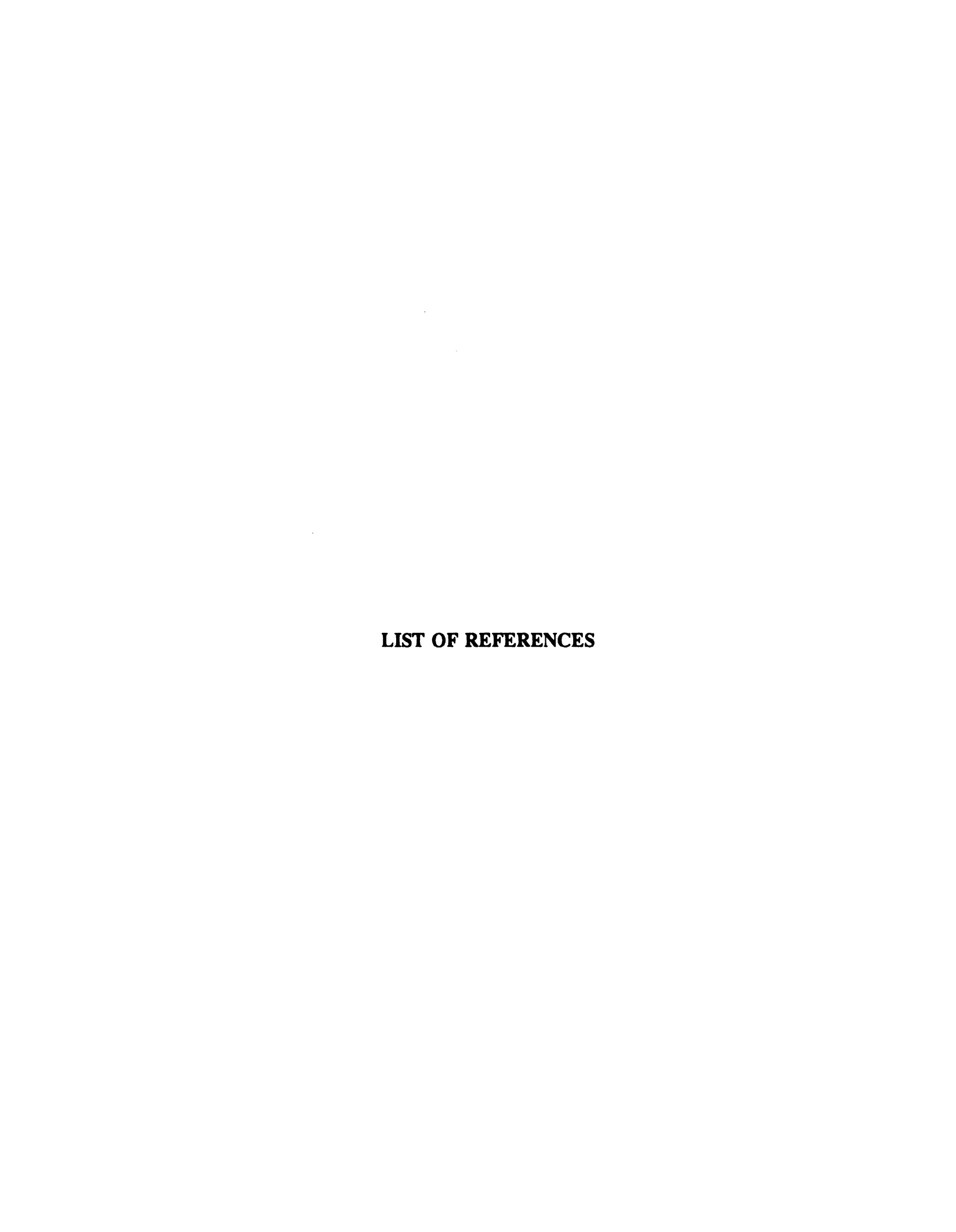


Figure C.1. Regrid algorithm for rectangular mesh. (a) The mesh contains nx-1 columns and ny-1 rows, (b) regrid for each column, and (c) regrid for each row.

In the second phase, the rows are regrided from row 1 to row ny-1 as done in the first phase for the columns. Similarly to the first phase, the row regrid may result in two cases as shown in Figure C.1(c). If a horizontal line is added, the total number of grid points is increased by nx.

For example, given an initial grid with  $nx \times ny$ , if the regrid algorithm generates 2 more lines during the column regrid and generates 1 more line during the row regrid, then the total number of grid points is increased from  $nx \times ny$  to  $(nx+2) \times (ny+1)$ . For MESFET simulation, since nx is larger than ny the increase in ny is more expensive than the increase in nx because of an increase in the bandwidth of the matrix which significantly increases computation time. Different tolerances can be set in column regrid and row regrid to keep ny as small as possible.



# LIST OF REFERENCES

- 1. C. Moglestue, "Monte Carlo particle modeling of small semiconductor devices," Computer Methods in Applied Mechanics and Engineering, vol. 30, pp. 173-208, 1982.
- 2. R. W. Hochney and J. W. Eastwood, Computer Simulation Using Particles, Chapter 10, New York, McGraw-Hill, 1981.
- 3. Y. Awano, K. Tomizawa, N. Hashizume and M. Kawashima, "Monte Carlo particle simulation of a GaAs short-channel MESFET," *Electronics Letters*, vol. 19, pp. 20-21, 1983.
- 4. A. Yoshii, M. Tomizawa and K. Yokoyama, "Accurate modeling for submicrongate Si and GaAs MESFET's using two-dimensional particle simulation," *IEEE Trans. on Electron Devices*, vol. ED-30, pp. 1376-1380, 1983.
- 5. B. Carnez, A. Cappy, A. Kaszynski, E. Constant, and G. Salmer, "Modeling of a submicrometer gate field-effect transistor including effects of nonstationary electron dynamics," *J. Appl. Phys.*, vol. 51, pp. 784-790, 1980.
- 6. R. K. Cook and J. Frey, "Two-dimensional numerical simulation of energy transport effects in Si and GaAs MESFET's," *IEEE Trans. on Electron Devices*, vol. ED-29, pp. 970-977, 1982.
- 7. C. M. Snowden and D. Loret, "Two-dimensional hot-electron models for short-gate-length GaAs MESFET's," *IEEE Trans. Electron Device*, vol. ED-34, pp. 212-223, 1987.
- 8. Y. K. Feng and A. Hintz, "Simulation of submicrometer GaAs MESFET's using a full dynamic transport model," *IEEE Trans. Electron Device*, vol. ED-35, pp. 1419-1431, 1988.
- 9. W. R. Curtice and Y. H. Yun, "A temperature model for the GaAs MESFET," *IEEE Trans. Electron Device*, vol. ED-28, pp. 954-962, 1981.
- 10. O. L. El-Sayed, S. El-Ghazaly, G. Salmer and M. Lefebvre, "Performance analysis of sub-micron gate GaAs MESFETs," *Solid-State Electronics*, vol. 30, pp. 643-654, 1987.

- 11. F. A. Buot and J. Frey, "Effects of velocity overshoot on performance of GaAs devices, with design information," *Solid-State Electronics*, vol. 26, pp. 617-632, 1983.
- 12. R. Stratton, "Diffusion of hot and cold electron in semiconductor barriers," *Phys. Rev.*, vol. 126, pp. 2002-2014, 1962.
- 13. H. H. Ou and T. W. Tang, "Numerical modeling of hot carriers in submicrometer silicon BJT's," *IEEE Trans. on Electron Devices*, vol. 34, pp. 1533-1539, 1987.
- 14. R. K. Cook, "Numerical simulation of hot-carrier transport in silicon bipolar transistors," *IEEE Trans. on Electron Devices*, vol. 30, pp. 1103-1110, 1983.
- 15. D. Widiger, I. C. Kizilyalli, K. Hess, and J. J. Coleman, "Two-dimensional transient simulation of an idealized high electron mobility transistor," *IEEE Trans. Electron Devices*, vol. ED-32, pp. 1092-1102, 1985.
- 16. K. Blotekjaer, "Transport equations for electrons in two-valley semiconductors," *IEEE Trans. Electron Device*, vol. ED-17, pp. 38-47, 1970.
- 17. T. J. M. Boyd and J. J. Sandborn, *Plasma Dynamics*, Barnes & Noble, New York, 1969.
- 18. T. J. Maloney, "Non-equilibrium electron transport in compound semiconductors," PhD dissertation, Cornell Univ., Ithaca, NY, 1977.
- 19. S. Kratzer, "Computer simulations of electron transport in GaAs," M.S. thesis, Cornell Univ., Ithaca, NY, 1978.
- 20. P. A. Sandborn, A. Rao and P. A. Blakey, "An Assessment of approximate nonstationary charge transport models used for GaAs device modeling," *IEEE Trans. Electron Devices*, vol. ED-36, pp. 1244-1253, 1989.
- 21. M. R. Friscourt, P. A. Rolland, A. Cappy, E. Constant, and G. Salmer, "Theoretical contribution to the design of millimeter-wave TEO's," *IEEE Trans. on Electron Devices*, vol. 30, pp. 223-229, 1983.
- 22. T. W. Tang, "Extension of the Scharfetter-Gummel Algorithm to the energy balance equation," *IEEE Trans. Electron Devices*, vol. ED-31, pp. 1912-1914, 1984.

- 23. D. L. Scharfetter and H. K. Gummel, "Large-signal analysis of a silicon read diode oscillator," *IEEE Trans. Electron Devices*, vol. ED-16, pp. 64-77, 1969.
- 24. J. J. Barnes and R. J. Lomax, "Finite-element methods in semiconductor device simulation," *IEEE Trans. Electron Devices*, vol. ED-24, pp. 1082-1089, 1977.
- 25. R. S. Varga, Matrix Iterative Analysis, Prentice-Hall, Englewood Cliffs, NJ, 1962.
- 26. S. Selberherr, Analysis and Simulation of Semiconductor Devices, Springer-Verlag Wien New York, 1984.
- 27. E. M. Buturla, P. E. Cottrell, B. M. Grossman and K. A. Salsburg, "Finite-element analysis of semiconductor devices: the FIELDAY program," *IBM J. Res. Develop.* vol. 25, pp. 218-231, 1981.
- 28. M. R. Pinto, C. S. Rafferty and R. W. Dutton, *PISCES-II User's Manual*, Stanford Electronics Laboratories, 1984.
- 29. A. Gnudi, F. Odeh, P. Ciampolini, M. Rudan, and G. Baccarani, "On the discretization of the hydrodynamic model of the semiconductor equations," Workshop on Numerical Modeling of Processes and Devices for Integrated Circuits--NUPAD II," May 9-10, 1988.
- 30. H. K. Gummel, "Self-consistent iterative scheme for one-dimensional steady state transistor calculations," *IEEE Trans. Electron Devices*, vol. ED-11, pp. 455-465, 1964.
- 31. A. Yoshii, M. Tomizawa and K. Yokoyama, "Investigation of numerical algorithms in semiconductor device simulation," *Solid-State Electronics*, vol. 30, pp. 813-820, 1987.
- 32. C. M. Snowden, M. J. Howes, and D. V. Morgan, "Large-signal modeling of GaAs MESFET operation," *IEEE Trans. Electron Devices*, vol. ED-30, pp. 1817-1824, 1983.
- 33. S. M. Sze, *Physics Of Semiconductor Devices*, ch. 6, 2nd ed. New York: Wiley, 1981.
- 34. P. L. Hower and N. G. Bechtel, "Current saturation and small-signal characteristics of GaAs FET's." *IEEE Trans. Electron Devices*, vol. ED-20, pp. 213-220, 1973.

- 35. H. Fukui, "Determination of the basic device parameters of a GaAs MESFET," Bell Syst. Tech. J., pp. 711-797, 1979.
- 36. P. Urien and D. Delagebeaudeuf, "New method for determining the series resistance in a MESFET or TEGFET," *Electron. Lett.*, vol. 19, pp. 702-703, 1983.
- 37. K. Lee, M. Shur, K. W. Lee, T. Vu, P. Roberts, and M. Helix, "New interpretation of 'end' resistance measurements," *IEEE Electron Device Lett.*, vol. EDL-5, pp. 5-7, 1984.
- 38. S. Chaudhuri and M. Das, "On the determination of source and drain series resistances of MESFET's" *IEEE Electron Device Lett.*, vol. EDL-5, pp. 244-246, 1984.
- 39. K. W. Lee, K. Lee, M. S. Shur, T. T. Vu, P. C. T. Roberts, M. J. Helix, "Source, drain, and gate series resistances and electron saturation velocity in ion-implanted GaAs FET's," *IEEE Trans. Electron Devices*, vol. ED-32, pp. 987-992, 1985.
- 40. L. Yang and S. I. Long, "New method to measure the source and drain resistance of the GaAs MESFET," *IEEE Electron Device Lett.*, vol. EDL-7, pp. 75-77, 1986.
- 41. Y. H. Byun, M. S. Shur, A. Peczalski and F. L. Schuermeyer, "Gate-voltage dependence of source and drain series resistances and effective gate length in GaAs MESFET's," *IEEE Trans. on Electron Devices*, vol. 35, pp. 1241-1245, 1988.
- 42. D. H. Navon, "A theorem on heat generation in semiconductor devices," *Proc. of the IEEE*, vol. 66, pp. 520-522, 1978.
- 43. M. S. Adler, "Accurate calculations of the forward drop and power dissipation in thyristors," *IEEE Trans. on Electron Devices*, vol. ED-25, pp. 16-22, 1978.
- 44. Y. Awano, K. Tomizawa and H. Hashizume, "Principles of operation of short-channel gallium arsenide field-effect transistor determined by Monte Carlo method," *IEEE Trans. on Electron Devices*, vol. ED-31, pp. 448-452, 1984.
- 45. W. Fawcett, A. D. Boardman and S. Swain, "Monte Carlo determination of electron transport properties in gallium arsenide," *J. Phys. and Chem. of Solids*, vol. 31, pp. 1963-1990, 1970.

- 46. K. Brennan and K. Hess, "High field transport in GaAs, InP and InAs," Solid-State Electronics, vol. 27, pp. 347-357, 1984.
- 47. T. A. Grotjohn, "Compensation effects on the electron velocity in submicron GaAs MESFET's," *IEEE Trans. on Electron Devices*, vol. 35, pp. 1144-1145, 1988.
- 48. S. E. Laux, "Techniques for small-signal analysis of semiconductor devices," *IEEE Trans. Electron Devices*, vol. ED-32, pp. 2028-2037, 1985.
- 49. G. D. Vendelin, Design of amplifiers and oscillators by the S-parameter method, pp. 32-33, Wiley, 1982.
- 50. M. B. Das and P. Schmidt, "High-frequency limitations of abrupt-junction FET's," *IEEE Trans. Electron Devices*, vol. ED-20, pp. 779-792, 1973.
- 51. M. B. Steer and R. J. Trew, "High-frequency limits of millimeter-wave transistor," *IEEE Electron Dev. Lett.*, vol. EDL-7, pp. 640-642, 1986.
- 52. R. J. Trew and . B. Steer, "Millimeter-wave performance of state-of-the-art MES-FET, MODFET and PBT transistors," *Electronics Letters*, vol. 23, pp. 149-151, 1987.
- 53. H. O. Vickes, "Note on unilateral power gain as applied to submicrometre transistors," *Electronics Letters*, vol. 24, pp. 1503-1505, 1988.
- 54. T. Shawki, G. Salmer, and O. El-sayed, "MODFET 2-D hydrodynamic energy modeling: optimization of subquarter-micro-gate structures," *IEEE Trans. Electron Devices*, ED-37, pp. 21-30, 1990.
- 55. U. Ravaioli and D. K. Ferry, "MODFET ensemble Monte-Carlo model including the quasi-two-dimensional electron gas," *IEEE Trans. on Electron Devices*, vol. 33, pp. 154-156, 1986.
- 56. J. Yoshida, "Classical versus quantum mechanical calculation of the electron distribution at the n-AlGaAs/GaAs heterointerface," *IEEE Trans. Electron Devices*, ED-33, pp. 154-156, 1986.
- 57. E. M. Azoff, "Generalized energy-momentum conservation equations in the relaxation time approximation," *Solid-State Electronics*, vol. 30, pp. 913-917, 1987.

- 58. K. Horio, Y. Iwatsu, and H. Yanai, "Numerical Simulation of AlGaAs/GaAs Heterojunction Bipolar Transistors with Various Collector Parameters," *IEEE Trans. on Electron Devices*, vol. 36, pp. 617-624, 1989.
- 59. S. J. Lee and C. R. Crowell, "Parasitic source and drain resistance in highelectron-mobility transistors," *Solid-State Electronics*, vol. 28, pp. 659-668, 1985.
- 60. D. Loret, "Two-dimensional numerical model for the high electron mobility transistor," *Solid-State Electronics*, vol. 30, pp. 1197-1203, 1987.
- R. W. Hockney, R. A. Warriner, and M. Reiser, "Two-dimensional particle models in semiconductor-device analysis," *Electronics Lett.*, vol. 10, pp. 483-486, 1974.
- 62. C. Moglestue and S. J. Beard, "A particle model simulation of field effect transistors," ed. B. T. Browne and J. J. H. Miller, Numerical Analysis of semiconductor Devices, Boole Press, Dublin, Ireland, pp. 232-236, 1979.

